UC San Diego
UC San Diego Electronic Theses and Dissertations

Title
Optical spectroscopy of correlated oxides

Permalink
https://escholarship.org/uc/item/0553g24h

Author
Stewart, Margaret K.

Publication Date
2011

Peer reviewed|Thesis/dissertation

eScholarship.org
Powered by the California Digital Library
University of California

UNIVERSITY OF CALIFORNIA, SAN DIEGO

Optical Spectroscopy of Correlated Oxides

A dissertation submitted in partial satisfaction of the
requirements for the degree
Doctor of Philosophy

in

Physics

by

Margaret K. Stewart

Committee in charge:

Professor Dimitri N. Basov, Chair
Professor Prabhakar R. Bandaru
Professor Massimiliano Di Ventra
Professor Jorge E. Hirsch
Professor Shayan Mookherjea

2011

Copyright
Margaret K. Stewart, 2011
All rights reserved.

The dissertation of Margaret K. Stewart is approved, and it is acceptable in quality and form for publication on microfilm and electronically:

Chair

University of California, San Diego

2011

DEDICATION

To Jeff and Katelyn

TABLE OF CONTENTS

LIST OF FIGURES

LIST OF TABLES

ACKNOWLEDGEMENTS

First I would like to thank my advisor Dimitri Basov for his guidance and patience through this process. I am also grateful to all the past and current members of the Basov group for their help with equipment and experiments and for useful feedback.

I am thankful to my parents for their for their unequivocal support and for always believing in me. To Jeff, my husband and my partner through grad school, for letting me share this journey with him and for giving me confidence. Finally, I am grateful to my daughter Katelyn for all the joy she has brought to my life.

Chapter 2, in full, is a reprint of the material as it appears in Phys. Rev. B **79**, 144414 (2009). M. K. Stewart, K. B. Chetry, B. Chapler, M. M. Qazilbash, A. A. Schafgans, A. Gupta, T. E. Tiwald, and D. N. Basov. The dissertation author was the primary investigator and author of this paper.

Chapter 3, in full, is a reprint of the material as it appears in J. of Appl. Phys. **110**, 033514 (2011). M. K. Stewart, J. Liu, R. K. Smith, B. C. Chapler, C.-H. Yee, D. Meyers, R. E. Baumbach, M. B. Maple, K. Haule, J. Chakhalian, and D. N. Basov. The dissertation author was the primary investigator and author of this paper.

Chapter 4, in full, is a reprint of the material as it appears in Phys. Rev. B. **83**, 075125 (2011). M. K. Stewart, C.-H. Yee, J. Liu, M. Kareev, R. K. Smith, B. C. Chapler, M. Varela, P. J. Ryan, K. Haule, J. Chakhalian, and D. N. Basov. The dissertation author was the primary investigator and author of this paper.

Chapter 5, in full, is a reprint of the material as it appears in Phys. Rev. Lett. **107**, (2011). M. K. Stewart, J. Liu, M. Kareev, J. Chakhalian, and D. N. Basov. The dissertation author was the primary investigator and author of this paper.

Chapter 6, in full, is currently being prepared for submission for publication of the material. M.K. Stewart, D. Brownstead, K. W. West, S. Wang, J. G. Ramirez, I. K. Schuller, and D. N. Basov. The dissertation author was the primary investigator and author of this material.

VITA

2007	B. S. in Physics *with highest distinction*, Purdue University
2009	M. S. in Physics, University of California, San Diego
2011	Ph. D. in Physics, University of California, San Diego

PUBLICATIONS

M. K. Stewart, D. Brownstead, K. G. West, S. Wang, J. G. Ramirez, I. K. Schuller and D. N. Basov, "Insulator-to-metal transition and correlated metallic state of V_2O_3 investigated by optical spectroscopy", in preparation.

M. K. Stewart, J. Liu, M. Kareev, J. Chakhalian, and D. N. Basov, "Mott physics near the insulator to metal transition in $NdNiO_3$", Physical Review Letters, in press.

M. K. Stewart, C.-H. Yee, J. Liu, M. Kareev, R. K. Smith, B. C. Chapler, M. Varela, P. J. Ryan, K. Haule, J. Chakhalian, and D. N. Basov, "Optical study of strained ultrathin films of strongly correlated $LaNiO_3$", Physical Review B 83, 075125 (2011).

M. K. Stewart, J. Liu, R. K. Smith, B. C. Chapler, C.-H. Yee, D. Meyers, R. E. Baumbach, M. B. Maple, K. Haule, J. Chakhalian, and D. N. Basov, "Optical probe of strong correlations in $LaNiO_3$", Journal of Applied Physics 110, 033514 (2011).

M. K. Stewart, K. B. Chetry, B. Chapler, M. M. Qazilbash, A. A. Schafgans, A. Gupta, T. E. Tiwald, and D. N. Basov, "Ellipsometric study of the electronic band structure of CrO_2 across the ferromagnetic transition", Physical Review B 79, 144414 (2009).

ABSTRACT OF THE DISSERTATION

Optical Spectroscopy of Correlated Oxides

by

Margaret K. Stewart

Doctor of Philosophy in Physics

University of California, San Diego, 2011

Professor Dimitri N. Basov, Chair

This dissertation presents optical studies of correlated oxide thin films mainly through the use of spectroscopic ellipsometry. The main focus is on exploring how electron-electron interactions shape the electronic properties of various transition metal oxides, although work on weakly correlated CrO_2 is also included. Epitaxial strain and temperature are employed as "tuning knobs" for material properties, often inducing and in one case completely suppressing a phase transition. A series of nickelate thin films of varying thickness and strain are investigated over broad energy and temperature ranges, spanning both the insulating and metallic phases. The far-infrared parts of the spectra are studied in the context of the extended Drude model. A detailed analysis is carried out to assess the energy scales associated with the transfer of electronic spectral weight across the insulator-to-metal transition and within the metallic state. These results are then compared to the predictions of the Mott-Hubbrad model for correlated electron systems. Additionally, a similar analysis is employed to study thin films of V_2O_3, which exhibits and insulator-to-metal transition at ~ 150 K. Finally, a study of the ferromagnetic transition in half-metallic CrO_2 is presented. The optical response of the films along various crystallographic directions is extracted from ellipsometry data and a comparison to existing band structure calculations is presented.

Chapter 1

Introduction

Correlated electron systems have been of great interest to researchers over most of the past century due to the variety of rich physics that can be found in them, such as insulator-to-metal transitions and high temperature superconductivity. In many cases, the quest to understand and control these phenomena continues today. Optical spectroscopy is a powerful tool in the study of correlated electron matter, allowing one to probe the excitation spectra and the dynamics of the free carriers in a contact-less manner. Specifically, through the use of optical sum rules it is possible to obtain the electronic kinetic energy from experimental data. This quantity, in conjunction with band theory calculations, can be used to quantify the strength of electronic correlations in a material. Additionally, by studying the temperature dependence of the optical properties, it is possible to understand the redistribution or reconstruction of electronic states in the vicinity of or across a phase transition.

In addition to temperature, epitaxial strain is another "tuning knob" that can be used to manipulate material properties. For this reason, many correlated oxides are grown as thin films on substrates that provide varying amounts of tensile and compressive strain. The aim is study how the electronic and magnetic properties are affected or controlled by strain. Variable angle spectroscopic ellipsometry is ideal for the study of thin film samples. It is possible to extract the optical spectra for the thin film material from the ellipsometric data, fully accounting for the reflections from the film/substrate interface. In this work we use spectroscopic ellipsometry over a wide energy range, in combination with near-normal incidence reflectance measurements, to study the optical properties of correlated oxide thin films. Low temperature ellipsometry measurements are possible thanks to the implementation of home-built ultra high vacuum cryogenic chambers.

In chapter 2 we report on a study of bulk-like films of the correlated metal $LaNiO_3$. Despite the metallic character of these samples, as evidenced by transport measurements, the optical conductivity does not exhibit a well-defined Drude resonance. This finding, along with a comparison to LDA calculations, positions $LaNiO_3$ as one of the most strongly correlated metals known to date.

Continuing our study of $LaNiO_3$, chapter 3 discusses the optical properties of strained ultra-thin films of this material. In this case, a coherent (Drude) response is observed for films subject to both tensile and compressive strain. By analyzing the effective electronic spectral weight we discover and unprecedented low temperature enhancement of the Drude plasma frequency at the expense of features in the optical conductivity associated with the Hubbard bands. The extended Drude analysis of the low frequency part of the spectra reveals the formation of a pseudogap and a weak temperature dependence of the carrier scattering rate in the DC limit.

In Chapter 4 we investigate another nickelate, $NdNiO_3$. Ultra-thin films subject to tensile strain exhibit an insulator-to-metal transition, similar to the bulk. When the substrate provides compressive strain however, the transition is completely quenched. Our work shows robust evidence of strong correlations in both the metallic and insulating samples. We find that Mott physics is the driving force behind insulator-to-metal transition in $NdNiO_3$ and charge-ordering is not the sole mechanism for it. The energy scales over which the transfer of electronic spectral weight takes place in both samples is consistent with the Mott-Hubbard model for correlated electron systems. These results together with those of chapter 3 position the nickelates as prototypical strongly correlated materials illustrating the DMFT predictions for Mott-Hubbard systems.

Chapter 5 reports on a study of the antiferromagnetic insulator to paramagnetic metal transition in V_2O_3. The extended Drude analysis reveals new signatures of strong correlations in the metallic phase: the partial gapping of the Fermi surface and the enhancement of the effective carrier mass as the temperature is lowered toward the insulating state. The redistribution of spectral weight over a wide energy range across the transition confirms the importance of electronic correlations in this system. Comparison to optical data for VO_2 reveals differences between insulator-to-metal transition in these two vanadates.

Lastly, in chapter 6 we present a spectroscopic ellipsometry study of the half metal CrO_2 across the ferromagnetic transition at $T_C \approx 380$ K. Detailed data collection and analysis revealed a pronounced anisotropy in the optical constants of the films, related to the anisotropic crystal structure. We find that the relative intensities of the optical conductivity features associated with interband transitions along the different crystalographic directions are consistent with the orbital anisotropy detected in x-ray absorption experiments. The general trends in the optical conductivity spectra are consisted with existing band structure calculations. However, the lack of a pronounced temperature dependence of these features indicates that double-exchange is unlikely to be the mechanism for ferromagnetic ordering in the ground state of CrO_2.

Chapter 2

Optical probe of strong correlations in $\mathrm{LaNiO_3}$ thin films

Abstract

The optical properties of $\mathrm{LaNiO_3}$ thin films are investigated over a wide energy and temperature range. Thin films of varying thickness were grown by pulsed laser deposition on $\mathrm{LaAlO_3}$ and $\mathrm{SrTiO_3}$ substrates. The optical conductivity data of the films reveal a number of interband transitions above 1 eV which are in good agreement with band structure calculations. No well defined Drude peak is observed however, in stark contrast with LDA theory predicting a finite density of states at the Fermi energy. This experimental finding of a vanishing Drude spectral weight, compared to a finite electron kinetic energy obtained from band structure calculations, highlights the importance of strong electronic correlations in $\mathrm{LaNiO_3}$.

2.1 Introduction

Transition metal oxides exhibit a wide array of interesting physical phenomena such as high temperature superconductivity, insulator-to-metal transitions, and half-metallic ferromagnetism.[42] Modern sample growth technologies offer an opportunity to control and tune these effects through heterostructuring.[140] At the interface between two oxides with different properties, the competing order parameters can dramatically modify the orbital, electronic, and magnetic structure of the bulk materials.[107] Switching of superconductivity on and off, for instance, has been demonstrated at the interface between an oxide superconductor and an oxide ferroelectric.[129] New properties not present in the constituent materials can also emerge at these interfaces. The formation of a metallic layer at the interface between the insulators $LaAlO_3$ and $SrTiO_3$, for example, has already been demonstrated.[89] Because of the ample choice of exotic properties offered by transition metal oxides for the growth of superlattices, experimental efforts will greatly benefit from the guidance of theoretical work. It is therefore of great importance that the constituent materials be thoroughly characterized experimentally and that their properties be well understood theoretically. This can be especially challenging, given that strong electronic correlations are often present in transition metal oxides.[135]

One of the most ambitious heterostructuring ideas yet is that of superconducting $LaNiO_3/LaAlO_3$ superlattices.[25, 44] Since the discovery of high-temperature superconductivity in the cuprates, the search for new superconducting materials with potentially higher transition temperatures has been at the vanguard of condensed matter Physics research. $LaNiO_3$ (LNO) is in many ways similar to the cuprates, but with one important difference: it has one electron in two degenerate, three-dimensional e_g orbitals. The lack of orbital degeneracy and the quasi two-dimensionality of the e_g electrons are well established attributes of superconductivity in the cuprates. Modifying the orbital structure of LNO through layered heterostructuring, and successfully inducing superconductivity in this non-superconducting material, would be a major breakthrough. Because of this, and given our limited understanding of LNO thus far, a detailed optical study of this oxide promises to be of great use.

In the bulk, LNO is a paramagnetic metal with a rhombohedrally distorted perovskite crystal structure.[40] Resistivity, susceptibility and heat capacity data reported for powder LNO are suggestive of strong correlations in this system.[123]

Unlike other rare earth nickelates, LNO does not exhibit a temperature controlled metal-insulator transition, but an antiferromagnetic insulating state has been reported in oxygen deficient $LaNiO_{3-x}$.[112, 50] In this work we show that LNO is a correlated electron system, as evidenced by an experimental Drude spectral weight that is strongly suppressed compared to that predicted by band structure calculations. The optical data presented here can not be fully described by available theoretical models of LNO. We propose that a better theoretical understanding of LNO is essential in order to fully explore the possibilities and limitations of $LaNiO_3/LaAlO_3$ superlattices.

2.2 Methods

Bulk synthesis of LNO has been a challenging issue, with available single crystals limited to the micron size. Thin film deposition, on the other hand, is largely possible because of the epitaxial stabilization.[62] Thus, by pulsed laser deposition, we grew preferentially (001)-oriented LNO films on $LaAlO_3$ (LAO) and $SrTiO_3$ (STO) single crystal substrates. A KrF excimer laser (λ=248 nm) was used to ablate a stoichiometry LNO target under 100 mTorr oxygen partial pressure. The temperature during the growth was kept at 700°C and cooled to 600°C after deposition, where annealing was performed under 1 atm of oxygen for one hour. To probe the bulk behavior of LNO, the film thicknesses are 100 nm and 200 nm which are sufficiently larger than the critical thickness, therefore relaxing the structure and minimizing strain-induced distortions. The effect of strain is further isolated by comparing films subjected to opposite lattice mismatch from LAO (-1.3%) and STO (+1.8%) substrates. Representative $\theta-2\theta$ x-ray diffraction data for the 200 nm film on STO are shown in Fig.2.1. The scans reveal all (001) reflections corresponding to a (001)-oriented perovskite structure. A (110) peak commonly found in thick films is also evident. The relative intensities of the (110) and (002) peaks indicate that the (110) phase makes up much less than 0.8% of the film.[17] The c-axis parameters are 3.84 Å and 3.86 Å on STO and LAO, respectively. While the former is the same as the bulk,[40] indicating complete relaxation from the large tensile strain, the latter is slightly bigger likely due to residual strain from the relatively smaller lattice mismatch.

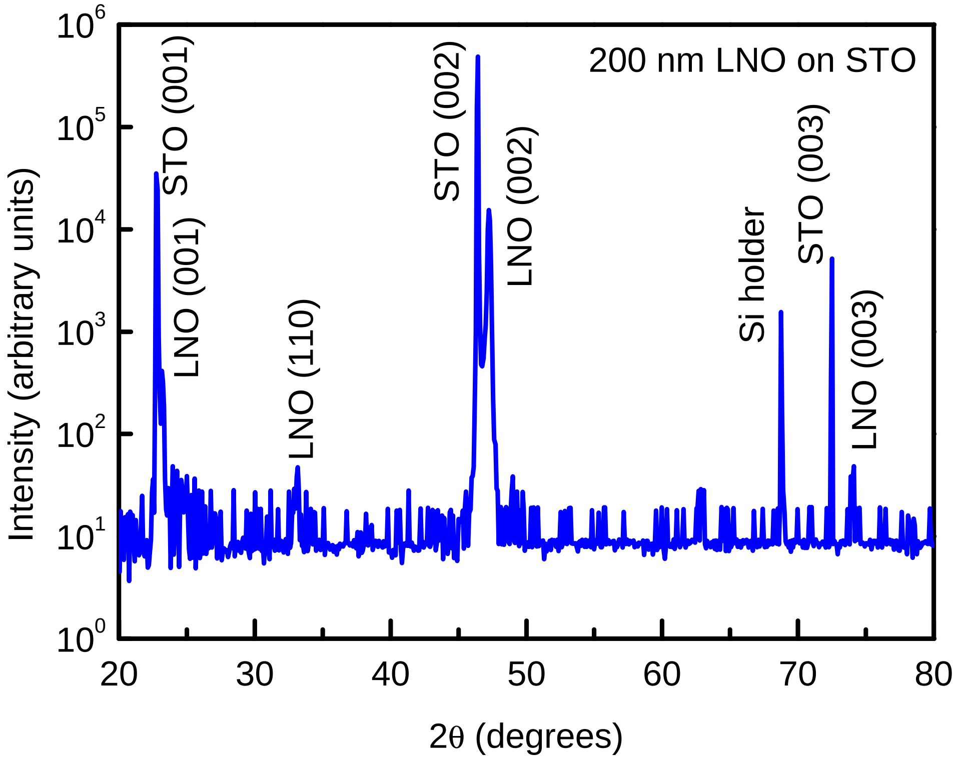

Figure 2.1: $\theta - 2\theta$ x-ray scan for the 200 nm film on STO.

Optical studies of both the films and the bare substrates were carried out using reflectance in the range from 50 to 700 cm^{-1} and variable angle spectroscopic ellipsometry (VASE) in the range from 700 to 48000 cm^{-1}. Near-normal incidence reflectance measurements were performed in a Michelson interferometer (Bruker 66vs). Reflectance of the sample was first measured relative to a gold reference mirror and then normalized by the reflectance of the gold coated sample.[49] Ellipsometry measurements were performed with two commercial Woollam ellipsometers. The range from 700 to 4500 cm^{-1} was investigated with an IR-VASE model based on a Bruker 66vs. For the range between 5000 and 48000 cm^{-1} we used a VASE model based on a grating monochromator. Both ellipsometers are equipped with home-built UHV chambers to allow low temperature measurements.[19] All the samples were characterized over the entire frequency range at room temperature

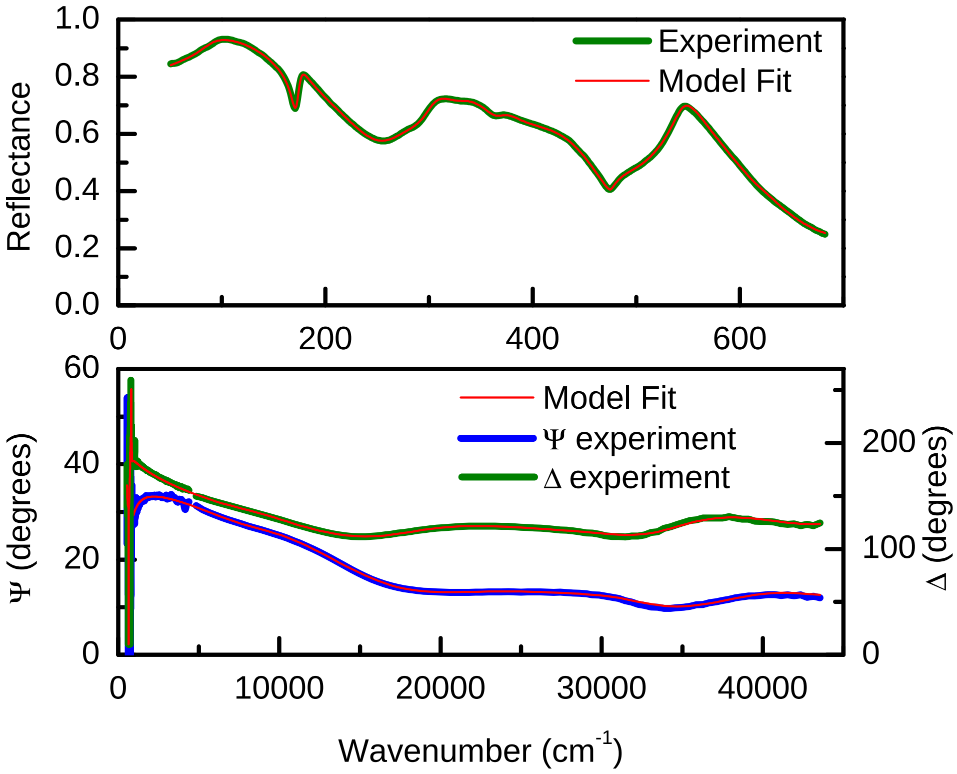

Figure 2.2: Raw reflectance (top panel) and 60° ellipsometry (bottom panel) data for the 100 nm film on STO plotted with the fit from the model (red line).

and in some cases at low temperatures down to 20 K. Ellipsometry measurements were performed at incidence angles of 60° and 75°. At each angle, the polarization state of the reflected light was measured in the form of two parameters, Ψ and Δ, which are related to the Fresnel reflection coefficients for p- and s- polarized light (R_p and R_s) through the equation $\frac{R_p}{R_s} = tan(\Psi)e^{i\Delta}$.

In order to obtain the optical constants from the raw reflectance and ellipsometry data, a model was created using Kramers-Kronig consistent Lorentz oscillators to describe the complex dielectric function of the sample. The parameters in the model were then fitted to the experimental data using regression analysis.[68] In the case of the LNO films, the model consisted of two layers: a substrate characterized by the optical constants previously determined for either LAO or STO, and a thin film layer from which the optical constants of the film alone were obtained. Figure 2.2 shows the raw reflectance and ellipsometry data plotted with the model fit for the 100 nm film on STO. The STO substrate phonons at 175 cm^{-1} and 483 cm^{-1} are evident in the reflectance data and have been accounted for in our model.

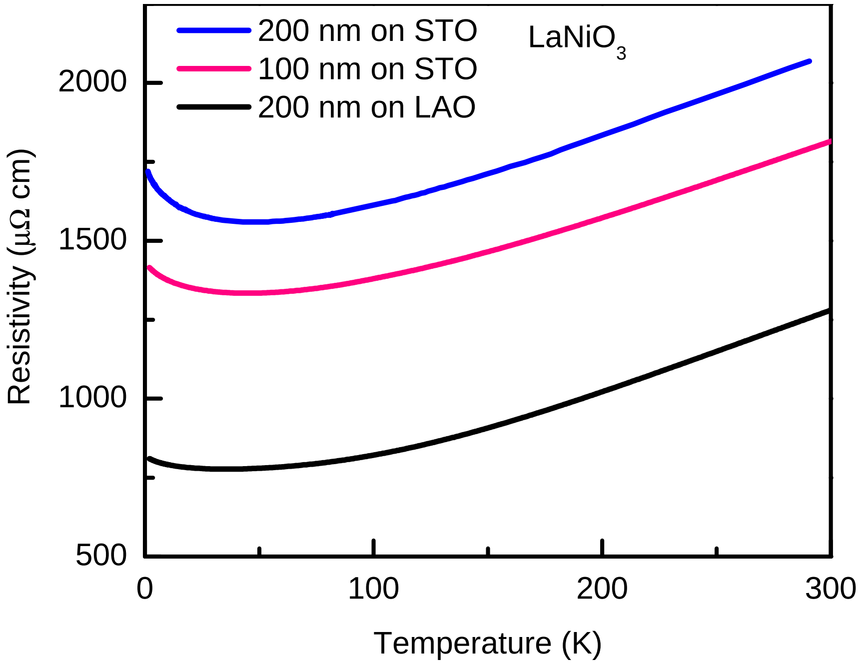

Figure 2.3: DC resistivity of the LNO films over a wide temperature range.

LDA band structure was computed within the FP-LAPW scheme [18] using room temperature bulk LNO structural parameters.[40] The calculations were performed on a 9x9x9 k-space grid with RKMAX set to 9.0, and converged to 0.1 mRy in energy and 0.0005 in charge distance.

2.3 Results and Discussion

Transport data in Fig. 2.3 show metallic behavior and reveal the resistivity of the films to be on the order of 1 mΩ cm. This value is in good agreement with previously reported transport data for similar films [66] and bulk LNO [123, 105]. The resistivity of our films is higher than that of ultrathin films of LNO,[138, 121] which we attribute to the difference in thickness. It is known that thickness and strain can strongly influence the transport properties of LNO thin films.[121] The

100-200 nm films used in this work are expected to be essentially strain-free while ultrathin films of thickness 20 nm or less contain at least a significant fraction that is subject to epitaxial strain due to the substrate. The resistivity data in Fig.2.3 show an upturn at low temperature. The same behavior is reported in Ref.[66] and is attributed to quantum corrections to the conductivity due to weak localization and renormalization of electron-electron interactions. A similar low temperature upturn in the resistivity has been observed in other correlated oxides.[1, 2, 47]

To gain insight into the electronic band structure of LNO it is useful to look at the optical conductivity, which is related to the complex dielectric function through the equation $\sigma(\omega) = \frac{i\omega[1-\epsilon(\omega)]}{4\pi}$. Figure 2.4 shows the real, dissipative part of the optical conductivity at room temperature. In the high energy region, above 1 eV, the main features of the optical conductivity, which we have labeled B-E, look similar for all the films. A more noticeable variation in the spectra is evident in the mid-IR region, presumably due to the effects of strain. While all samples show a peak in this region (A in Fig.2.4), the magnitude and shape is different for each film. In the far-IR range (note the change in scale), we see a broad peak centered at 300 cm^{-1}. In stark contrast with theoretical predictions, no well defined Drude peak is observed, indicative of very strong electronic correlations. Below we discuss in detail the data in these three regions. The similarity of the 100 nm and 200 nm films on STO seen in Fig.2.4, especially in the far-IR region, shows that the small fraction of secondary phases that may develop with increasing thickness do not significantly affect the optical conductivity of the films. Additionally, the similarity of the films on STO and LAO indicates that our data indeed reflect the properties of strain-free LNO.

The high energy optical conductivity we have acquired is consistent with earlier work on LNO ceramic samples.[4, 5] In Fig.2.5, we plot the calculated LDA partial density of states, which is in good agreement with previous band structure calculations.[113, 120, 87] LNO has a $t_{2g}^6 e_g^1$ electronic configuration, with the antibonding e_g states crossing the Fermi level. The inset in Fig.2.5 shows that the optical conductivity obtained from LDA calculations is in qualitative agreement with our experimental data. Based on the data in Fig.2.5 and using

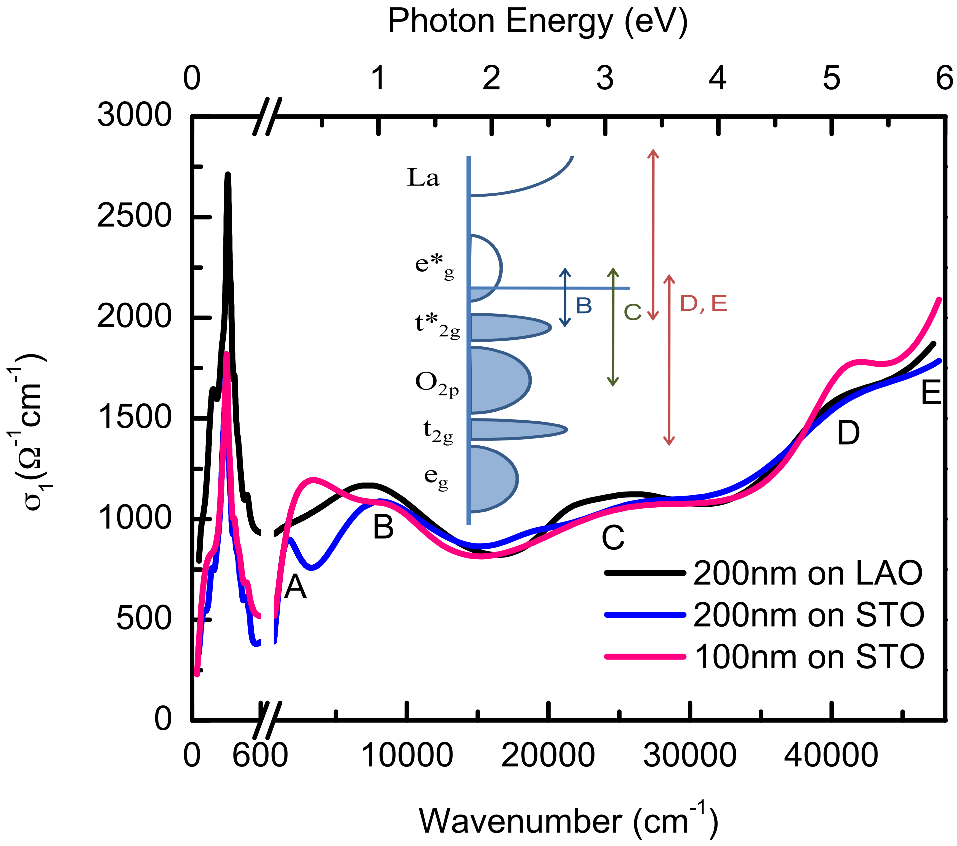

Figure 2.4: Real part of the optical conductivity of three different LNO films at room temperature. Note the change in scale at 600 cm^{-1}. Inset: rough sketch of the LNO density of states and interband transitions.

transition decomposition analysis of the LDA optical conductivity, we attempt to assign features B-D in Fig.2.4 to specific interband transitions (see inset in Fig.2.4). We suggest that B corresponds to transitions from the Ni $t*_{2g}$ and $e*_g$ levels to the Ni $e*_g$ orbitals . C could be due to transitions from the O $2p$ to the $e*_g$ orbitals. D and E may be the result of transitions from $t*_{2g}$ to the La $4f$ and $5d$ levels and from the bonding Ni e_g and t_{2g} orbitals to the $e*_g$ orbitals. Low temperature optical conductivity in this range is shown in the inset of Fig.2.6. All of the features remain unchanged down to 20 K. A small reduction of up to 5 % in the optical conductivity is evident between 1.5 and 4 eV.

Based on LDA calculations, feature A in the mid-IR region appears to be too low in energy to be an interband transition. However, given the failure of this model to accurately describe our low frequency data, it is possible that the $e*_g$ band is, in reality, significantly different from that obtained by these calculations. In this scenario, it can not be ruled out that this peak is indeed associated with an interband transition.

Alternatively, feature A could be a sign of some kind of electron localization. It is known that localization phenomena can give rise to a shift of the Drude peak to finite frequencies, due to the need of the electrons to overcome an energy barrier.[7] We note that the peak does seem to be centered at an unusually high energy compared to other materials where localization of electrons is present.[11, 9] Polaronic transport can also result in this type mid-IR absorption. Figure 2.6 shows low temperature infrared data for the 100 nm film on STO. Virtually no temperature dependence of this feature is observed down to 40 K. This behavior allows us to rule out the presence of small polarons, which would require a strong temperature dependence of the mid-IR absorption.[106] Large polaron absorption spectra, on the other hand, are expected to be temperature independent and asymmetric,[36] in agreement with our data. The peak position near 0.3 eV is also consistent with large polarons, as it is below the 0.7 eV cut off predicted by Fröhlich coupling for transition metal oxides [7]. It has also been suggested that this type of absorption could be due to incoherent motion of carriers coupled to the spin degree of freedom. [5] However, the lack of temperature dependence in

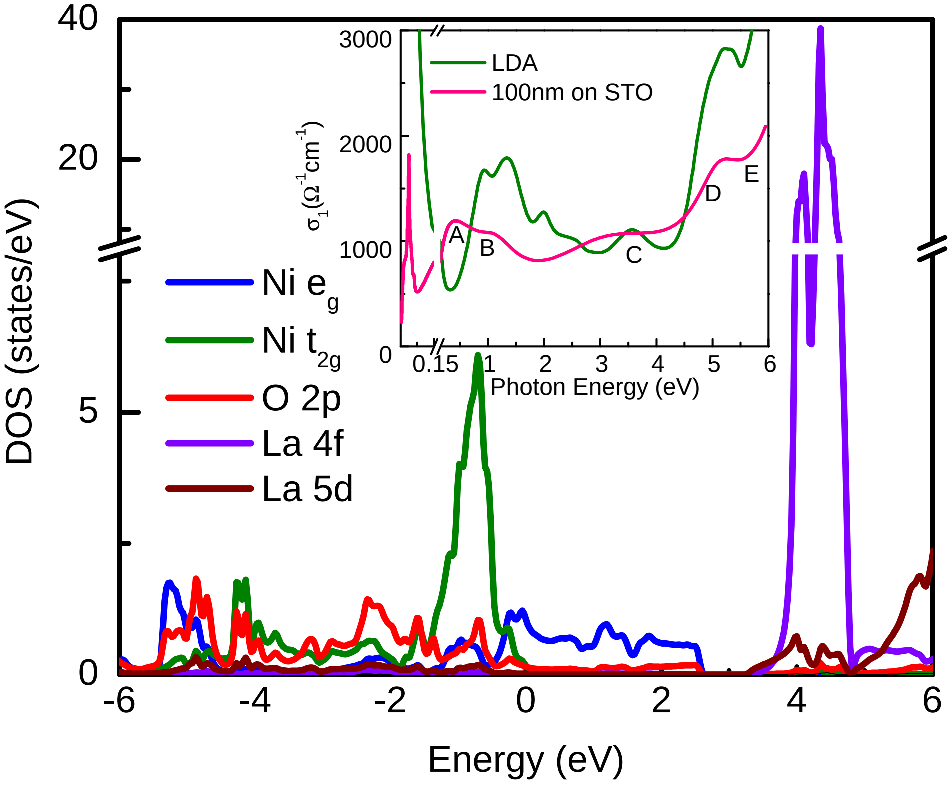

Figure 2.5: Partial LNO density of states obtained from LDA theory. Inset: comparison of the optical conductivity obtained experimentally for the 200 nm film of LNO on STO and that obtained from LDA calculations. The Drude peak produced by LDA theory is not present in the experimental data.

our data makes this an unlikely scenario.

We now focus our attention on the far-IR part of the spectra in Fig.2.4. Optical measurements are ideal for probing the kinetic energy of electrons, given that this quantity is proportional to the area under the Drude part of the optical conductivity, $K_{exp} \propto \int_0^\Omega \sigma_1(\omega) d\omega$.[83] Comparison of the experimental electron kinetic energy to that obtained from band structure calculationss, K_{band}, provides a means for classifying materials according to the strength of the electronic correlations in the system.[81, 103] The ratio K_{exp}/K_{band} is expected to be close to unity for itinerant electron systems and will become suppressed as strong interactions come into play, which are not included in K_{band}. Band structure calculations for LNO predict a finite density of states at the Fermi level and a plasma frequency $\omega_p = 3.7eV$. Data in Fig. 2.4 however, show no obvious sign of a Drude contribution to the optical conductivity. The plasma frequency obtained by integrating $\sigma_1(\omega)$ up to 1500 cm^{-1} is 1 eV for the film on LAO and 0.8 eV for the films on STO. This results in $K_{exp}/K_{band} \approx 0.05 - 0.07$, which is quite low, even compared to other correlated metals.[103] In this context, our data present robust evidence of very strong electronic correlations in LNO. These values are also low compared to those of ultrathin strained LNO films which, while still very strongly correlated, do exhibit a Drude peak.[92] This suggests that strain affects the electronic properties of LNO.

In contrast with other lanthanide rare earth nickelates,[60, 86] the strength of correlations in LNO does not appear to be tuned by temperature. The low temperature data in Fig.2.6 show no significant temperature dependence, except for the peak at 300 cm^{-1}, which we discuss below. Low temperature far-IR data have also been obtained for the film on LAO but are not shown here, as they exhibit the same trend as the data in Fig.2.6. We note that, even in the realm of strongly correlated systems, the low energy optical conductivity spectra we have obtained is unusual. Correlated metals typically show coherent (Drude) and incoherent contributions of similar strength. In the case of LNO, the incoherent part of the optical conductivity (feature A) is much stronger than the coherent one.

We now discuss the strong far-IR resonance shown in Figs. 2.4 and 2.6.

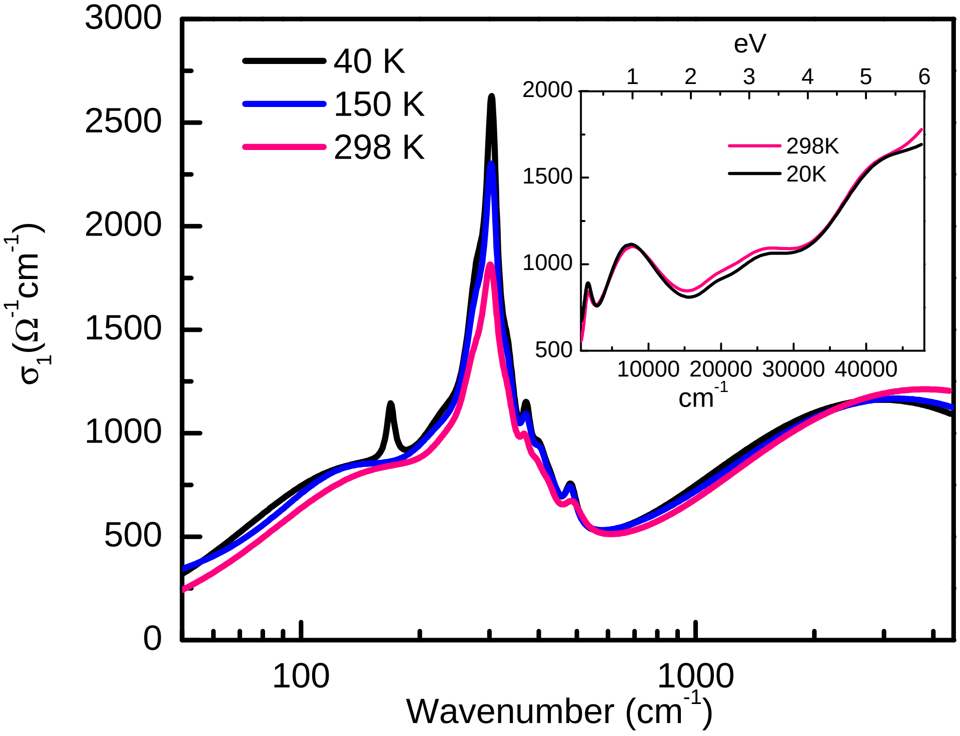

Figure 2.6: Low temperature optical conductivity of the 100 nm thick film on STO in the far-IR and mid-IR regions. Inset: optical conductivity of the 200 nm film on STO up to 6 eV at 298 and 20 K.

According to group theory, three infrared-active phonon modes are expected in this range for a cubic perovskite. The broad peak centered at 300 cm^{-1} is composed of much more than three oscillators. One possibility is that the modes are split and broadened due to the rhombohedral distortion of the LNO lattice. At 40 K, the strength of the main peak is increased by about 20% and a small peak is resolved at 170 cm^{-1} (Fig. 2.6) . This, along with some sharpening of the spectra at low temperature, is suggestive of absorption due to phonons. The effective ionic charge obtained from this resonance by means of the equation $\int \sigma_1(\omega)d\omega = \frac{\pi n Z^2}{2m*}$ is Z=2.5. While this value is somewhat high, it is not outside the range of known effective ionic charges in oxides.[5, 41] In nickelates, Z=1.9 has been obtained for $La_2NiO_{4+\delta}$.[98] As seen in Fig. 2.4, no thickness dependence of this feature is observed, with the 100 nm and 200 nm films on STO showing almost identical far-IR spectra. The film on LAO shows optical conductivity about 50% higher than the films on STO, consistent with resistivity data. The shape of the resonance however, is remarkably similar even though LAO has a rhombohedral perovskite crystal structure and STO is a cubic perovskite.

A recent x-ray photoemission study of LNO has found a dispersive e_g band crossing the Fermi energy, in apparent disagreement with our data.[35] A similar discrepancy between ARPES and infrared optical data has been reported for layered manganites and can be explained by the presence of a pseudogap at the Fermi energy.[65, 53] It is also important to note that LNO is a polar material in which electronic reconstruction at the surface is a likely possibility.[131] While the results of Ref.[35] show a 3-D Fermi surface with k_z band dispersion, the probing thickness of ARPES is still very small compared to infrared probes. It can not be ruled out that these data are a more accurate description of the electronic structure of LNO in the vicinity of a surface or interface than of bulk LNO.

2.4 Conclusions

We have obtained optical conductivity of various LNO thin films over a wide temperature and energy range. Above 1 eV, our data show several interband transition in good agreement with band structure calculations. At lower frequencies however, significant discrepancies with theory are evident. Despite band theory predictions of a finite density of states at the Fermi level, no Drude peak is present in our data. We claim that this is evidence of strong correlations in LNO, which must be taken into account by theoretical models used in the design of oxide heterostructures. We have shown that the strength of the electronic correlations is not controlled by temperature.

Acknowledgments

The authors thank A. J. Millis, S. J. Moon, and G. Sawatzky for useful discussion. Work at UCSD was supported by DOE-BES. J.C. was supported by DOD-ARO under the grant No. 0402-17291 and NSF grant No. DMR-0747808.

MBM was supported by DOE under grant No. DE FG02-04ER46105.

Chapter 3, in full, is a reprint of the material as it appears in J. of Appl. Phys. **110**, 033514 (2011). M. K. Stewart, J. Liu, R. K. Smith, B. C. Chapler, C.-H. Yee, D. Meyers, R. E. Baumbach, M. B. Maple, K. Haule, J. Chakhalian, and D. N. Basov. The dissertation author was the primary investigator and author of this paper.

Chapter 3

Optical study of strained ultrathin films of strongly correlated $LaNiO_3$

Abstract

An optical study of fully strained ultrathin $LaNiO_3$ films is presented and compared with LDA+DMFT calculations. $LaNiO_3$ films were grown by pulsed laser deposition on $LaAlO_3$ and $SrTiO_3$ substrates which provide compressive and tensile strain, respectively. Optical conductivity data show a Drude peak with a spectral weight that is significantly reduced compared to that obtained from LDA calculations. The extended Drude analysis reveals the presence of a pseudogap around 80 meV for the film on $SrTiO_3$ and near 40 meV, at low temperature only, for the film on LAO. An unusual temperature dependence of the optical conductivity is observed, with the Drude plasma frequency increasing by up to 20% at low temperature due to spectral weight transfer from bands lying 2-4 eV below the Fermi energy. Such a strong temperature dependence of the Drude spectral weight has previously been reported for correlated electron systems in which a phase transition is present. In LNO however, no phase transition is observed.

3.1 Introduction

Optical studies have been invaluable in the understanding of correlated electron systems, in part due to the optical sum rules which allow one to monitor redistributions of the electronic spectral weight associated with mobile and localized electrons.[82, 16, 7] One optical signature of correlations is especially notorious. The emergence of the conducting state in a correlated metal is usually associated with a dramatic transfer of the electronic spectral weight (SW) over many eV.[110, 27, 13, 111] A canonical manifestation of this trend is seen in V_2O_3 as this correlated oxide undergoes an insulator-to-metal transition (IMT). Specifically, in V_2O_3 one registers a SW transfer from the energy range dominated by the response of the Hubbard bands to the quasiparticle peak responsible for the Drude response in the metallic state, confirming the validity of the half-filled Hubbard model.[110, 6, 104] Because the IMT in this and in other correlated systems is accompanied by structural changes and/or electronic/magnetic phase separation, the role of these auxiliary factors in the SW transfer is difficult to disentangle from the direct impact of correlations.

In this work, we present an optical study of $LaNiO_3$ (LNO), a correlated oxide [123, 141, 92, 127] without additional complications due to phase transitions, spin or charge order, etc. This material is the only rare earth nickelate to remain metallic at all temperatures [137] and therefore offers the opportunity to study the dynamics of correlated electrons in its pure form, unobscured by structural or phase separation effects. The optical response of bulk LNO is unusual for a metal, showing no well defined Drude peak.[4, 127] While the ultrathin strained films discussed here do exhibit a Drude resonance, electronic correlations dominate every aspect of charge dynamics. We show that the seemingly conventional metallic temperature dependence of the DC resistivity in LNO is directly linked to the unexpected enhancement of the Drude SW at the expense of features attributable to Mott-Hubbard bands.

3.2 Methods

Epitaxial LNO films were grown by reflection high-energy electron diffraction (RHEED) controlled pulsed laser deposition on LAO and STO substrates with -1.2% and +1.7% lattice mismatch, respectively. The films are 30 unit cells thick with c-axis parameters of 3.86 Å on LAO and 3.78 Å on STO (see Table 3.1). Representative time-dependent RHEED specular intensity (RSI) is shown in Fig.3.1 for the LNO film on STO. A full recovery of RSI is observed after each unit-cell layer, characteristic of perfect layer-by-layer growth. The inset in Fig.3.1 shows the corresponding RHEED image with well defined spots and streaks at the (00) specular and the (01) and $(0\bar{1})$ off-specular reflections, indicative of a smooth surface morphology. Additionally, the films have been characterized by X-ray diffraction, X-ray absorption, AFM and TEM as shown in the appendix and in Ref.[24].

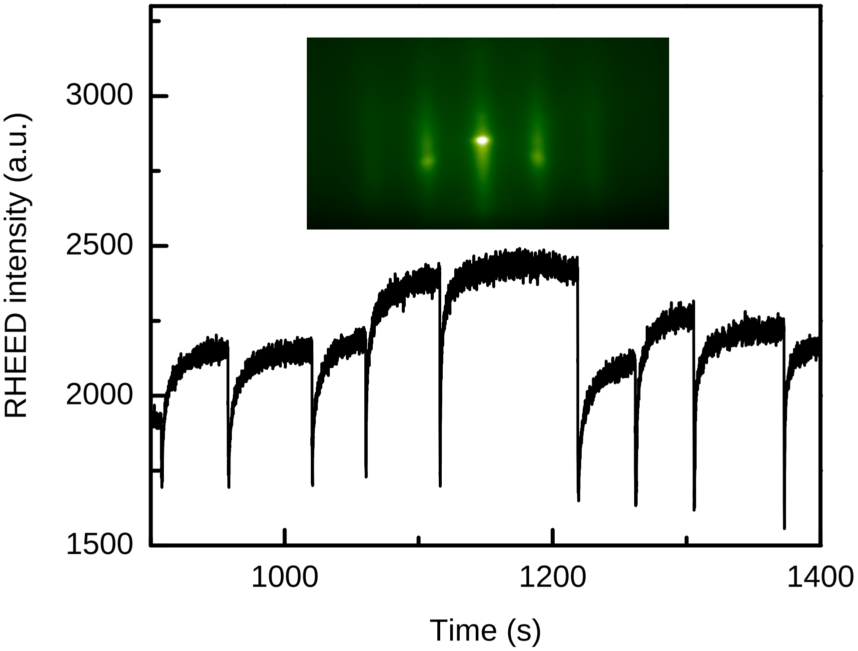

Figure 3.1: Representative RSI evolution during the growth of the LNO film on STO. Inset: corresponding RHEED image.

Optical studies of both the films and the bare substrates between 20 and 298 K were carried out using reflectance in the range from 6 to 85 meV and variable angle spectroscopic ellipsometry (VASE) in the range from 80 meV to 5.5

Table 3.1: Comparison of relevant theoretical and experimental parameters for LNO films on LAO and STO: lattice mismatch, *c*-axis parameters obtained from x-ray diffraction, Drude plasma frequency and scattering rate obtained from optics data at 298 K and 20 K, and ratio of the electron kinetic energy obtained from optics data and that obtained from LDA calculations (see text for details).

	Lattice mismatch(%)	*c*-axis (Å) (XRD)	ω_p 298 K (eV)	ω_p 20 K (eV)	$1/\tau(\omega \to 0)$ 298 K (cm^{-1})	$1/\tau(\omega \to 0)$ 20 K (cm^{-1})	K_{exp}/K_{LDA}
$LaNiO_3/LaAlO_3$	-1.2	3.86	1.11	1.29	468	265	0.11
$LaNiO_3/SrTiO_3$	+1.7	3.78	0.93	1.04	505	403	0.08

eV. Near-normal incidence reflectance measurements were performed in a Michelson interferometer (Bruker 66vs). Reflectance of the sample was first measured relative to a gold reference mirror and then normalized by the reflectance of the gold coated sample.[49] Ellipsometry measurements were performed with two commercial Woollam ellipsometers. The range from 80 to 550 meV was investigated with an IR-VASE model based on a Bruker 66vs. For the range between 0.6 and 6 eV we used a VASE model based on a grating monochromator. Both ellipsometers are equipped with home-built UHV chambers to allow low temperature measurements.[19] Ellipsometry measurements were performed at incidence angles of 60° and 75°. At each angle, the polarization state of the reflected light was measured in the form of two parameters, Ψ and Δ, which are related to the Fresnel reflection coefficients for p- and s- polarized light ($\tilde{R}_{pp}$ and $\tilde{R}_{ss}$) through the equation

$$\tilde{R} = \frac{\tilde{R}_{pp}}{\tilde{R}_{ss}} = tan(\Psi)e^{i\Delta}. \tag{3.1}$$

In order to obtain the optical constants from the raw reflectance and ellipsometry data, a model was created using multiple Kramers-Kronig consistent oscillators to describe the complex dielectric function of the sample.[68] The parameters in the model were then fitted to the experimental data using regression analysis with the WVASE32 software package from Woollam Co., Inc. In the case of the LNO films, the model consisted of two layers: a substrate characterized by the optical constants previously determined for either LAO or STO, and a thin film layer from which the optical constants of the film alone were obtained.[68] Since LAO and STO have several far-IR phonons with strong temperature dependence, the substrates were measured and modeled at all the same temperatures as the films. This allows us to use the appropriate temperature for the substrate layer in order to ensure that the temperature dependence observed in the extracted optical conductivity is indeed caused by the LNO films. Representative raw reflectance and ellipsometry data for the film on STO are plotted in Fig.3.2 along with the model fit.

We note that the crystal structure of the films is slightly anisotropic, with the c-axis lattice parameter about 1.5 % larger (smaller) than the in-plane lattice

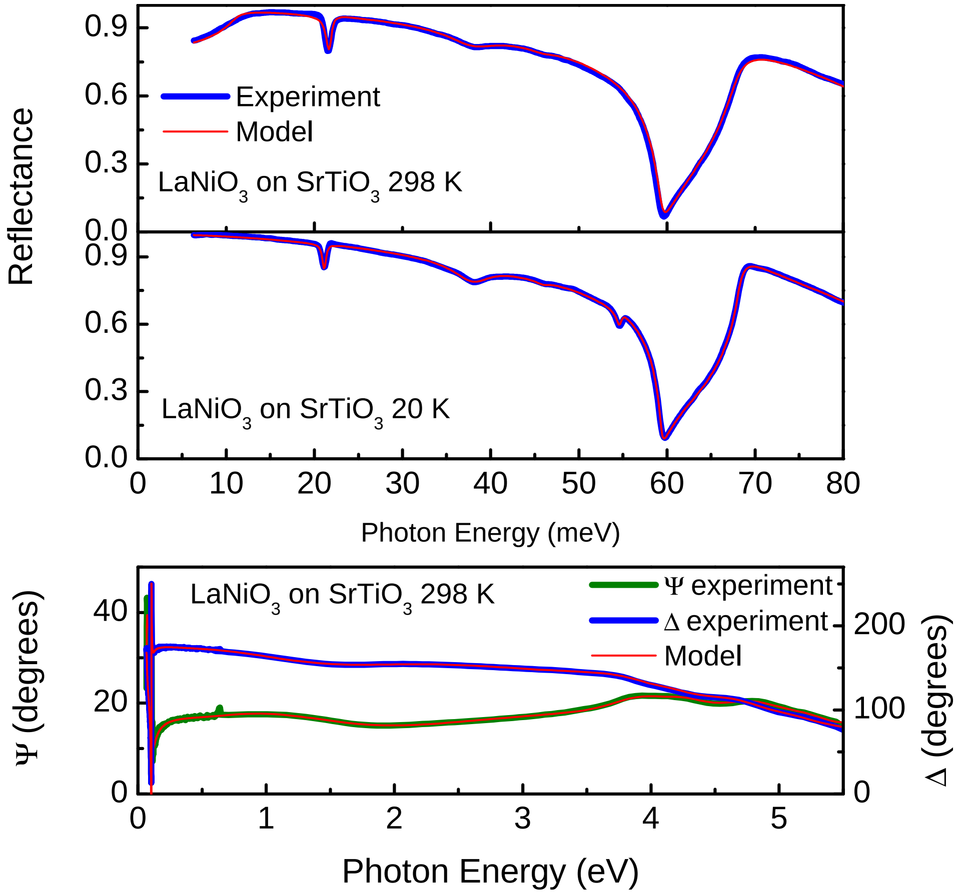

Figure 3.2: Raw reflectance and ellipsometry data for the LNO film on STO plotted with the model fit.

parameter for the LNO film on LAO (STO). In order to asses the effects of this anisotropy in our optical data, we performed room temperature ellipsometric measurements for the LNO film on LAO in which the position of the polarizer was varied and tracked. In this way it was possible to obtain the ratios of the diagonal and off-diagonal components of the Jones matrix

$$J = \begin{bmatrix} \tilde{R}_{pp} & \tilde{R}_{sp} \\ \tilde{R}_{sp} & \tilde{R}_{ss} \end{bmatrix}, \tag{3.2}$$

which is a diagonal matrix when the sample is completely isotropic. We found that the magnitudes of both the real and imaginary parts of $\tilde{R}_{ps}/\tilde{R}_{pp}$ and $\tilde{R}_{sp}/\tilde{R}_{ss}$ were between 0.003 and 0.012 in the the range from 0.6 to 6 eV. This means that the off-diagonal components of the Jones matrix are only about 1% of the diagonal components, approximately the same as the noise level in our measurements. Additionally, modeling using c-axis and ab-plane optical constants obtained from LDA+DMFT calculations for strained films indicates that our measurements are dominated by the in-plane response and the effect of this anisotropy on the measured ellipsometric parameters is only evident above ~1.5 eV and is very small. We therefore conclude that the anisotropy of the crystal structure only minimally affects our measurements and the use of an isotropic model for our analysis is appropriate.

Charge self-consistent LDA+DMFT [64] calculations were performed using the implementation described in Ref. [45]. We used U=7.3 eV and J=1 eV for the strength of the Coulomb repulsion on Ni-d orbitals, and $E_{DC} = U * (n_d - 1/2) - J(n_d - 1)/2$ as the standard double counting energy, where n_d=7.3 is the average d valence. A range for J and U was determined based on previous studies of this class of compounds and then scanned to obtain the best fit to our optics data as well as to ARPES [35] and thermal measurements.[105] In order to compute the optical conductivity, we analytically continued the self-energy using modified Gaussians [45] and cross-checked the result with maximum entropy. The conductivity was then computed using the DFT momentum matrix elements and convolving the correlated Green's function for all values between -6 eV and 6 eV, relative to the Fermi level.

3.3 Results and Discussion

3.3.1 Optical conductivity: general trends

Figure 3.3 shows the real part of the optical conductivity, given by $\sigma(\omega) = \frac{i\omega[1-\epsilon(\omega)]}{4\pi}$, for the LNO films on LAO and STO at various temperatures. In both films, a Drude peak typical of metals is evident at low frequencies, along with three phonon modes. Additionally, four peaks (A-D in Fig.3.3) can be clearly identified at higher energies. These can be assigned to interband transitions by comparing to LDA theory. The inset in Fig.3.3 shows a sketch of the LNO density of states (DOS) based on LDA calculations,[127, 113, 120, 87] indicating a $t_{2g}^6 e_g^1$ electronic

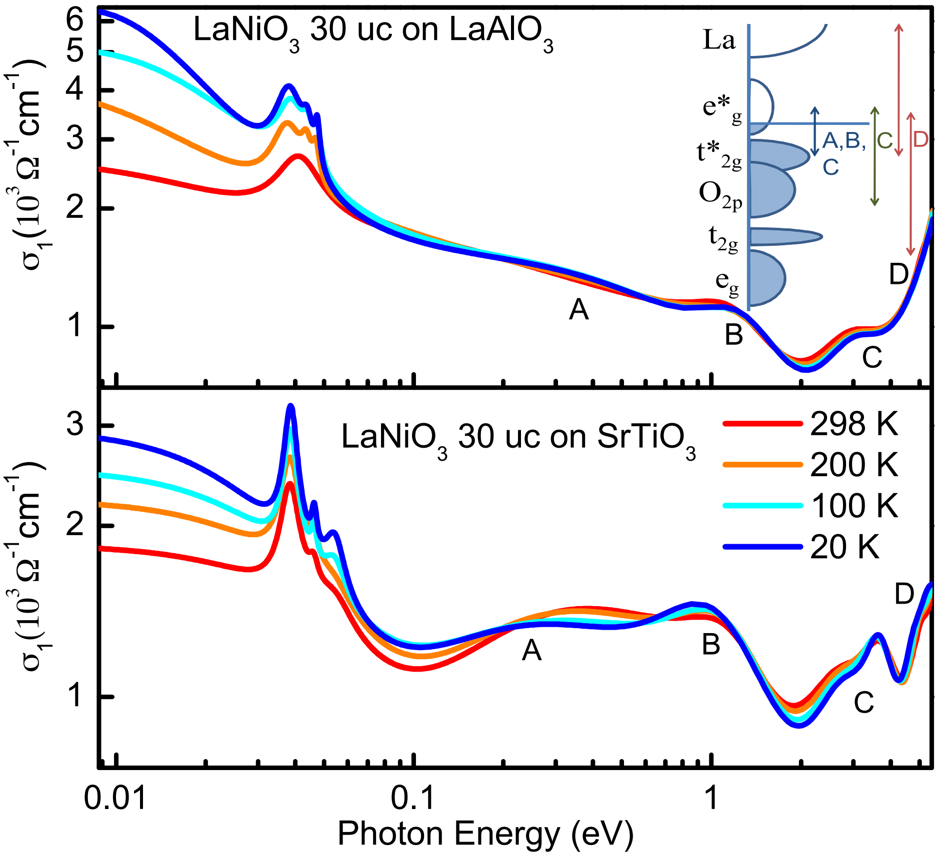

Figure 3.3: Real part of the optical conductivity of fully strained LNO films on LAO (top panel) and STO (botton panel) substrates plotted on a log-log scale. Inset: sketch of the LNO density of states and interband transitions based on LDA calculations.

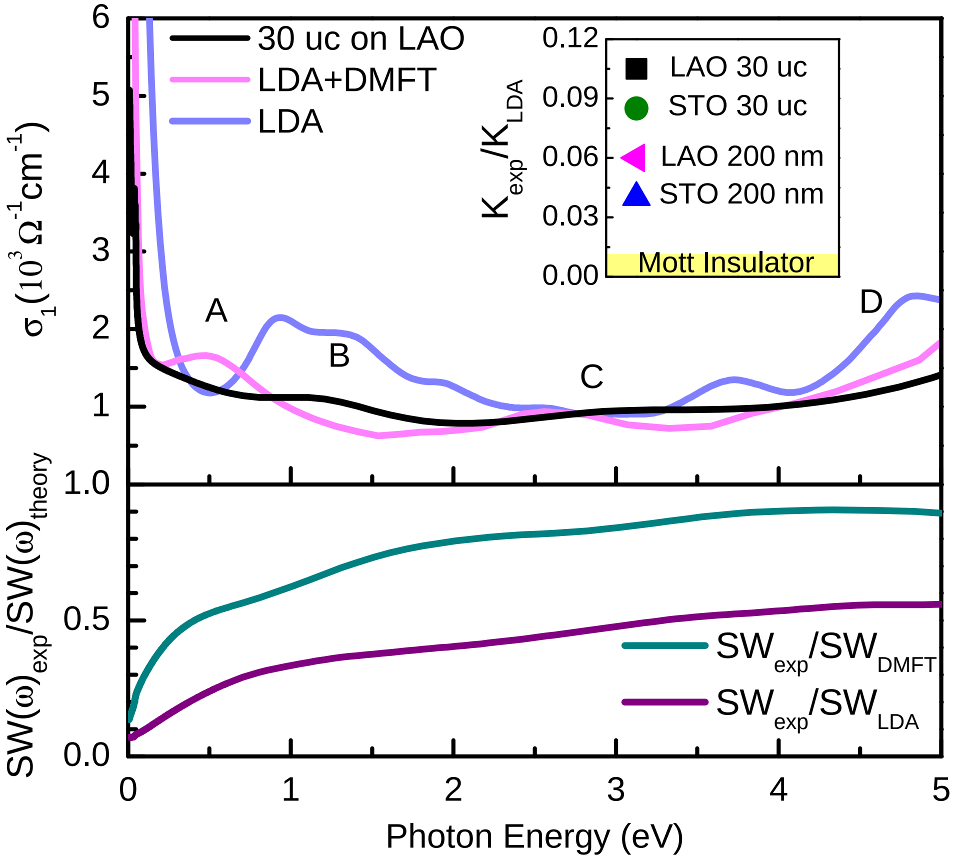

Figure 3.4: Top panel: Real part of the optical conductivity of a 30 unit cell thick LNO film on LAO substrate obtained at 100 K, plotted with the optical conductivity obtained from LDA and LDA+DMFT calculations for strained LNO on LAO at 116 K. Inset: ratio of the experimental electron kinetic energy at room temperature for LNO thin films of different thickness grown on LAO and STO substrates and the LDA kinetic energy. This ratio approaches zero for Mott insulators. Bottom panel: Ratio of the spectral weight obtained from experimental data and that obtained from two different theoretical calculations: LDA and LDA+DMFT.

Table 3.2: Assignment of interband transitions based on LDA transition decomposition analysis.

A and B	C	D
${e^*}_g \rightarrow {e^*}_g$	${t^*}_{2g} \rightarrow {e^*}_g$	Ni $3d \rightarrow$ Ni $3d^*$
${t^*}_{2g} \rightarrow {e^*}_g$	O $2p \rightarrow {e^*}_g$	Ni $3d^* \rightarrow$ La $4f$
		Ni $3d^* \rightarrow$ La $5d$

configuration, with the antibonding ${e^*}_g$ states crossing the Fermi level. Figure 3.4 shows $\sigma_1(\omega)$ of the film on LAO at 100 K along with those obtained from LDA and from LDA+DMFT. The latter was calculated for strained LNO on LAO at 116 K. Using transition decomposition analysis of the LDA optical conductivity we arrive at the assignment of interband transitions reported in Table 3.2.

According to Fig.3.4, LDA+DMFT provides a more accurate description of our experimental data than LDA does. In particular, feature A is not evident in the LDA $\sigma_1(\omega)$ but is present in the LDA+DMFT results. The two peaks seen at 1 eV and 1.5 eV (A and B, respectively) in LDA shift to lower energy when correlations are included in LDA+DMFT, resulting in better agreement with experiment. In this picture, feature A is due to interband transitions from the ${t^*}_{2g}$ and ${e^*}_g$ orbitals. A redshift of feature C is also evident in LDA+DMFT, consistent with the scenario in which electronic correlations suppress the energy of interband transitions due to the quasiparticle renormalization. We note that, even though the LDA+DMFT results reproduce the key experimental trends, the agreement is less than perfect. This is not surprising given that optics is one of the most challenging probes to match well theoretically. This is because the description of the optics data relies on the convolution of two Green's functions, which in turn is very sensitive to any small errors in the individual Green's functions.

3.3.2 Extended Drude analysis

In considering the low frequency part of the spectra, it is instructive to first review the usual behavior of the optical conductivity in conventional metals. The free electron (Drude) contribution to the optical conductivity can be described in terms of the electron scattering rate $1/\tau$ using the equation

$$\sigma_{Drude} = \frac{ne^2\tau}{m}\frac{1}{1-i\omega\tau}. \tag{3.3}$$

In conventional conductors, $1/\tau$ and the carrier mass m are frequency independent and $1/\tau$ decreases with decreasing temperature. This results in an increase in the amplitude and narrowing of the Drude peak. The low and high temperature optical conductivity curves tend to cross before the onset of interband transitions and the Drude plasma frequency remains constant with temperature. The data shown in Fig.3.3, which are also plotted on a linear scale in the top panels of Fig.3.6, differ from this description. While the amplitude of the Drude peak increases at low temperature for both films, the narrowing of the Drude peak is not very pronounced, as discussed below.

To understand how our data deviate from the conventional Drude theory, we make use of the extended Drude analysis. Within this framework, the scattering rate $1/\tau(\omega)$ and the mass renormalization factor $m^*(\omega)/m_b$ are understood to be frequency dependent and are given by [13]

$$\frac{1}{\tau(\omega)} = -\frac{\omega_p^2}{\omega} Im\left(\frac{1}{\tilde{\varepsilon}(\omega)-\varepsilon_\infty}\right). \tag{3.4}$$

$$\frac{m^*(\omega)}{m_b} = -\frac{\omega_p^2}{\omega^2} Re\left(\frac{1}{\tilde{\varepsilon}(\omega)-\varepsilon_\infty}\right). \tag{3.5}$$

Here m_b is the carrier band mass and ω_p is the Drude plasma frequency given by

$$\frac{\omega_p^2}{8} = \int_0^\Omega \sigma_1 d\omega = \frac{4\pi ne^2}{m}, \tag{3.6}$$

with Ω=125 meV. This cut-off was selected to lie between the Drude peak and the onset of interband transitions and provides an upper limit for ω_p. Fig.3.5 (b) shows $1/\tau(\omega \to 0)$ obtained from Eq. (3.4). While $1/\tau$ decreases at low temperature, by 20% for the film on STO and by 40% for the film on LAO, the change is not sufficient to account for the increase in DC conductivity. This deficiency is compensated by an increase in the ω_p of up to 20% (Fig.3.5 (a)), an unusual effect that can be understood as a transfer of spectral weight to the Drude peak and is discussed further in section 3.3.3.

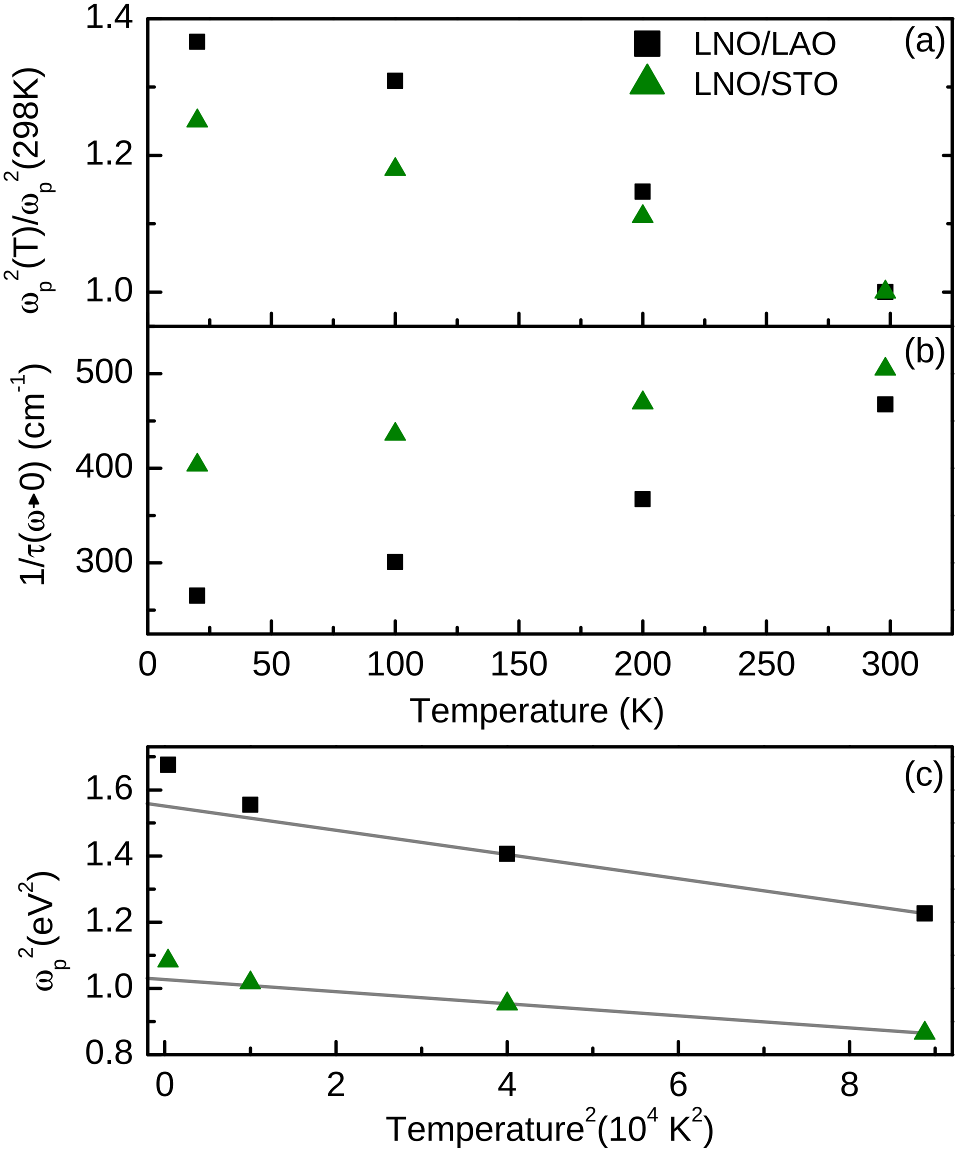

Figure 3.5: (a): Ratio of the Drude plasma frequency at low temperature and at 298 K squared, obtained by integrating the real part of the optical conductivity up to 125 meV. (b): Scattering rate in the zero frequency limit obtained from the extended Drude analysis. (c): Drude plasma frequency squared plotted as a function of the temperature squared.

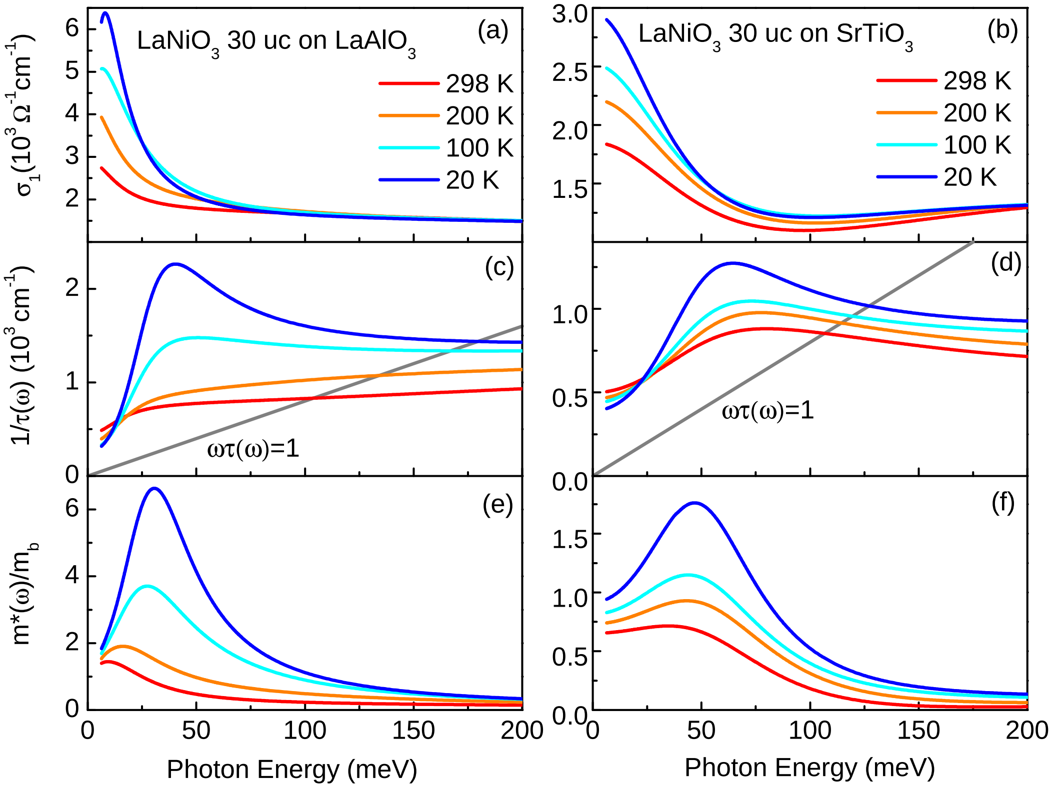

Figure 3.6: Results of the extended Drude analysis for LNO films on LAO (left panels) and on STO (right panels). (a and b): Real part of the optical conductivity after subtraction of the phonon contribution. (c and d): frequency dependent scattering rate. (e and f): frequency dependent mass renormalization factor.

Figure 3.6 shows the results of the extended Drude analysis, along with $\sigma_1(\omega)$ in the same energy range after subtraction of the phonon contribution. As shown in Fig.3.6(e and f), the mass enhancement is strongly temperature and frequency dependent. $m^*(\omega)/m_b$ increases with decreasing temperature and peaks around 50 meV. We note that $m^*(\omega)/m_b$ is larger for the film on LAO that for the film on STO, especially at low temperature.

As seen in Fig.3.6(c and d), the low frequency scattering rate of the carriers is larger than their energy ω. This is in contrast with the relation $1/\tau(\omega) < \omega$ characteristic of well defined quasiparticles in a Fermi liquid,[13] and is consistent with the argument for strong electronic correlations in LNO (see section 3.3.4). For the film on STO (Fig.3.6(d)) , $1/\tau(\omega)$ exhibits a peak around 70 meV which increases in magnitude as the temperature is lowered. This type of behavior in $1/\tau(\omega)$ has been attributed to the presence of a pseudogap in other correlated oxides such as underdoped cuprates [10, 100, 12] and the metallic puddles in phase separated VO_2.[101] The redshift seen in the peak at low temperature suggests that the magnitude of the gap decreases from 80 meV at 298 K to 65 meV at 20 K. The presence of a pseudogap is also supported by the minimum in the optical conductivity seen in Fig.3.6(b). For the film on LAO, a peak in $1/\tau(\omega)$ is evident around 40 meV at 20 K and 100 K only (Fig.3.6(c)), suggesting that a pseudogap develops as the temperatures is lowered. The magnitude of the pseudogap is smaller than for the film on STO and a clear sign of gapping is not apparent in the optical conductivity in Fig.3.6(a).

3.3.3 Temperature dependence

To understand the origin of the anomalous enhancement of the Drude SW, it is useful to look at the ratio of $\sigma_1(\omega)$ at low temperatures and that at 298 K, shown in Fig.3.7. It is apparent from Fig.3.7 that the temperature dependence of features A and B can be explained as a transfer of SW from one to the other and is opposite in the two films. For the film on LAO (STO), the SW of feature A increases (decreases) and that of feature B decreases (increases) at low temperature. This difference between the two samples could be due to strain, as tensile and

Table 3.3: SW of the Drude peak and of feature C at 20 K minus the SW at 298 K for the LNO films on LAO and STO.

	ΔSW_{Drude} (10^5 cm^{-2})	ΔSW_C (10^5 cm^{-2})
LNO/LAO	7.23	-7.15
LNO/STO	3.61	-3.39

compressive strains have been shown to have different effects on the e_g orbitals and DOS in LNO.[24] The reduction in $\sigma_1(\omega)$ between 1.5 and 3.5 eV is more significant and suggests that the enhanced low temperature Drude SW originates from the electronic states responsible for feature C (see Table 3.2). In order to quantify this, we consider the change in SW of the Drude peak ΔSW_{Drude} and of feature C ΔSW_C between 20 K and 298 K, as shown in Table 3.3. The ΔSW_{Drude} and ΔSW_C values are within a few percent of each other for both films, providing strong evidence of SW transfer between feature C and the Drude peak. We note that most of the changes in the Drude part of $\sigma_1(\omega)$ are off the scale in Fig.3.7 and may be more clearly seen in Fig.3.5(a). Given U=7.3 eV for LNO, the SW transfer seen in our data appears to be consistent with the canonical half-filled band Hubbard model, in which a SW transfer from the Hubbard band at $U/2$ to the quasiparticle peak is expected.[110] Thus, a similar phenomenology of spectral weight transfer is maintained in LNO despite the fact that the simplest version of the Hubbard band picture needs to be revised for this multiband system with quarter filled e_g bands.

Temperature driven changes in ω_p, along with high energy effects in $\sigma_1(\omega)$, have been observed in several correlated electron systems systems such as high-T$_c$ cuprates,[14, 61] manganites [27, 111] and V_2O_3.[110] As seen Fig.3.5(c), the Drude SW plotted as a function of the temperature squared is consistent with a linear behavior. While a T^2/W (where W is the bandwidth) dependence of the SW can be attributed to thermal smearing of the Fermi-Dirac distribution function as given by the Sommerfeld model, these effects are expected to be quite mild in magnitude, unlike the 35% increase in ω_p^2 seen in our data. A T^2 dependence has also been observed in the normal state of high-T_c cuprates,[85, 33, 91] in which

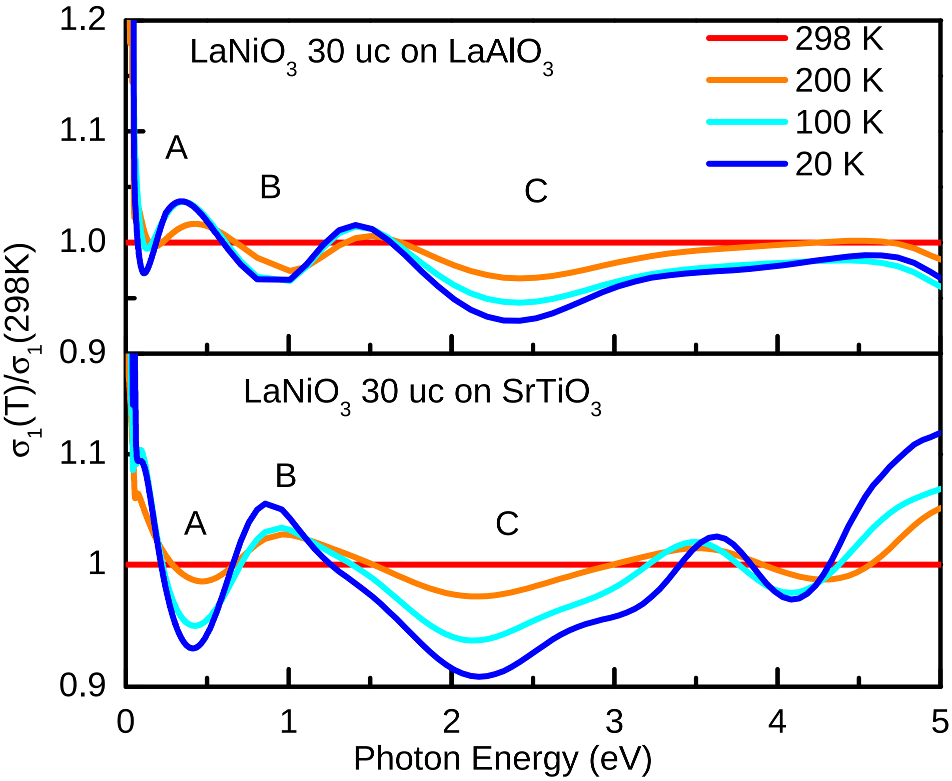

Figure 3.7: Ratio of the optical conductivity at low temperatures and the optical conductivity at 298 K for the LNO films on LAO (top panel) and on STO (bottom panels).

even changes on the order of 2% are considered to be large based on the bandwidth $W \sim 2$ eV. This deviation from the Sommerfeld model in the cuprates has been attributed to electronic correlations which extend the temperature dependence of the carrier response to energies on the order of U.[91] A direct comparison between the 2-D, single band model in Ref. [91] and our data is not possible since LNO is a multiband, 3-D system. However, given that the e_g bandwidth in LNO is ~ 4 eV, the observed temperature dependence of ω_p is quite substantial and, to our knowledge, unprecedented in the absence of a phase transition.

We note that, since the rest of the lanthanide rare earth nickelates do exhibit an IMT, it is likely that LNO is also close to localization even if it remains metallic at all temperatures. The spectral weight transfer from the low energy Drude peak into the incoherent contribution to the optical conductivity at higher energy is in qualitative agreement with the basic prediction of the DMFT for systems near the Mott transition.[110] Our system specific calculations indeed show that with increasing temperature, the Drude spectral weight gets redistributed to higher energy. However, due to the difficulty associated with the analytic continuation of the Monte Carlo data from the imaginary to the real axis, the precision of the conductivity beyond 1eV is limited, hence we can not determine the theoretical temperature dependence of feature C.

3.3.4 Electronic kinetic energy

In earlier work, we reported on the optical properties of LNO films of thickness 100-200 nm, which are expected to be relatively strain free and bulk-like.[127] As in the case of LNO ceramics,[4] no well defined Drude peak was observed in the optical conductivity of these films, presumably due to a combination of enhanced scattering and strong electronic correlations in this material. The fully strained films discussed in this paper and in Ref.[92], on the other hand, do exhibit a Drude peak in the optical conductivity (Fig.3.3). However, our data show that electronic correlations are still very strong in these films, albeit possibly not as strong as in bulk LNO. In an attempt to quantify and compare the strength of electronic correlations of various LNO films, it is useful to consider the ratio of the electron kinetic energy obtained experimentally and that obtained from band structure calculations K_{exp}/K_{LDA}.[81, 103] This ratio is close to unity for conventional metals and becomes suppressed when strong electronic correlations come into play. K_{exp} can be obtained from optical measurements by integrating the Drude contribution of the optical conductivity,[83]

$$K_{exp} = \frac{\hbar c_0}{e^2} \int_0^{\Omega} \frac{2\hbar}{\pi} \sigma_1(\omega) d\omega. \tag{3.7}$$

Here c_0 is the c-axis lattice parameter and Ω is the frequency cut-off chosen such that interband transitions are excluded from the integral.

The inset in Fig.3.4 shows K_{exp}/K_{LDA} for various LNO thin film samples at room temperature obtained by integrating $\sigma_1(\omega)$ up to 125 meV, the same cut-off used to obtain ω_p in Fig.3.5. The same K_{LDA} was used for all the samples. It is clear that K_{exp} is very strongly suppressed with respect to the LDA prediction, regardless of the substrate and thickness of the film. The highest value was obtained for the 30 u.c. film on LAO, K_{exp}/K_{LDA}=0.11, which is very low even compared to other correlated oxides.[103] The data in the inset in Fig.3.4 suggest that tensile and compressive strain both reduce the strength of correlations in LNO. While it may seem unexpected that both types of strain have a similar effect on the LNO films, we note that the symmetry of the crystal structure is reduced in strained films relative to the bulk, regardless of whether the lattice mismatch is positive or negative. This is due to the epitaxial constraint that removes the 3-fold rotation about the main $R\bar{3}/c$ axis [74] and could be the cause for the increased metallicity of the strained films. Furthermore, it has been shown that the tendency to charge and bond disproportionation is suppressed not only when compressive strain is applied, but also under tensile strain due to the dynamic breathing mode adopted by the oxygen octahedra.[24] Since charge order is the leading cause for the insulating state in nickelates, it can be expected that factors that suppress charge disproportionation will also increase the metallicity of the films. Our data show that this is indeed the case and that the increase in the metallicity is associated with a stronger coherent contribution to the optical conductivity.

The K_{exp}/K_{LDA} values we have obtained are somewhat lower than those reported in Ref.[92]. Specifically, for a film on LAO they report a mass enhancement of 3 equivalent to $K_{exp}/K_{LDA} = 0.33$, three times higher than our result. Although measurements for a film on STO are not reported, we can estimate from Fig.3 in Ref.[92] that an LNO film subject to 1.7% of tensile strain could have mass enhancement of roughly 4, or $K_{exp}/K_{LDA} = 0.25$. This difference is, at least in part, likely due to the choice of integration cut-off Ω. The authors of Ref.[92] have chosen $\Omega = 0.2$ eV while in this work we use $\Omega = 0.125$ eV in order to exclude the spectral weight of feature A. Because of the scale on which the optical conductivity is shown in Ref.[92] it is hard to assess whether such a feature is present in their data.

While K_{exp}/K_{LDA} depends on the selection of Ω (Eq.(3.7)), it is important to note that the argument for strong electronic correlations in LNO holds regardless of what cut-off is chosen. The bottom panel in Fig.3.4 shows the ratio of the spectral weight $SW(\omega) = \int_0^{\omega} \sigma(\omega')d\omega'$ obtained from experimental data and that obtained from LDA calculations. $SW(\omega)$ represents the effective number of carriers contributing to absorption at a given frequency and $SW(\Omega)$ is proportional to K_{exp}. While $SW(\omega)_{exp}/SW(\omega)_{LDA}$ increases with increasing frequency, it remains less than unity over the entire energy range. This shows that, independent of the cut-off frequency used to obtain K_{exp}, LNO is very strongly correlated. The other curve in the bottom panel of Fig.3.4 shows the spectral weight ratio using LDA+DMFT instead of LDA. Including electronic correlations in the theoretical calculations provides a more realistic description of LNO, resulting in a spectral weight ratio that is closer to unity.

3.3.5 Tensile vs. compressive strain

We now compare the effects of tensile and compressive strain on the optical and electronic properties of the LNO films and discuss the findings (see also Table 3.1). Even though the symmetry of the crystal structure in both LNO strained films is reduced relative to the bulk, the films on LAO and STO adopt different lower symmetry space groups ($C2/c$ and $P2_1/c$ respectively).[74, 24] For this reason, some differences in the optical response of the two films can be expected. As shown in Figs.3.3 and 3.6 the film on LAO has higher $\sigma_1(\omega \rightarrow 0)$ than the film on

STO. According to Eqs.(3.3) and (3.6), the DC conductivity is inversely proportional to $1/\tau$ and proportional to ω_p^2. As seen in Fig.3.5(b), $1/\tau$ is higher for the film on STO than for the film on LAO. However, this difference is not sufficient to account for the decreased DC conductivity. At 298 K, $\tau_{LAO}/\tau_{STO} = 1.07$ while $\rho_{STO}/\rho_{LAO} = 1.3$. This means that an increased Drude spectral weight for the film on LAO must be included to account for the difference in the conductivity (Fig.3.5(a)). While $1/\tau$ decreases more rapidly for the film on LAO with decreasing temperature, ω_p remains higher at all temperatures, suggesting that the increased scattering and the reduced Drude spectral weight are jointly responsible for the lower conductivity of the film on STO.

In the context of electronic correlations, the higher ω_p observed for the film on LAO (Fig.3.5 (a)) means that K_{exp}/K_{LDA} is larger for the film on LAO than for the film on STO (see inset in Fig.3.4), i.e. the film subject to tensile strain is more strongly correlated than the film with compressive strain. Furthermore, features B and C are centered at lower frequency for the film on STO than the one on LAO. This is consistent with the hypothesis that electronic correlations suppress the energy of interband transitions (Section 3.3.1), as these would be red-shifted more in the film with stronger correlations, the film on STO. Our finding is in agreement with X-ray linear dichroism data showing that compressive strain suppresses the tendency to charge and bond disproportionation more so than tensile strain,[24] which could increase the coherent response of the carriers for the film on LAO. Finally, our results are also consistent with the data in Ref.[92] showing a larger mass enhancement for the films subject to tensile strain than to compressive strain.

3.4 Conclusions

Our optical study of strained LNO films reveals that, despite the improved metallicity observed in these samples relative to the bulk, three canonical properties of correlated systems are retained: i) a suppression in the ratio K_{exp}/K_{LDA}, ii) a pseudogap and iii) a striking increase in ω_p at low temperature. This latter effect is particularly relevant for the understanding of correlated electron systems, as

SW changes of this magnitude have not been previously observed in a correlated system without a phase transition. This result indicates that the low temperature enhancement of the Drude SW can be considered an intrinsic property brought on by electronic correlations, showing that ω_p can be tuned with temperature even in the absence of an IMT.

Finally, we briefly discuss our results in the context of the recent theoretical proposal to mimic the gross features of the cuprate d-bands in nickelates through heterostructuring.[44] Some similarities can be found between LNO and the high-T_c cuprates based on our data. As described above, the temperature dependence of the Drude spectral weight is linear with T^2 (Fig.3.5(c)). This behavior is consistent with that observed in the normal state of several cuprate superconductors.[85, 33, 91] Additionally, features A-C present in the optical conductivity (Fig.3.3) are also seen in the cuprates.[29] Furthermore, even though our results show an increased metallicity of the strained films relative to bulk LNO, the strength of electronic correlations, possibly a key ingredient for superconductivity,[103] remains quite high. Reference [44] suggests that the presence of tensile strain will be beneficial in the attempt to induce superconductivity in LNO heterostructures. While our data show that strain increases the metallicity of the films, it is the film subject to compressive strain that has the highest conductivity. Therefore, it can not be concluded from our data that tensile strain is more favorable that compressive strain.

Acknowledgments

Work at UCSD was supported by DOE-BES. J.C. was supported by DOD-ARO under the grant No. 0402-17291 and NSF grant No. DMR-0747808.

Chapter 4, in full, is a reprint of the material as it appears in Phys. Rev. B. **83**, 075125 (2011). M. K. Stewart, C.-H. Yee, J. Liu, M. Kareev, R. K. Smith, B. C. Chapler, M. Varela, P. J. Ryan, K. Haule, J. Chakhalian, and D. N. Basov. The dissertation author was the primary investigator and author of this paper.

Appendix: Sample characterization

In addition to the RHEED measurements shown in Fig.3.1, the samples have been fully characterized using a variety of techniques to ensure the high quality of the films. The top panel of Fig.3.8 shows a 2 μm x 2 μm AFM image of a 30 uc LNO film on TiO_2-terminated STO.[59] The image indicates that the sample surface is atomically flat with surface roughness less than 75 pm and preserved vicinal steps. High-resolution cross-sectional TEM imaging (bottom panel of Fig.3.8) shows a coherent, defect-free film structure and an atomically sharp interface with no cation interdiffusion. Reciprocal space maps of the LNO (222) reflections obtained with X-ray diffraction for 10 uc LNO films on LAO and on STO can be seen in Fig.3.9. The in-plane components are perfectly matched with respect to the substrates, confirming the fully strained state of the films.

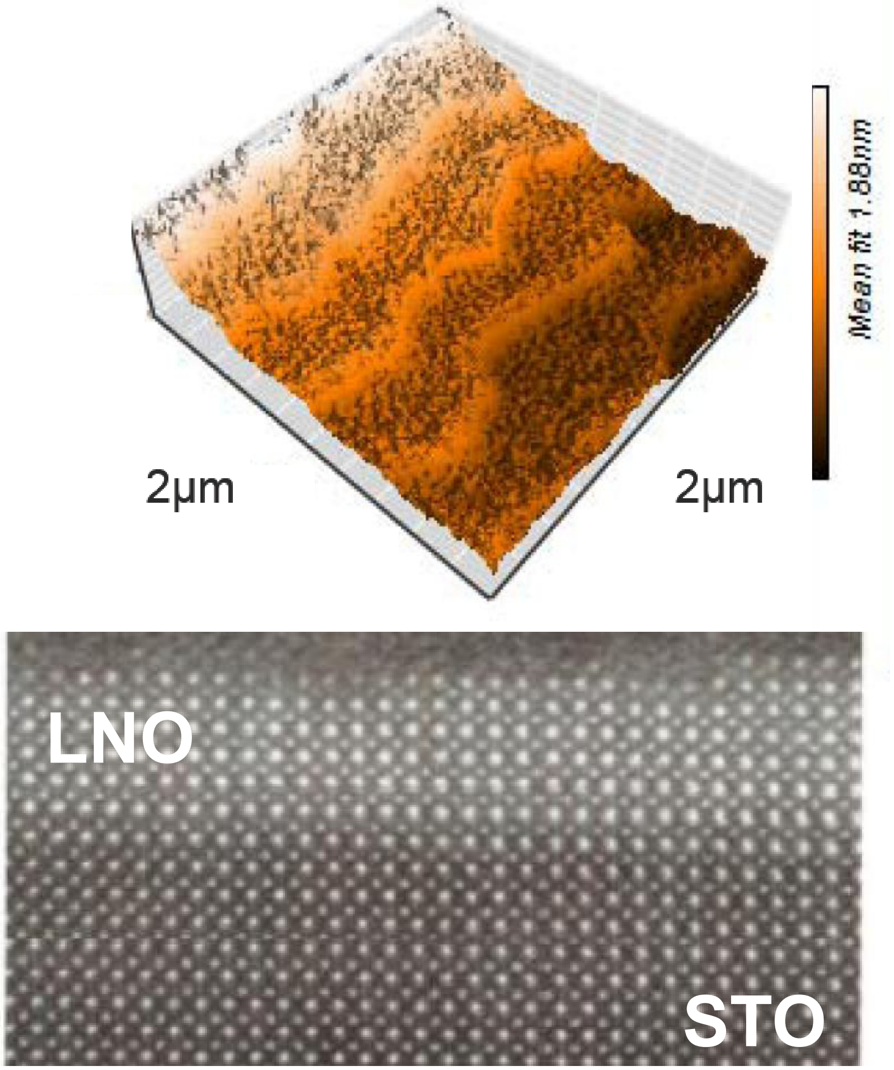

Figure 3.8: Top: AFM surface image of a 30 uc film of LNO on STO. Bottom: TEM image of a 10 uc film of LNO on STO.

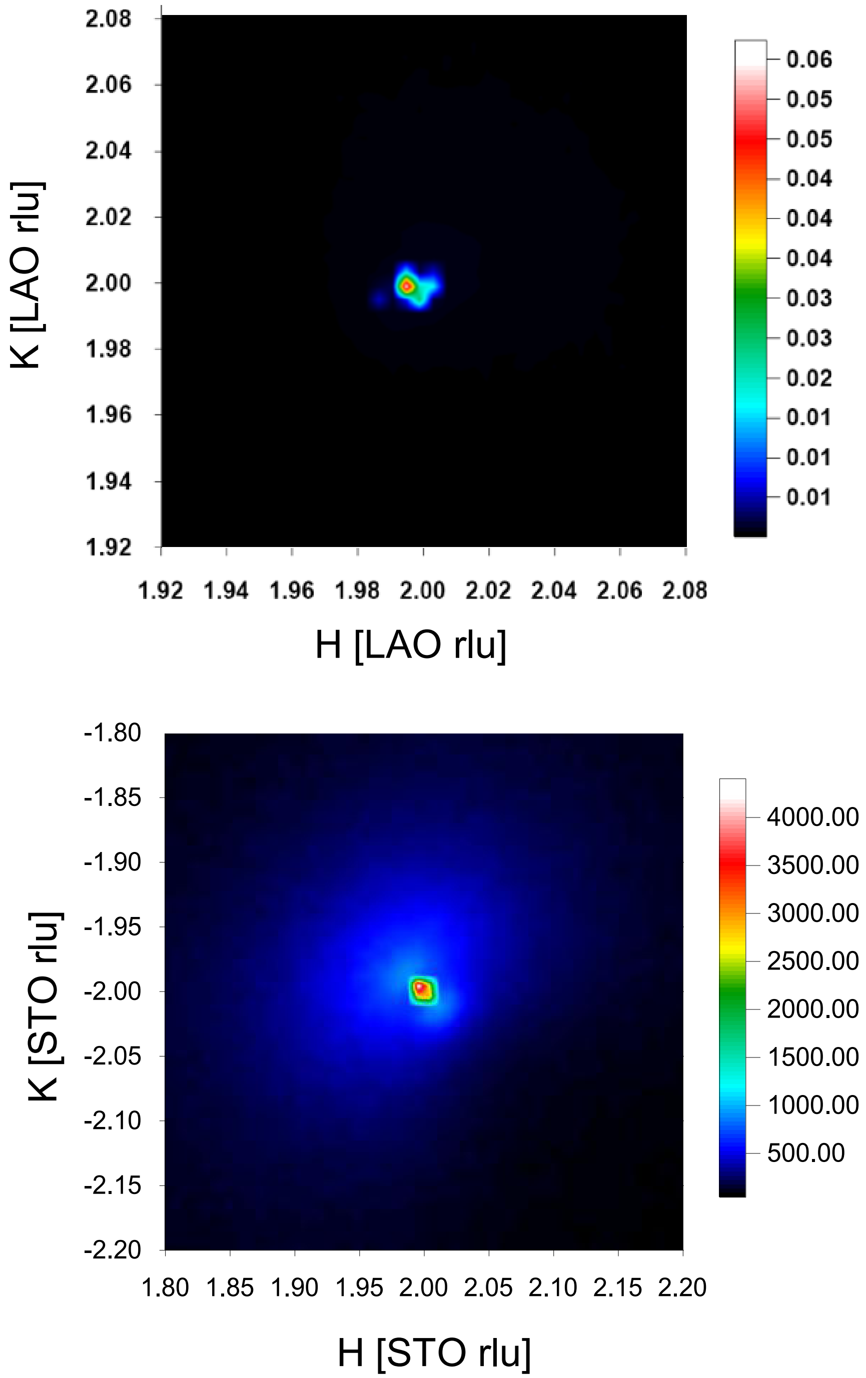

Figure 3.9: Reciprocal lattice maps for 10 uc films of LNO on LAO (top) and on STO (bottom).

Chapter 4

Mott physics near the insulator-to-metal transition in $NdNiO_3$

Abstract

An optical study of $NdNiO_3$ ultrathin films with insulating and metallic ground states reveals new aspects of the insulator-to-metal transition that point to Mott physics as the driving force. In contrast with the behavior of charge-ordered systems, we find that the emergence of the Drude resonance across the transition is linked to a spectral weight transfer over an energy range of the order of the Coulomb repulsion U, as the energy gap is filled with states instead of closing continuously. Additionally, a low temperature increase of the Drude plasma frequency is evident in the metallic state.

4.1 Introduction

The rare earth nickelates have been of interest to researchers in part due to the strong connection between their crystal structure and electronic and magnetic properties [78, 23]. With the exception of $LaNiO_3$ (LNO), the members of the

RNiO$_3$ series (R = rare earth) undergo an insulator-to-metal transition (IMT) at a temperature T_{IMT}, which can be controlled by the radius of R [137], applied hydrostatic pressure [21, 88] or epitaxial strain [134]. It is believed from resonant x-ray diffraction [114], transport [148] and electron diffraction [145] studies that a structural phase transition resulting in charge-ordering is responsible for the IMT. Furthermore, it has been suggested that the ground state of the nickelates can in fact be better understood as a band insulator rather than a Mott-Hubbard system [76]. However, given the recent optical studies of LNO that have shown unusually strong electronic correlations and a spectral weight (SW) transfer consistent with Mott physics [92, 128], it is possible that the current understanding of the IMT in nickelates based solely on charge-ordering is incomplete.

In this letter we present an optical study of newly available ultrathin films of NdNiO$_3$ (NNO) in which the IMT can be quenched by applying compressive strain [71]. In the bulk, NNO undergoes a transition from an antiferromagnetic insulator [39] to a paramagnetic metal at ~ 200 K [137], accompanied by a structural transition [40]. While detailed optical studies of NNO ceramics exist [60], no such characterization of NNO single crystals or epitaxial ultrathin films has been reported. The ability to grow and study high quality samples with tunable properties allows one to thoroughly investigate the processes involved in the IMT. A SW analysis of our data reveals key signatures of Mott-Hubbard physics, providing strong evidence that electronic correlations play a major role in achieving the insulating phase in NNO.

4.2 Methods

Epitaxial NNO films were grown on LaAlO$_3$ (LAO) and SrTiO$_3$ (STO) substrates by pulsed laser deposition with in situ monitoring by reflection high energy electron diffraction. Single crystal LAO (001) and STO (001) substrates provide -0.3% and +2.6% lattice mismatch, respectively. The films are 30 u.c. thick with c-axis parameters of 3.84 Å on LAO and 3.75 Å on STO. Growth conditions and sample characterization details can be found in Ref.[71]. Optical characterization of the films was carried out using variable angle spectroscopic ellipsometry in the range from 60 meV to 6 eV. Additionally, near-normal incidence reflectance from 10 to 80 meV was performed in a Michelson interferometer (Bruker 66vs) relative to a gold mirror and then normalized by the reflectance of the gold coated sample [49].

4.3 Results and discussion

We first consider the real part of the optical conductivity $\sigma_1(\omega)$ given by $\sigma(\omega) = \frac{i\omega[1-\epsilon(\omega)]}{4\pi}$, where $\epsilon(\omega)$ is the complex dielectric function. The room temperature $\sigma_1(\omega)$ for the NNO films on LAO and on STO is shown in Fig.4.1. Below 2 eV the two spectra exhibit the same gross features: a Drude peak and two interband transitions labeled A and B in Fig.4.1. The Drude resonance is stronger for the film on LAO. Based on bulk band structure calculations showing a ${t_{2g}}^6{e_g}^1$ electronic configuration [113, 143], we suggest that features A and B are due to transitions between the occupied and unoccupied antibonding e_g^* orbitals (see inset in Fig.4.1). Above 2 eV, more marked differences between the two spectra are evident. Feature C is broader and centered at higher frequency for the film on LAO and a peak at 4.5 eV (feature D) is only evident for the film on STO. Feature C can be assigned to transitions from the t_{2g}^* and the non-bonding O $2p$ to the e_g^* orbitals. Finally, D and E could be the result of excitations from the bonding t_{2g} and e_g levels to e_g^*. Transitions to the empty Nd $4f$ and $5d$ states could also contribute to the higher energy features D and E, but band structure calculations with density of states (DOS) including these orbitals were not available. We note that these assignments are based on calculations performed for bulk NNO and not for strained films.

The optical conductivity of the NNO film on STO at various temperatures can be seen in Fig.4.2. At low temperature the Drude peak disappears as the system enters the charge-ordered insulating state. The SW of feature A rapidly decreases and a new peak emerges at 0.65 eV (A' in Fig.4.2). This transfer of SW from the Drude resonance to a finite energy peak is typical of charge-ordered

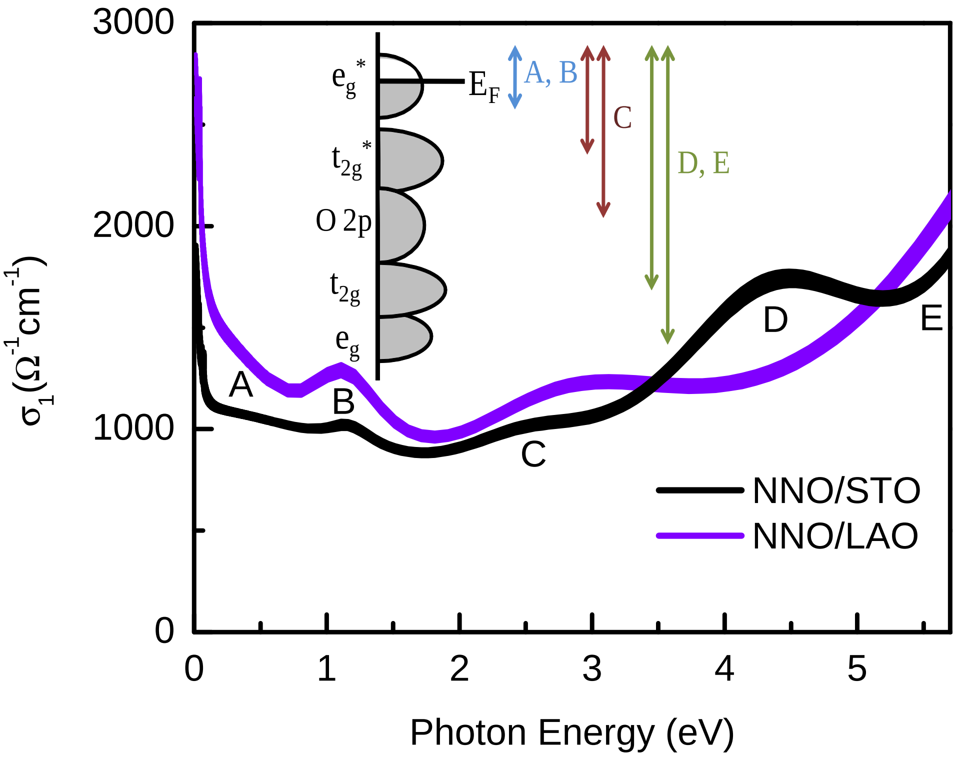

Figure 4.1: Real part of the optical conductivity at 298 K for the NNO films on LAO and STO. The error bars are represented by the thickness of the curves. Inset: sketch of the NNO DOS based on Refs.[113] and [143].

systems in the regime of weak electron-lattice coupling [96, 28]. However, feature A', which is likely due to transitions between the e_g^* states that are gapped in the insulating state, only accounts for part of the lost Drude SW. We must therefore consider feature D, which shows a temperature dependence opposite to that of the Drude response: Its SW decreases as the temperature is raised from 20 K to 200 K and then increases when warmed up further. Thus, this resonance is clearly involved in the SW transfer that leads to the opening of the correlated gap, as evidenced by the SW analysis presented below.

Figure 4.3 shows $\sigma_1(\omega)$ for the NNO film on LAO. In contrast with the film on STO (Fig.4.2) and bulk NNO [60], the Drude resonance remains prominent at 20 K and its magnitude increases. The peak A' that arises at low temperature for the film on STO between features A and B as a result of the IMT is not seen. This is consistent with X-ray absorption data showing a charge-ordered ground state for the film on STO but not for the film on LAO [71]. Finally, we observe an unusual transfer of SW from feature C to the Drude peak, which we discuss in detail below.

To quantitatively study the temperature dependence of the Drude resonance in the metallic phase we consider the plasma frequency ω_p given by

$$\frac{\omega_p^2}{8} = \int_0^{\Omega} \sigma_1(\omega) d\omega = \frac{4\pi n e^2}{m^*}. \tag{4.1}$$

Here n is the density of free carriers, m^* is their renormalized mass, and Ω is the cut-off chosen to include only the coherent contribution to $\sigma_1(\omega)$. In conventional metals the free carrier SW is unaltered with temperature and the entire temperature dependence of the Drude absorption is due to a decrease in the scattering rate $1/\tau$. Correlated metals, on the other hand, often exhibit an exotic temperature dependence of ω_p [16]. In the normal state of high-T_c cuprates, for instance, a $\sim 2\%$ enhancement in ω_p has been measured that can not be explained by the Sommerfeld model [91]. More recently, a low temperature increase in the Drude SW of unprecedented magnitude was observed in LaNiO$_3$ (LNO) [128].

For the film on LAO ω_p was obtained using $\Omega = 125$ meV, before the onset of feature A. Additionally, $1/\tau$ was obtained from the extended Drude analysis

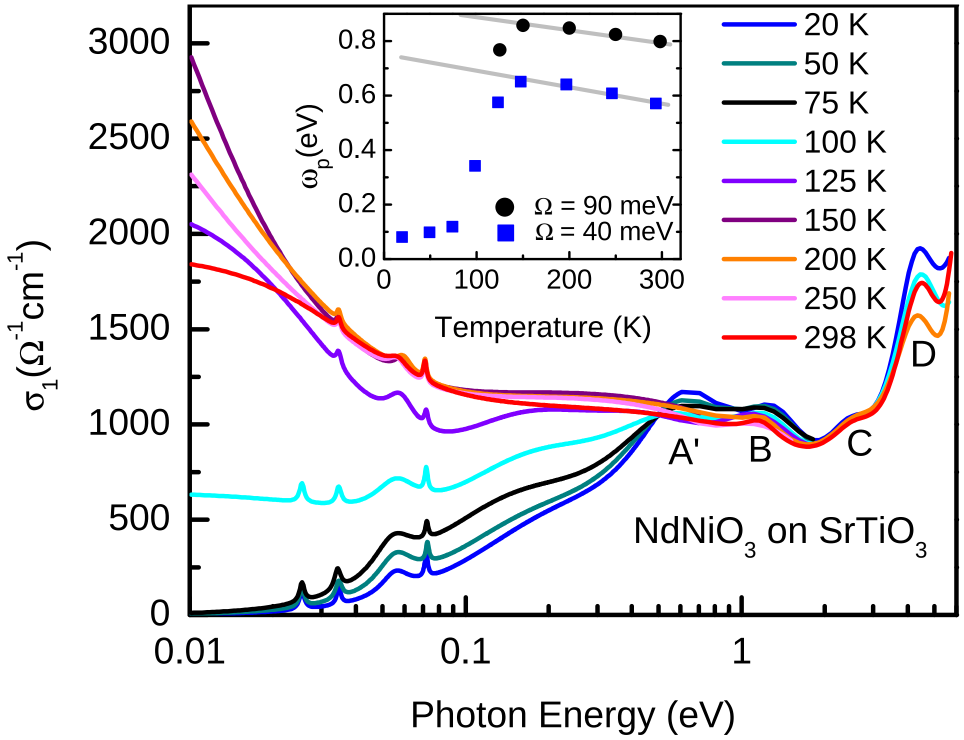

Figure 4.2: Real part of the complex conductivity for the NNO film on STO across the IMT. Inset: ω_p obtained from Eq.(4.1) with $\Omega = 90$ meV and plasma frequency obtained with $\Omega = 40$ meV. The gray lines are guides to the eye.

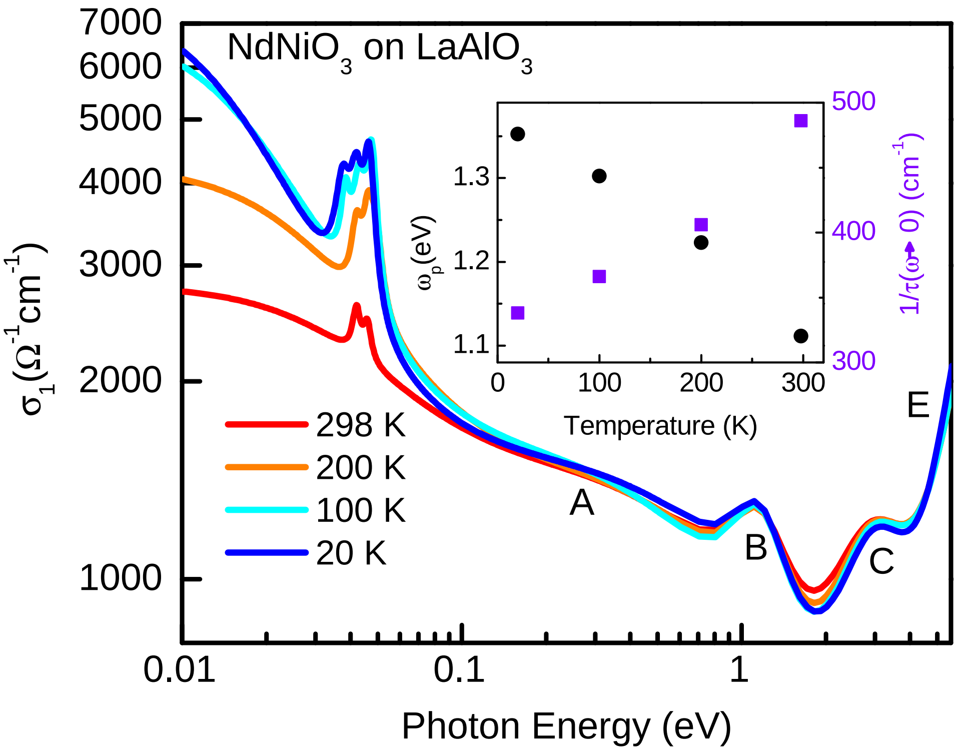

Figure 4.3: Real part of the optical conductivity for the NNO film on LAO at various temperatures. The Drude resonance remains prominent at all temperatures and no IMT is observed. Inset: ω_p and $1/\tau$ obtained from Eqs.(4.1) and (4.2).

using

$$\frac{1}{\tau(\omega)} = -\frac{\omega_p^2}{\omega} Im\left(\frac{1}{\tilde{\varepsilon}(\omega) - \varepsilon_\infty}\right). \tag{4.2}$$

ω_p and $1/\tau(\omega \to 0)$ are plotted in the inset in Fig.4.3. Similar to the bahavior of LNO [128], $1/\tau$ decreases at low temperature, but not enough to account for the change in DC resistivity [71]. The enhancement in ω_p from 1.1 eV a 298 K to 1.35 eV at 20 K must also be taken into account, signaling that additional states are being populated at the Fermi energy. For the film on STO we used $\Omega = 90$ meV, the minimum in $\sigma_1(\omega)$ at 125 K between the Drude peak and the first interband transition A. A similar behavior to that of the film on LAO is observed at $T > T_{IMT}$. We find that ω_p increases with decreasing temperature down to 150 K (see inset in Fig.4.2). The inset in Fig.4.2 also shows ω_p integrated up to 40 meV, roughly the size of the insulating gap. As expected, the low frequency SW is close zero at low temperature and then increases rapidly as T_{IMT} is approached.

While both samples exhibit a low temperature enhancement of ω_p in the metallic phase, the origin of this effect is not the same. To understand this better we consider the ratio of $\sigma_1(\omega)$ at low temperature and at 298 K shown in the insets in Fig.4.4. For the film on LAO there is a low temperature decrease in $\sigma_1(\omega)$ between 1.5 eV and 4 eV and a transfer of SW from feature C to the Drude resonance. This can also be seen by studying SW(Ω), which represents the effective number of carriers contributing to absorption below the cut-off frequency Ω and is given by

$$SW(\Omega) = \int_0^\Omega \sigma_1(\omega) d\omega. \tag{4.3}$$

Figure 4.4(a) shows the ratio of the SW at various temperatures and that at 298 K for the film on LAO. For $\Omega = 1.2$ eV, which includes the contributions from interband transitions A and B, the SW is 10 % higher at 20 K than at 298 K. SW($\Omega = 4$ eV), on the other hand, is the same at all temperatures, confirming the transfer of SW from feature C to the Drude resonance.

For the film on STO, $\sigma_1(\omega)$ is enhanced above 3.5 eV at 200 K and then suppressed in the insulating state. SW($\Omega = 2$ eV), which includes features A and B, increases down to 150 K and then decreases in the insulating state (Fig.4.4(b)). With $\Omega = 5.6$ eV we find that the SW is nearly the same at all the measured

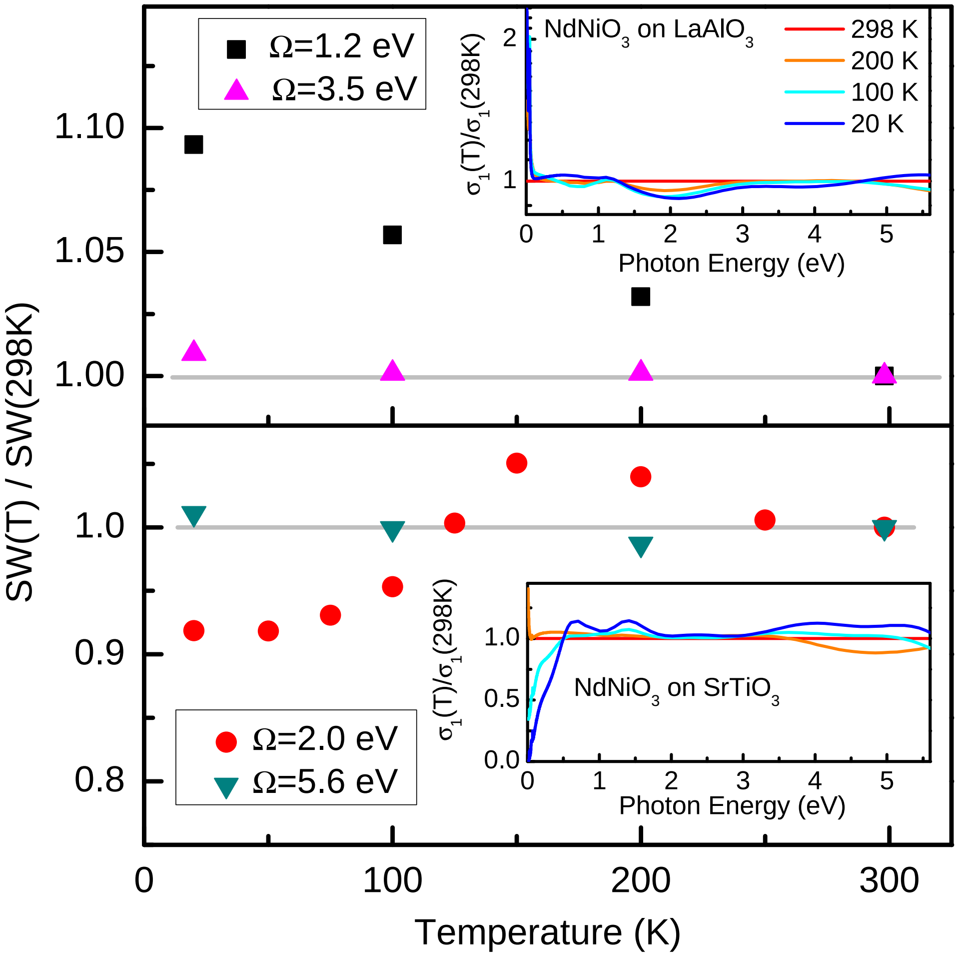

Figure 4.4: Ratio of the SW (Eq.(4.3)) at low temperature and at 298 K obtained with various frequency cut-offs Ω for the films on LAO (a) and on STO (b). The gray lines are guides to the eye. Insets: Ratio of $\sigma_1(\omega)$ at low temperature and at 298 K.

temperatures. This behavior is drastically different from systems where the IMT is caused by charge- and/or spin- ordering. These latter effects lead to the opening of an energy gap with a transfer of the free carrier SW to resonances immediately above it [28]. In Fe_3O_4, for example, the redistribution of SW is restricted to 10 times the size of the energy gap Δ [96], instead of up to 30Δ as we observe for NNO. Our data are also in contrast with spin density wave systems, such as $Cd_2Os_2O_7$ [93], in which the gap closes continuously. Instead, like in other Mott systems [101], Fig.4.2 shows that $\sigma_1(\omega)$ increases gradually in the gap region as it is filled with states. Contray to the conventional understanding, these two observations indicate that charge-ordering, if present, is not the driving force for the IMT in NNO.

Our data suggest that the different ground states observed for the two films are linked to the contrast seen in the high energy $\sigma_1(\omega)$, namely features C and D (Fig.4.1). While we have tentatively attributed these peaks to different interband transitions (Fig.4.1 inset), ab initio calculations taking into account the modified crystal structure of the strained films are necessary to be sure of this assignment. Irrespective of this uncertainty, our observations are consistent with the Mott-Hubbard picture for a strongly correlated metal and a Mott insulator. When a conducting state is initiated in a Mott-Hubbard system either by temperature or doping, the coherent contribution to $\sigma_1(\omega)$ increases at low temperature as SW is transferred from the Hubbard band to the quasiparticle peak. This phenomenon occurs on the energy scale of $U/2$, where U is the on-site Coulomb repulsion. In the insulating state, on the other hand, the transitions related to the Hubbard bands will occur at energies on the order of U since there is no quasiparticle peak [110]. Similarly, our data show that the energy scale involved in the SW transfer for the NNO film on STO ($\sim$ 5.6 eV) is roughly twice as large as the one for the film on LAO ($\sim$ 3 eV) and suggest a range of U that is in reasonable agreement with $U = 7$ eV reported previously [20]. We therefore propose that Mott physics plays an important role in the IMT of NNO, in contrast with the claims of Ref. [76] that the insulating state in the nickelates can be better described by a more conventional band picture.

While the optical data obtained for the film on LAO are very different from the film on STO and even bulk NNO, the spectra are surprisingly similar to those of LNO [128]. Not only does the sample remain metallic at all temperatures but the transfer of SW from feature C to the Drude resonance over the energy range of $U/2$ and the dramatic increase in ω_p are almost identical to the temperature dependence of LNO. The interband transitions in Fig.4.3 are remarkably similar to those observed in ultrathin films of LNO on LAO as well.

Even though applying hydrostatic pressure can cause a suppression of T_{IMT} due to an increase in the bandwidth, over 40 kbar would be required to fully quench the IMT [147], much more than can be achieved with the -0.3% of epitaxial strain present in our films. We therefore propose that the stabilization of the metallic phase in the NNO film on LAO can not be understood in terms of a change in bandwidth and the effects of heteroepitaxial strain must be considered. Previous work on ultrathin films of LNO has shown that tensile and compressive strain result in different crystal structures for the films [74, 24]. Compressive strain is accommodated by Ni-O bond bending and stretching, resulting in a distortion of the NiO_6 octahedra and a reduced symmetry of the atomic structure relative to bulk LNO. In contrast, samples under tensile strain show a pronounced pattern of octahedral rotations with an additional “breathing” mode of the NiO_6 network. This latter effect induces a Ni-O bond length disproportionation resulting in two inequivalent Ni sites [24].

This link between bi-axial strain and NiO_6 structure could be responsible for the quenching of the IMT. Assuming a similar effect to that observed in LNO, the “breathing” distortion associated with deterrences in orbital polarization and ligand hole density distribution would be active for the film on STO but not for the film on LAO, thus precluding the charge-ordered ground state in the latter and stabilizing the unusual metallic phase. Orbital reflectometry experiments that can detect small variations in the orbital occupation [15] would therefore be helpful in understanding the striking strain dependence we observed in the optical properties of NNO.

4.4 Conclusions

The discussion in the previous paragraph and the SW analysis presented above suggest that charge-ordering and Mott physics work together to produce the insulating state in NNO. We observe a transfer of SW from the Drude resonance to the peaks immediately above the insulating gap, typical of charge-ordering systems. However, we also find unambiguous evidence that the energy scales of the order of U are intimately involved in both the IMT and the charge dynamics of the metallic state. The simple band picture based solely on charge-ordering [76] fails to account for the salient spectral properties of nickelates presented in this letter and in Ref. [128] and Mott physics must therefore be taken into account to fully describe this correlated system.

Acknowledgments

Work at UCSD is supported by DOE-BES. J.C. was supported by DOD-ARO under the grant No. 0402-17291 and NSF grant No. DMR-0747808.

Chapter 5, in full, is a reprint of the material as it appears in Phys. Rev. Lett. **107**, (2011). M. K. Stewart, J. Liu, M. Kareev, J. Chakhalian, and D. N. Basov. The dissertation author was the primary investigator and author of this paper.

Appendix: Ellipsometric measurements and data analysis

The ellipsometric studies were carried out in two J. A. Woollam ellipsometers: an IR-VASE model based on a Bruker 66vs Michelson interferometer and covering the range from 60 to 600 meV and a monochromator based VASE model for the range between 0.6 and 6 eV. Both instruments are equipped with home-built UHV cryogenic chambers to allow measurements down to 20 K. For the IR-VASE system, test spectra were obtained from a 20 nm thick thermal oxide on Si with and without the ZnSe windows in place, which were within 0.5% of each other. Thus, no corrections to the data are required, as is often the case in this frequency range given that the retardance is inversely proportional to the wavelength. In the case of the VASE ellipsometer, the effects of the quartz windows are accounted for by performing a calibration with the same thermal oxide described above over entire frequency range.

A spot size of about 3 mm in diameter was used and the size of our samples is 5 mm x 5 mm. The samples were mounted on brass cones to avoid measuring reflections from the sample holder. The measurements were performed at incidence angles of 60° and 75° with the size of the elongated spot being 6 mm and 11.6 mm, respectively, and an uncertainty in the angle of less than 0.1°. At each angle we measured the polarization state of the light in terms of two parameters, Ψ and Δ, which are related to the Fresnel reflection coefficients for p- and s- polarized light ($\tilde{R}_{pp}$ and $\tilde{R}_{ss}$) through the equation

$$\tilde{\rho} = \frac{\tilde{R}_{pp}}{\tilde{R}_{ss}} = tan(\Psi)e^{i\Delta}. \tag{4.4}$$

In order to extract the optical constants of the NNO thin films, we first need to know the optical properties of the substrate. For this reason, we have measured the bare LAO and STO substrates over the entire frequency range at all the same temperatures as the films. The back of the substrates has been roughened using diamond sandpaper to avoid reflections from the backside in the transparent region.

The VASE system is equipped with a computer-controlled wave plate compensator which allows for accurate measurements of the Mueller-Matrix and of the depolarization of the light beam by the sample. Fig.4.5(a) shows that the depolarization caused by the NNO/STO sample is less than 0.3%, much lower than the $\sim$ 1% cutoff usually associated with isotropic, homogeneous samples [38]. This confirms that the thickness of the films is uniform throughout the sample [115], as expected from the RHEED controlled layer-by-layer deposition technique used to grow the films. The use of the Mueller-Stokes formalism is therefore not required

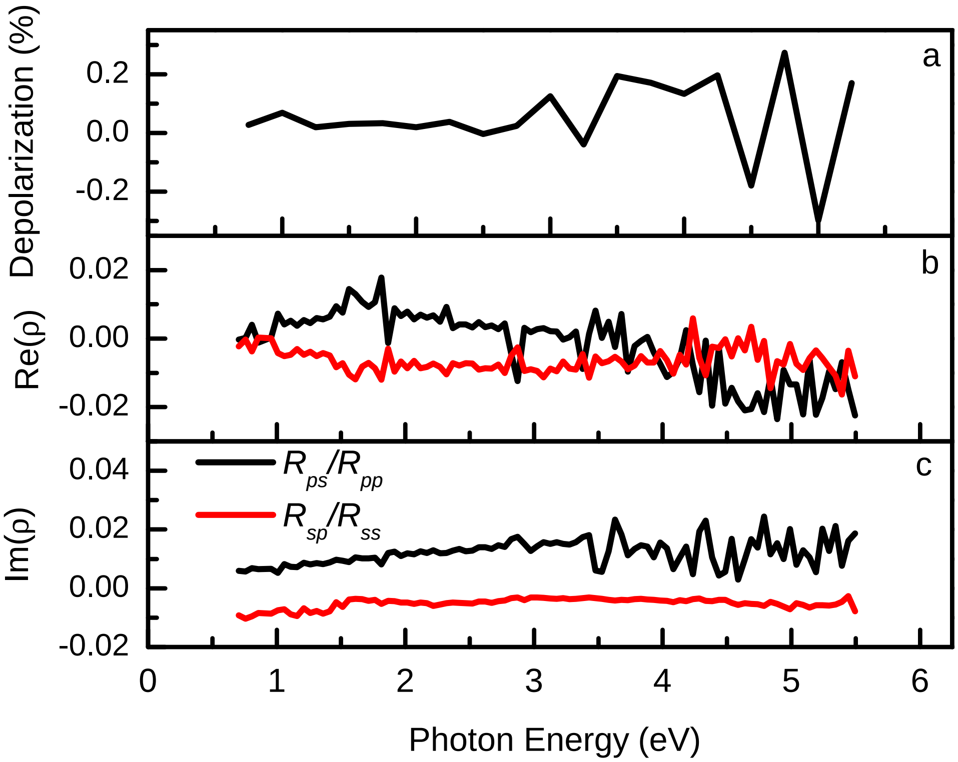

Figure 4.5: Representative depolarization data for the NNO film on STO obtained at room temperature (a). Real (b) and imaginary (c) parts of the ratios $\tilde{R}_{ps}/\tilde{R}_{pp}$ and $\tilde{R}_{sp}/\tilde{R}_{ss}$ for the NNO film on STO.

for the analysis of our data and we focus only on the Jones matrix

$$J = \begin{bmatrix} \tilde{R}_{pp} & \tilde{R}_{sp} \\ \tilde{R}_{sp} & \tilde{R}_{ss} \end{bmatrix}, \tag{4.5}$$

which is a diagonal matrix in the case of isotropic samples. The ratio of the off-diagonal and diagonal matrix elements obtained for the NNO/STO sample at room temperature are shown in Fig.4.5 (b) and (c). The magnitudes of both the real and imaginary parts of these ratios are all less than 0.02, i.e. the off-diagonal components of the Jones matrix are less than 2% of the diagonal components. We can therefore be certain that the anisotropy in the optical constants of out films is negligible and an isotropic model can be employed in the data analysis.

The analysis of the experimental data was performed using the WVASE 32 software from J. A. Woollam, which employs the Levenberg-Marquardt multivariate regression algorithm to find the best fit to the data by minimizing the mean-squared error [55]. The error bars in the resulting optical constants are based on the 90% confidence limits obtained from the fits. Our models include various oscillators to account for all the far-IR phonons typical of transition metal oxides as well as the interband transitions and the Drude response, when appropriate. As is now standard procedure for the starting point in the analysis of ellipsometric data, we aim to fully parametrize the dielectric function of the material with the set of oscillators as a whole and no information is extracted from the individual functions [68]. The sole precondition for this approach is that the oscillators be Kramers-Kronig consistent in order to obtain physically sound optical constants, which is met by all our models.

We first modeled the data obtained for the bare LAO and STO substrates at each temperature. The raw ellipsometric data and the model fit for the STO substrate at room temperature are plotted in Fig.4.6 (a), showing good agreement between the two. We employed a surface roughness layer consisting of 50% void and 50% LAO or STO, respectively, and described its response with the Bruggeman effective-medium approximation. The thickness of these layers was determined from the mid-IR part of the spectra in which the substrates are transparent and was found to be ~ 3 nm. The optical constants we obtained are in good agreement

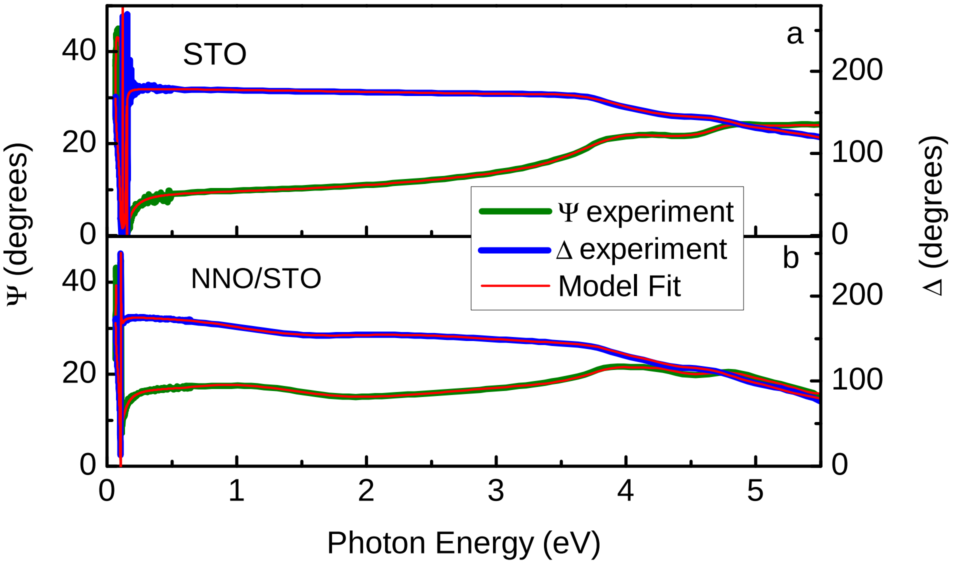

Figure 4.6: Representative raw ellipsometric data and model fit for the STO substrate (a) and the NNO/STO sample (b) at room temperature.

with those reported in the literature [122, 22, 146].

Knowing the optical constants of the LAO and STO substrates at all the relevant temperatures, it was then possible to extract the optical spectra of the NNO thin films themselves. For this purpose, we have employed a two layer model containing the substrate and the thin film. In this case, the optical constants of the substrates were fixed, while those of the NNO films were parametrized using various Kramers-Kronig consistent oscillators which we fit to the experimental data using the WVASE32 software described above. The algorithm used accounts for reflections from the sample surface as well as from the NNO/substrate interface. Representative raw data for the NNO/STO sample are shown in Fig.4.6 (b) along with the model fit.

Chapter 5

Insulator-to-metal transition and correlated metallic state of V_2O_3 investigated by optical spectroscopy

5.1 Introduction

Many correlated electron systems exhibit phase transitions that can be driven by a variety of external factors and have repercussions that often extend beyond the immediate vicinity of the transition.[52, 7] V_2O_3, commonly considered the canonical Mott-Hubbard system, presents a temperature induced inuslator-to-metal transition (IMT) at $T_c \approx 150$ K. This transition from an antiferromagnetic insulating (AFI) phase to a paramagnetic metal (PM) is accompanied by a change in the crystal symmetry from monoclinic to rhombohedral.[32] The optical properties of V_2O_3 across this IMT and in the correlated metallic state were initially described with the single band Hubbard model within the framework of DMFT [110, 109]. While this work represented a breakthrough in the understanding of the Mott driven IMT, later studies have shown that the multi-band character of V_2O_3 must be taken into account.[95, 46] The exact configuration of the t_{2g} manifold near the Fermi level, however, is still subject to controversy.[80, 94, 34, 130, 84]

In addition to the aforementioned IMT, a high temperature paramagnetic insulating (PI) phase can be attained in V_2O_3 by applying external pressure and by chemical doping.[77, 54, 70] In stoichiometric V_2O_3, a *crossover* region between the PM and PI phases exists at elevated temperatures.[97] Recent x-ray absorption experiments show variations in the orbital occupation of the metallic state reached through different paths across the phase diagram.[108] These results point to the interplay between electronic correlations and the crystal field as a key factor governing the IMT.

In this work we present an optical study of V_2O_3 thin films showing a significant enhancement of the Drude resonance relative to previous samples.[104] The broad energy range and detailed temperature dependence of our data, in addition to the strong Drude response, allow us to thoroughly investigate the optical properties both across the AFI to PM transition and above T_c. We report on canonical optical signatures of Mott transitions observed in our data, including evidence of a pseudogap near the IMT. Our results unveil a number of similarities between the properties of the PM state of V_2O_3 and the metallic puddles found in phase separated VO_2.

5.2 Methods

V_2O_3 thin films were grown by RF magnetron sputtering of a V_2O_3 target (1.5" diameter, $> 99.7\%$, ACI Alloys, Inc.) on an r-plane $(10\bar{1}2)$ sapphire substrate. The sample was prepared in a high vacuum deposition system with a base pressure of $1 \cdot 10^{-7}$ Torr. 4 mTorr ultra high purity (UHP) Ar was used for sputtering. The substrate temperature during deposition was 750°C while the RF magnetron power was kept at 100 W. These conditions yielded a deposition rate of 0.67 Å/s and a total thickness of 100 nm for the sample reported here. The sample was cooled at a rate of 13°C/min in the same Ar flow after the deposition. Macroscopic resistance vs temperature $(R - T)$ measurements show a metal-insulator transition at 150K with more than 5 orders of magnitude change in resistance. Finally, half of the sample was annealed for 30 minutes at each 550°C and 650°C with a base pressure of $1 \cdot 10^{-5}$ Torr. Most of this paper will focus on the data obtained for the pristine sample. Results for the annealed film are shown in Section 5.3.5.

Optical characterization of the V_2O_3 film and the sapphire substrate was carried out using spectroscopic ellipsometry in the range from 70 meV to 6 eV and near normal incidence reflectance in the range from 6 to 85 meV. Ellipsometric measurements were performed in two commercial Woollam ellipsometers equipped with home built UHV cryogenic chambers to allow for low temperature studies. The optical conductivity of the film was obtained from the raw reflectance and ellipsometry data using a two layer model taking into account the reflections from the film/substrate interface and the temperature dependence of the substrate. A detailed description of experimental and analysis methods can be found in Refs.[128] and [126].

5.3 Results and discussion

5.3.1 Optical conductivity: general trends

We begin by considering the real, dissipative part of the optical conductivity $\sigma_1(\omega)$, which is related to the complex dielectric function through the equation $\sigma(\omega) = \frac{i\omega[1-\epsilon(\omega)]}{4\pi}$. The low temperature spectra in Fig.5.1 show the sample in the insulating state, where $\sigma_1(\omega)$ exhibits an energy gap of ~ 0.5 eV and a number of interband transitions above 1 eV. As the temperature increases the gap is gradually filled with states and a Drude resonance emerges above 180 K along with a finite energy peak centered at 0.27 eV. Additionally, the spectral weight associated with the interband transitions above 1 eV is reduced relative to the insulating state. In comparison to earlier optical data for V_2O_3 thin films,[104] two important differences are evident: i) The optical conductivity due to interband transitions (above 1 eV) is higher in the insulating state than in the metallic state. This is in contrast with the data in Ref.[104] where the low and high temperature $\sigma_1(\omega)$ curves cross at 3 eV. ii) The Drude peak is much stronger than the weak resonance observed previously and is in fact of similar magnitude to that observed in single crystal

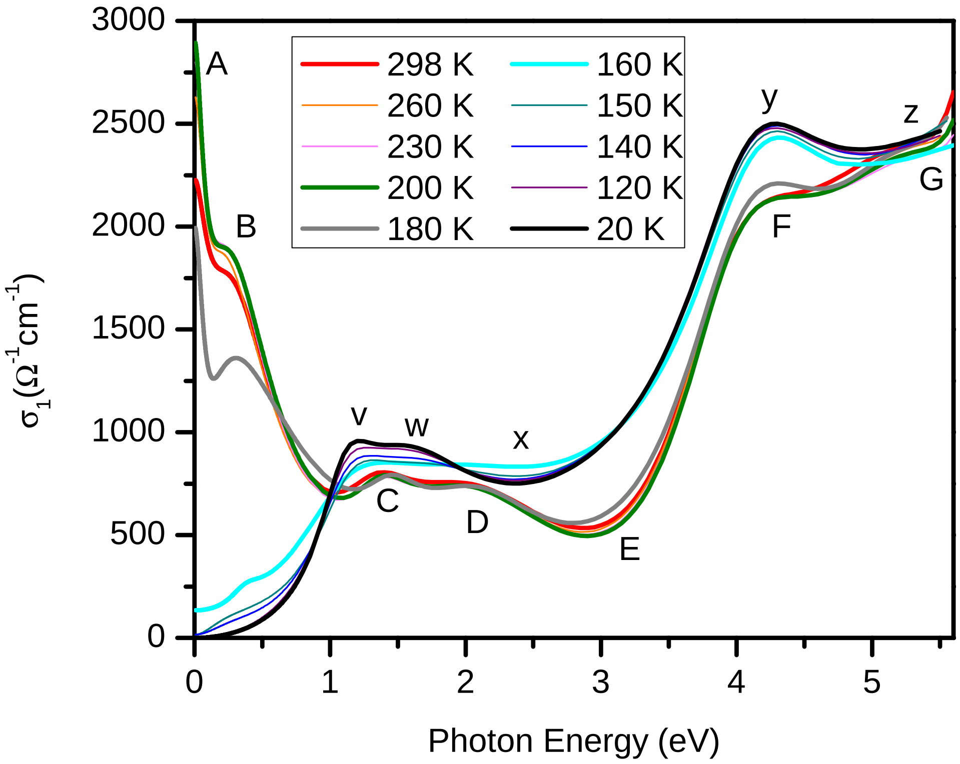

Figure 5.1: Real part of the optical conductivity of pristine V_2O_3 across the insulator-to-metal transition. Interband transitions in the insulating state are labelled $v - z$. $A - G$ correspond to features in the metallic phase. See text and Fig.5.2 for details.

samples of V_2O_3.[6] In contrast with Ref.[6], in this work we focus our attention on the antiferromagnetic insulator to paramagnetic metal transition and we examine a much wider energy range of the optical conductivity, up to 6 eV. Below we discuss the spectra in Fig.5.1 in relation to theoretical results and earlier measurements on V_2O_3 and VO_2.

We focus first on the optical conductivity at 20 K, corresponding to the insulating state. The right panel in Fig.5.2 shows a sketch of the density of states for the antiferromagnetic insulating state based on the LDA+U calculations shown in Ref.[37]. The vanadium t_{2g} orbitals are occupied by two electrons and split into non-degenerate a_{1g} (green) and doubly degenerate e_g^π (blue) bands due to the trigonal field. Additionally, the strong on-site Coulomb repulsion ($U = 2.8$ eV in Ref.[37]) separates the spin up and spin down t_{2g} levels into upper and lower

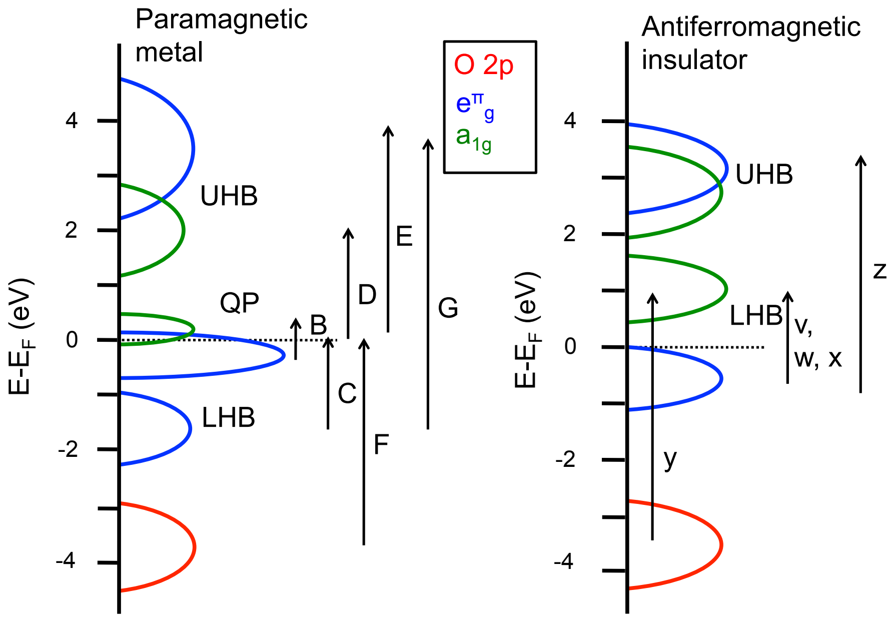

Figure 5.2: Sketch of the electronic density of states for the paramagnetic metal [99] (left) and the antiferromagnetic insulator [37] phases of V_2O_3. The assignment of interband transitions corresponds to the labeling of the optical conductivity features shown in Fig.5.1.

Hubbard bands (UHB and LHB, respectively). The oxygen $2p$ bands are located about 4 eV below the Fermi level and lower.[104] Based on this picture, we assign features v through z to interband transitions, as depicted in Fig.5.2 (b). Peaks v, w, and x are due to transitions within the lower Hubbard bands of the t_{2g} manifold. Features y and z are due to excitations from the O $2p$ bands to the LHB and from the LHB to the UHB, respectively. We note that the work in Ref.[37] results in a ground state in which the a_{1g} LHB is not occupied. This is in contrast with x-ray absorption studies revealing an AFI ground state with an $(e^{\pi}_{g}e^{\pi}_{g})$:$(e^{\pi}_{g}a_{1g})$ occupation ratio of 2:1.[95] For this reason, transitions within the LHB result in a series of peaks between 1 and 3 eV rather than the single structure one might expect from the simplified picture in Fig.5.2.

In considering the spectra for the metallic state between 200 and 298 K, we refer the LDA+DMFT predictions from Ref.[99]. In addition to the LHB and UHB present at low temperature, two quasiparticle peaks (QP) emerge at the Fermi level (see left panel in Fig.5.2). The a_{1g} orbitals are nearly empty and have coherent character at the Fermi level, giving rise to the narrow Drude resonance (A in Fig.5.1). Some e_g^π contribution to the Drude peak is also possible, as these bands are expected to approach the regime of coherent quasiparticles below 390 K.[99] Feature B can be assigned to transitions from the e_g^π QP to the a_{1g} QP. C and D are due to transitions from the e_g^π LHB to the QP and from the QP to the a_{1g} Hubbard band respectively. Features F and G correspond to transitions within the e_g^π bands, from the QP to the UHB and between the lower and upper Hubbard bands. Finally, peak E is related to transitions form the oxygen $2p$ bands. These assignments are, in general, consistent with those in previous optical studies.[104, 6] However, here we compare our data to DMFT results taking into account the strongly correlated nature of the metallic phase, i.e. the presence of the Hubbard bands and quasiparticle peaks. The high quality of our films and the detailed temperature dependence of our data allow for more specific assignments and in depth analysis. In the following section we examine features $A-G$ in the context of the the Mott-Hubbard model.

5.3.2 Metallic state of V_2O_3

To better understand the properties of the metallic state of V_2O_3 we study the temperature dependence between 200 K and 298K. It is useful to consider two quantities: the Drude plasma frequency ω_p and the effective spectral weight as a function of frequency SW(ω), given by

$$\frac{\omega_p^2}{8} = \int_0^\Omega \sigma_1(\omega)d\omega = \frac{4\pi ne^2}{m^*}, \tag{5.1}$$

$$SW(\omega) = \int_0^\omega \sigma_1(\omega')d\omega'. \tag{5.2}$$

The former is related to the free carrier density n and effective mass m^* while the latter represents the effective number of carriers contributing to absorption below the frequency ω. In the case of ω_p, the integration cutoff is chosen such that only the Drude contribution to the optical conductivity is included, leaving out the spectral weight due to interband transitions. The inset in Fig.5.3 (a) shows ω_p obtained using $\Omega = 140$meV, before the onset of feature A. An increase from 1.14 eV at 298 K to 1.25 eV at 200 K is evident, signifying and enhancement in the free carrier density (the temperature dependence of m^* is discussed at the end of this section). Furthermore, in Fig.5.3 (a) the ratio of SW(ω) at 200 K and 298 K shows that, within the metallic state, the low temperature SW(ω) remains higher up to 3.5 eV. This means that interband transitions up to 3.5 eV must be taken into account in order to explain the low temperature increase in the Drude SW, as is often the case in correlated metals.[128, 126] Looking at the difference between the $\sigma_1(\omega)$ spectra at 200 K and 298 K (Fig.5.3 (b)), it is evident that a transfer of SW from features C, D, and E to features A and B is taking place.

The study of the temperature dependence described above confirms the assignments of features $A - G$ (Fig.5.2) in the context of the DMFT predictions for Mott-Hubbard systems. [109, 99] At low temperatures, a transfer of SW from the Hubbard bands to the quasiparticle peak is expected. This is evidenced in our data by the increase in SW of the features associated with the QP (A and B) at the expense of those related to the Hubbard bands ($C - E$). The optical conductivity of feature G is also reduced at 200 K, consistent with the assignment of this peak to transitions between the LHB and the UHB.

We note that the ω_p values reported in the inset of Fig.5.3 are low compared to the band theory prediction, giving a ratio $K_{exp}/K_{band} = 0.12$ at 200 K. Here K_{exp} and K_{band} represent the electronic kinetic energy obtained from experiment and from band theory, respectively, and their ratio is used to quantify the strength of electronic correlations.[103] K_{exp} is extracted from the optical conductivity using

$$K_{exp} = \frac{\hbar a}{e^2} \int_0^{\Omega} \frac{2\hbar}{\pi} \sigma_1(\omega) d\omega, \tag{5.3}$$

where $a = 3$ Å is the lattice constant and Ω is the same as in Eq.5.1. While this value represents a 100% increase from the previous generation of V_2O_3 films, it is still very much in the strongly correlated regime lying between the nickelates ($K_{exp}/K_{LDA} \approx 0.04 - 0.1$) [128, 127, 126] and the cuprates ($K_{exp}/K_{LDA} \approx 0.15 - 0.45$).[103, 8]

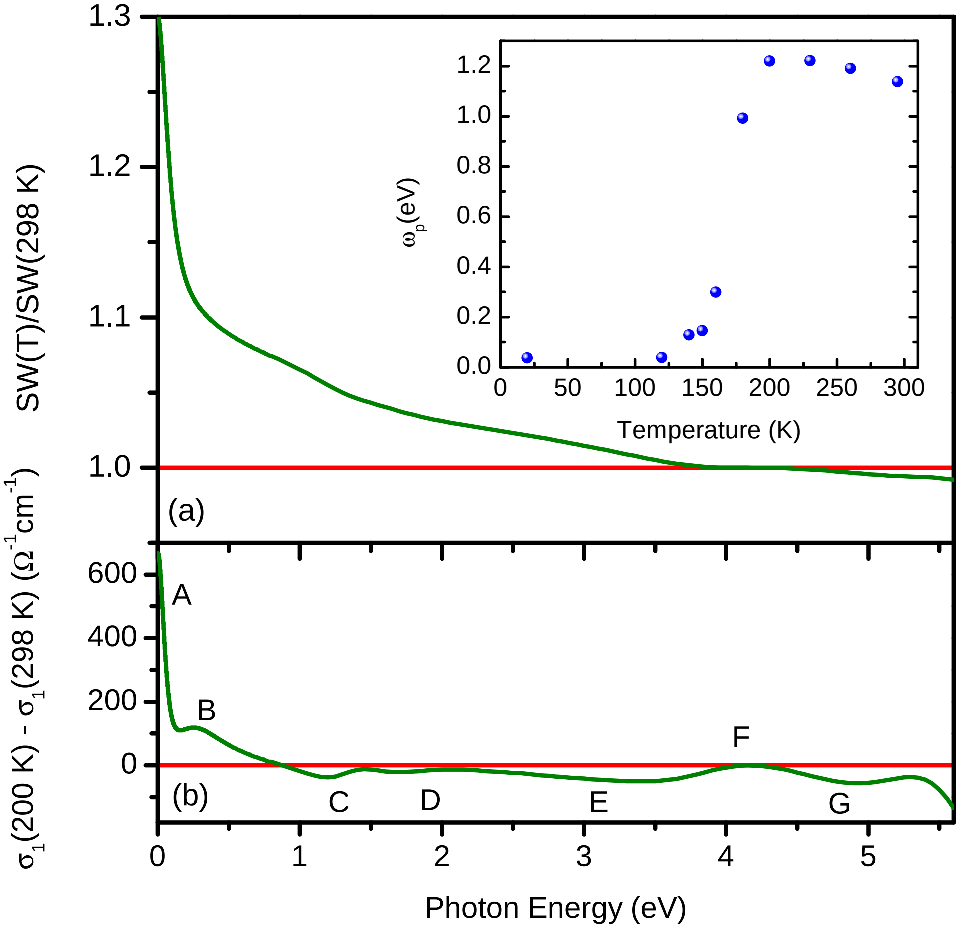

Figure 5.3: Ratio of the spectral weight at 200K and at 298 K (a). Inset: Drude plasma frequency obtained from Eq.5.1 with the integration cutoff 140 meV. Difference between the optical conductivity spectra at 200 K and at 298 K (b). Intra- and interband transitions are labeled as in Fig.5.1

In addition to the spectral weight, important information about the metallic behavior of V_2O_3 can be obtained from the extended Drude analysis. This theory is often used in the study of correlated metals as it allows for the frequency dependence of the carrier scattering rate

$$\frac{1}{\tau(\omega)} = \frac{\omega_p^2}{4\pi} \frac{\sigma_1(\omega)}{\sigma_1^2(\omega) + \sigma_2^2(\omega)}, \tag{5.4}$$

which can not be assumed to be a constant as in the case of conventional metals. Additionally, the effective mass of the carriers m^*, which in the presence of correlations often shows a strong frequency dependence and an enhancement relative to the band mass m_b, can be obtained from

$$\frac{m^*(\omega)}{m_b} = \frac{\omega_p^2}{4\pi\omega} \frac{\sigma_2(\omega)}{\sigma_1^2(\omega) + \sigma_2^2(\omega)}. \tag{5.5}$$

The inset in Fig.5.4(b) shows $1/\tau(\omega)$ at various temperatures plotted with the gray line representing $1/\tau(\omega) = \omega$. It is evident that $1/\tau(\omega) > \omega$ up to 0.4 eV, in violation of the canonical criterion for well-defined quasiparticles: $1/\tau(\omega) << \omega$. Thus, the charge carriers in V_2O_3 are not well-defined quasiparticles and can not be described by Fermi Liquid theory. Another important aspect of the $1/\tau(\omega)$ spectra is the maximum appearing at 200 K centered around 0.18 eV. This type of structure in the scattering rate has been observed in other correlated oxides such as the high-T_c cuprates, nickelates, and VO_2,[101] oftentimes in the vicinity of an IMT. It can be attributed to the presence of a pseudogap: a partial gapping of the Fermi surface leading to a suppression in the scattering rate at low frequencies. The mass enhancement factor (Fig.5.4(c)) exhibits a strong frequency dependence, particularly at low temperatures. Additionally, in the low frequency limit m^*/m_b increases as the temperature is lowered towards the insulting phase, as expected in the presence of strong correlations.

5.3.3 Insulator-to-metal transition

As discussed above, the optical conductivity in Fig.5.1 clearly shows the insulator-to-metal transition in V_2O_3 occuring around 180 K. In this section we examine the aspects of this transition in more detail, particularly as they relate

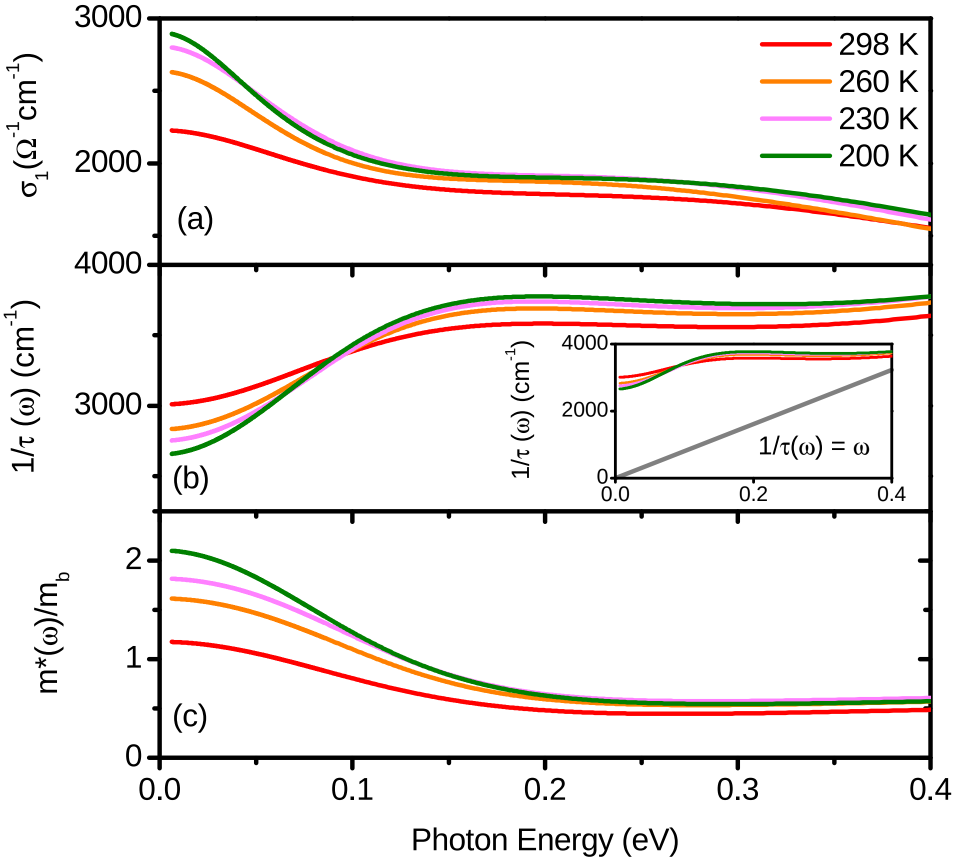

Figure 5.4: Extended Drude analysis of the metallic state of V_2O_3. Real part of the optical conductivity (a), frequency dependent scattering rate given by Eq.5.4 (b) and frequency dependent mass enhancement factor obtained from Eq.5.5 (c). The inset in panel (b) shows $1/\tau(\omega)$ plotted with the $y-$axis scale starting at 0 and the gray line represents $1/\tau(\omega) = \omega$.

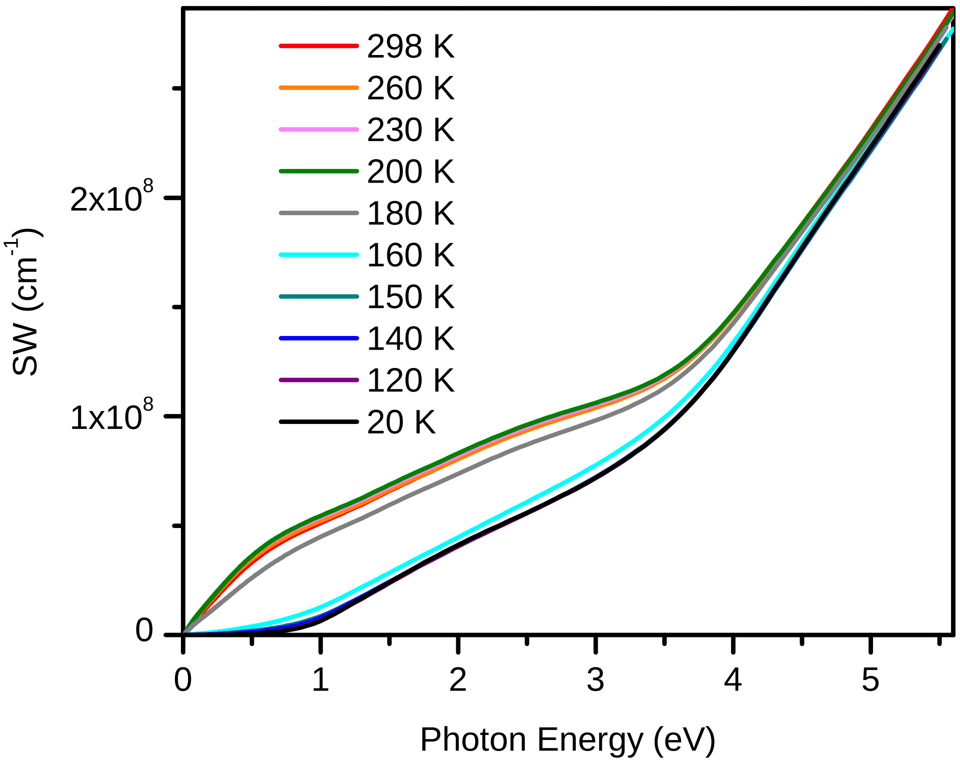

Figure 5.5: Effective electronic spectral weight of V_2O_3 obtained from the spectra in Fig.5.1 using Eq.(5.2).

to the strongly correlated nature of V_2O_3. First, we note that the insulating gap present in the optical conductivity gradually becomes filled with states as the temperature increases, without reducing the magnitude of the energy gap. This effect gives rise to a well-defined Drude resonance A and an incoherent peak B and constitutes a signature of Mott driven IMT. At the same time, the SW of the interband transitions immediately above the gap and up to 5 eV is reduced significantly. The SW(ω) at all the measured temperatures shown in Fig.5.5 reveals that the optical conductivity of to 5 eV must be considered in order to fully account for the low frequency increase in spectral weight observed across the IMT. Such a large energy scale for SW transfer is consistent with the Mott-Hubbard model: The emerging Drude response is the result of a quasiparticle peak forming at the Fermi level at the expense of the Hubbard bands, separated by an energy U. We note that the data in Fig.5.5 are at odds with earlier measurements of V_2O_3 films for which the low temperature SW does not recover the values measured for the metallic phase even at 6 eV. This is related to the higher optical conductivity observed in the present study for the interband transitions between 1 and 3 eV. Knowing that the bandwidth of the t_{2g} manifold in V_2O_3 is very sensitive to extrinsic factors such as doping and pressure and quite possibly strain and impurities, it is likely that this difference is associated with the higher quality of our films, evidenced also by the stronger Drude resonance.

In addition to the large energy scale for SW transfer, indications of a pseudogap and the low temperature increase in the mass enhancement factor (Fig.5.4) highlight the importance of electronic correlations in driving the IMT. While evidence of a pseudogap in the optical conductivity of V_2O_3 above 450 K (in the *crossover* region) is presented in Ref.[6], here we focus on lower temperatures closer to the AFI to PM transition. We find that the partial gapping of the Fermi surface is occurring in spite of the high metallicity of our films, which differs from the bad-metallic behavior of the *crossover* phase reported in Ref.[6]. Furthermore, the peak feature in $1/\tau(\omega)$ is more pronounced at lower temperatures, closer to the IMT. Thus, we propose that pseudogap is linked to the AFI to PM transition and is indicative of the importance of Mott physics in this part of the V_2O_3 phase diagram.

5.3.4 Comparison to VO_2

We now compare our results to previous optical studies of the closely related correlated oxide VO_2. Starting at the far-IR part of the spectra in Fig.5.1 we note that the Drude resonance is much narrower than that observed in VO_2, which extends up to a minimum in $\sigma_1(\omega)$ at 1.7 eV.[102, 104] The plasma frequency of VO_2 is thus more than two times higher than the $\omega_p = 1.25$ eV we have obtained for V_2O_3. From the extended Drude analysis we find that the peak structure found in $1/\tau(\omega)$ in Fig.5.4 (b) indicating the formation of a pseudogap as the IMT is approached is not present in VO_2.[102] Additionally, the mass enhancement factor is higher in V_2O_3. All these observations indicated that electronic correlations are stronger in V_2O_3 than in VO_2.

On the other hand, the optical conductivity of the metallic puddles found in the phase coexistence regime across the IMT in VO_2 bear a closer resemblance to our data.[101] In this case, the $\sigma_1(\omega)$ spectra in Fig.4 of Ref.[101] exhibit a very narrow Drude resonance followed by a dip and an incoherent peak centered at 0.25 eV, similar to the V_2O_3 data in Fig.5.4(a). Furthermore, the scattering rate reveals evidence of a pseudogap, albeit much more marked that in our V_2O_3 data. We propose that this similarity between the V_2O_3 data and that of the more strongly correlated metallic puddles of VO_2 could signify a difference in the way the IMT takes place in these two vanadates. In VO_2, the strongly correlated metallic regions form within an insulating background and grow as the temperature is increased, eventually taking over the entire sample and transitioning into the rutile metal phase. In order to observe the large mass enhancement and the pseudogap it was necessary to separate the contributions from the metallic and insulating regions across the transition. In V_2O_3, on the other hand, the IMT could be occurring in a much more homogenous manner with less spatial variation of the optical constants on the nanoscale. Evidence of the very strongly correlated nature of the V_2O_3 metal near the transition can thus be observed even in far-field measurements averaging over the optical constants of macroscopic regions.

A similar contrast is evident in time-resolved spectroscopy studies of the photo-induced phase transition in VO_2[48] and V_2O_3.[72] In the former, the fluence required to drive the system across the IMT decreases as the temperature approaches T_c. The authors of Ref.[48] attribute this phenomenon to the percolative nature of the transition: the presence of metallic precursors reduces the amount of energy needed to reach the homogeneous metallic state. This dependence of the threshold fluence on the initial temperature of the sample is not reported for V_2O_3,[72] consistent with out proposal that phase separation in the vicinity of the IMT is more prominent in VO_2. In addition to the far-field and time-domain spectroscopy studies of V_2O_3, low temperature scanning near-field infrared microscopy would be the ideal tool to further investigate this issue.

Finally, we comment on an important difference between the phase diagrams of the two materials. While VO_2 exhibits a single IMT at 340 K, V_2O_3 presents a high temperature *crossover* phase with poor metallic properties,[97] in addition to the paramagnetic metallic and antiferromagnetic insulating phases studied here. By applying external pressure or doping with Chromium, the temperature range over which the sample is metallic is significantly reduced and and a high temperature paramagnetic insulating phase emerges.[77, 108] Thus, as the temperature is raised beyond $T_c \approx 150$ K, V_2O_3 enters the metallic state but then begins to approach the *crossover* region, precluding the system from evolving into a less correlated metal like VO_2 does. For this reason, the spectra in Figs.5.1 and 5.4 have more in common with the metallic puddles found very close to the IMT in VO_2 [101] than with the high temperature rutile phase away from the transition.[102] Furthermore, $K_{exp}/K_{LDA} \approx 0.5$ for VO_2,[103, 104] much higher than the value we have obtained for V_2O_3. This interpretation is consistent with studies of chromium doped V_2O_3,[108] where the optical conductivity of the paramagnetic metallic phase exhibits a bad metal behavior with no well-defined Drude resonance,[73] suggestive of enhanced correlations in the region between the antiferromagnetic and paramagnetic insulating states.

5.3.5 Annealed V_2O_3

In Fig.5.6(a) we show the optical conductivity obtained for the annealed V_2O_3 film. It is immediately evident that the magnitudes of the Drude resonance and the incoherent peak B are dramatically suppressed compared to the data for the pristine sample (Fig.5.1). Additionally, the difference between the spectral weight of the interband transitions up to 5 eV in the insulating and metallic states is not as marked as it is in Fig.5.1. SW(ω) at 5.5 eV however, is similar for both samples (Figs.5.5 and 5.6(b)). In other words, the annealing process causes a redistribution of SW in the metallic state, from the low frequency features associated with the e_g^π and a_{1g} QP to the optical conductivity above 1 eV related to the Hubbard bands. Finally, we note that the weak Drude and the incoherent peak of comparable magnitude are reminiscent of earlier data for V_2O_3 thin films,[104] although the DC conductivity reported here is still $\sim 100\%$ higher than in Ref.[104]. We thus conclude that the enhanced Drude spectral weight we have measured in our pristine V_2O_3 films is indeed related to an increased QP density of states and

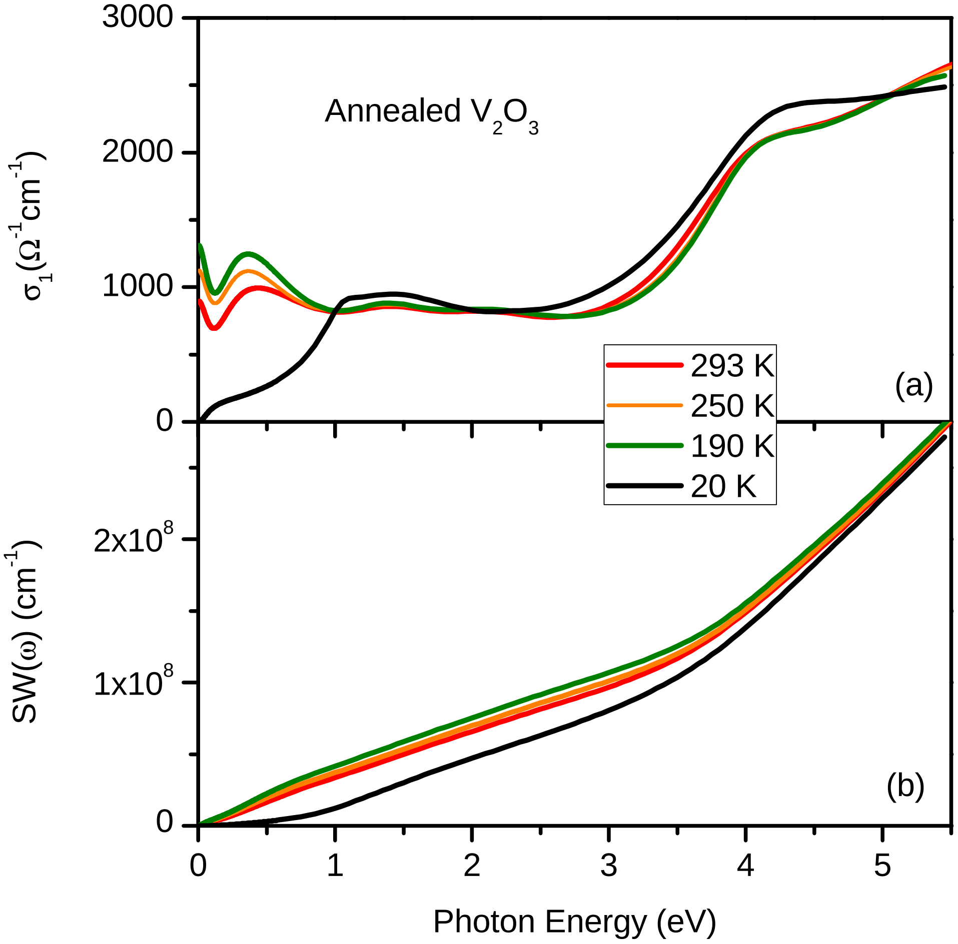

Figure 5.6: Real part of the optical conductivity (a) and effective spectral weight (b) obtained for the annealed V_2O_3 sample.

cannot be attributed solely to an overall shift in the $\sigma_1(\omega)$ values.

5.4 Conclusions

We have presented an optical study of V_2O_3 thin films providing evidence that electronic correlations play an important role in the AFI to PM transition. We find that the temperature driven transfer of spectral weight, both within the metallic state and across the IMT, is consistent with the Mott-Hubbard model for correlated systems. The extended Drude analysis, facilitated by the well-defined coherent response of our sample, reveals new signatures of strong correlations in the metallic state: i) the formation of a pseudogap and ii) the enhancement of the carrier effective mass as the IMT is approached. Finally, we propose that the similarities between our data and the metallic puddles of phase separated VO_2 indicate that electronic correlations remain quite prevalent even as temperatures is raised past the immediate vicinity of the IMT.

Acknowledgements

Chapter 6, in full, is currently being prepared for submission for publication of the material. M.K. Stewart, D. Brownstead, K. W. West, S. Wang, J. G. Ramirez, I. K. Schuller, and D. N. Basov. The dissertation author was the primary investigator and author of this material.

Chapter 6

Ellipsometric study of the electronic band structure of CrO_2 across the ferromagnetic transition

Abstract

The optical properties of half metallic CrO_2 at temperatures below, at, and above the Curie temperature are studied by means of variable angle spectroscopic ellipsometry. The films were epitaxially grown on (100) and (110) oriented TiO_2 substrates by chemical vapor deposition. Optical conductivity data reveal a pronounced anisotropy of the optical constants for all films which is in good agreement with what is known about their crystal structure. The main features of the conductivity spectra in the ferromagnetic state are consistent with existing band structure calculations. However, no temperature dependence of these features across the ferromagnetic transition is evident, posing questions about the electronic structure of the material.

6.1 Introduction

According to band structure calculations CrO_2 is classified as a half-metallic ferromagnet with complete spin polarization at the Fermi energy.[116, 136, 63] This has sparked a renewed interest in this material as a candidate for spin injection in spintronics applications. The prediction has been confirmed by point contact Andreev reflection measurements showing 96-98% spin polarization.[58, 3] Other experiments such as x-ray absorption,[67] photoemission [139] and optical measurements [119] performed below the Curie temperature show general agreement with band structure calculations in the ferromagnetic state. Work done to study the electromagnetic response of this material across the ferromagnetic transition is limited to absorption [142, 144] and pump-probe transmission [51] studies claiming to confirm a double-exchange mechanism of the ferromagnetic state. Within this latter scenario, major changes in the optical conductivity are expected across the ferromagnetic transition.[90] A comprehensive study of the optical properties across T_C in both the c-axis and ab-plane directions should help further our understanding of this half-metal. While it is well known that the crystal structure of CrO_2 is anisotropic,[132] experimental studies of the anisotropy in the optical response of thin films are also very limited.[51, 124]

In this paper, we study the frequency dependent optical conductivity of CrO_2 over a wide temperature and energy range in order to learn about its electronic band structure and carrier dynamics across the ferromagnetic transition. We employed variable angle spectroscopic ellipsometry (VASE): a technique that allows us to extract both the real and imaginary parts of the optical conductivity without recourse to Kramers-Kronig analysis.

6.2 Experimental Methods

The samples are epitaxial CrO_2 thin films grown on TiO_2 substrates by chemical vapor deposition with CrO_3 as a precursor. Sample growth and characterization using x-ray diffraction, Rutherford back scattering spectroscopy, several microscopy techniques and a standard four-probe dc method are described elsewhere.[43, 26, 79] We used two different samples, one deposited on TiO_2 in the (100) orientation with a thickness of 175 nm, and one in the (110) orientation, 150 nm thick. The (100) film is strained while the (110) film is strain free.[125, 26, 79] The reported Curie temperature of these films is T_C=390-395 K and the magnetic easy axis is the *c*-axis.[43]

We performed the measurements using two commercial Woollam ellipsometers. One, a VASE model based on a grating monochromator, covers the energy range between 0.6 and 6 eV, to which we added a UHV cryostat in order to enable measurements at both low and elevated temperatures.[19, 104] The other one, an IR-VASE model, covers the range between 0.05 and 0.7 eV and is based on a Michelson interferometer (Bruker 66vs). We first characterized the blank (100) and (110) substrates and then the films. Knowing that the crystal structure of CrO_2 is elongated along the c direction, it is natural to expect the electronic properties to be anisotropic.[51] In order to study the optical constants in the various crystallographic directions, it was necessary to measure the samples in two orientations: with the *c*-axis in the plane of incidence and perpendicular to it. A schematic of these experimental geometries is shown in Fig. 6.1. Each measurement was performed at incidence angles of 60° and 75° and at temperatures ranging from 300 to 450 K, while some measurements in the visible and ultraviolet region were extended down to 60 K. At each angle we measured the polarization state of the reflected light in the form of two parameters Ψ and Δ, as shown in Fig. 6.1, which are related to the Fresnel reflection coefficients for p- and s-polarized light (R_p and R_s) through the equation: $\frac{R_p}{R_s} = tan(\Psi)e^{i\Delta}$. We note that there is good agreement, better than 3%, between the data obtained from the two different ellipsometers in the overlapping frequency range.

In order to obtain the optical constants of the thin film samples, we first constructed a 2-layer model taking proper account of the role of the substrate in raw ellipsometric data. The complex dielectric functions of the TiO_2 required for this analysis were determined through ellipsometric measurements of the bare substrates, keeping in mind the anisotropy of this uniaxial crystal. The same model of the optical constants tensor has been employed to fit the four sets of experimental

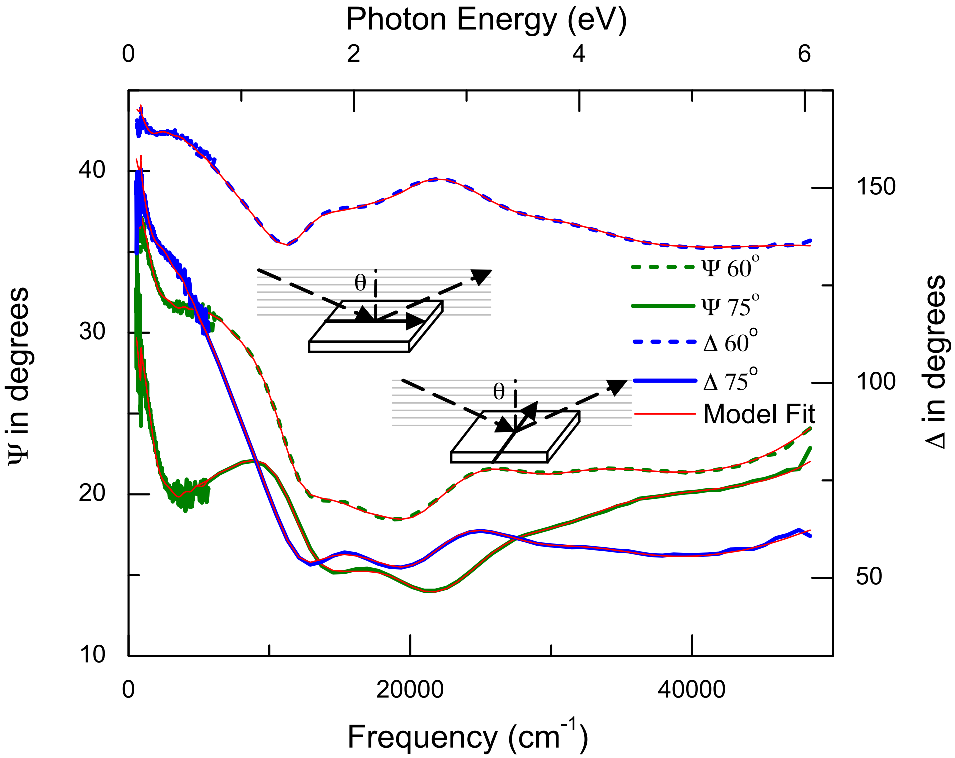

Figure 6.1: Room temperature ellipsometry data for (110) CrO_2 film with *c*-axis in the plane of incidence. Ψ and Δ were measured at incidence angles of 60° and 75°. The red line shows the fit from the constructed model. Inset: schematic of the experimental geometry with *c*-axis in the plane of incidence (top) and *c*-axis perpendicular to plane of incidence (bottom). The dashed arrows represent the incident and reflected beams, with angle of incidence θ. The solid arrow indicates the direction of the c-axis.

data for TiO_2 collected at 60° and 75° with the *c*-axis both perpendicular and parallel to the plane of incidence. In this way we were able to obtain the conductivity for both the *c*-axis and the *ab*-plane of each of the two TiO_2 samples. Our data are in good agreement with those obtained in previous experiments.[56, 133] To account for surface roughness in the substrate, we included in our model a top layer consisting of 50% void and 50% TiO_2 and described the response of such an effective layer with the Bruggeman Effective Medium Approximation.[57] The thickness of the layer was determined by the model fit to be 4 nm. Data for the CrO_2/TiO_2 films were modeled in a similar way. Specifically, we used the optical constants previously obtained for TiO_2 to characterize the substrate so that the only fit parameters were the optical constants of CrO_2 in the *c*-axis and *ab*-plane directions. The CrO_2 layer of the model is composed of two separate sets of eight Kramers-Kronig consistent gaussian oscillators [31] and a Drude function, amounting to 26 fit parameters. Two sets of oscillators are necessary because we want to describe the response along each of the two crystallographic directions. Fig. 6.1 shows experimental data and the model fits for measurements of the (110) sample performed at room temperature with the *c*-axis in the plane of incidence. It can be seen that our model provides good fits, within 5%, for the data at both angles throughout the entire experimental range.

6.3 Results and Discussion

In order to analyze our results, it is useful to look at the real, dissipative part of the optical conductivity, as it is related to the density of states. The complex optical conductivity can be obtained from the complex dielectric function using $\sigma(\omega) = \frac{i\omega(1-\epsilon(\omega))}{4\pi}$. Fig. 6.2 shows conductivity data for both CrO_2 samples at room temperature. The spectra show three main features: (i) a Drude contribution at low frequencies, (ii) a broad peak in the mid-IR region (0.2-1.5 eV), and (iii) a sharp onset of interband absorption at 1.5 eV indicative of a prominent band gap. Comparing our data with band structure calculations [136, 75] it is tempting to assign feature (iii) to transitions across the minority gap between

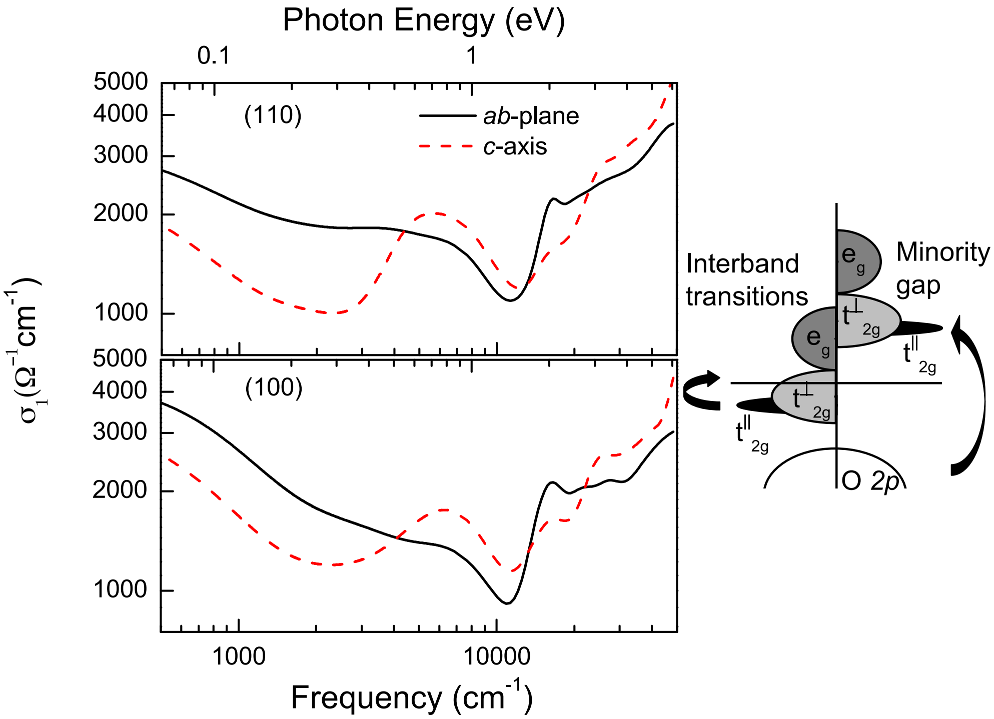

Figure 6.2: Real part of the optical conductivity of (110) CrO_2 (top panel) and (100) CrO_2 at room temperature in both *ab*-plane and *c*-axis directions. Right panel: sketch of the density of states of CrO_2.[136]

the oxygen $2p$ and the chromium $3d$ bands, estimated by LSDA calculations to be 1.3 eV. Furthermore, transitions between the $t^{||}_{2g}$ and the e_g levels (see right panel in Fig. 6.2) may contribute to absorption above 1.5 eV. Feature (ii) would correspond to interband transitions between the split t_{2g} levels. Based on this analysis, one might conclude that our data support the LSDA calculations more so than LSDA+U calculations. The latter include a Hubbard U term to account for intra-atomic Coulomb repulsion and predict a larger spin minority gap of 2.1 eV, which is inconsistent with our results. While existing band structure calculations are valid at very low temperatures, dramatic changes in the band structure are not expected at higher temperatures below T_C.

Data in Fig. 6.2-6.4 reveal significant anisotropy in the CrO_2 films throughout the entire frequency range of our measurements. Fig. 6.3 shows DC conductivity, scattering rate $(1/\tau)$, and Drude plasma frequency (ω_p) data obtained from the Drude functions in our models. These spectral features are related to the Drude contribution of the optical conductivity by $\sigma_{Drude}(\omega) = \frac{\omega_p^2}{4\pi(1/\tau - i\omega)}$. The plasma frequency we have obtained experimentally is somewhat lower than the LSDA prediction of ~ 2 eV.[69] At room temperature, the DC conductivity and the Drude plasma frequency in the *ab*-plane are about 30% higher than in the direction of the c-axis. Going back to Fig. 6.2 we note that this trend continues until about 0.5 eV. This is consistent with the knowledge that one of the $t_{2g}^{\perp}$ levels at the Fermi energy is hybridized with the oxygen $2p_y$ state forming a Π-type bond normal to the *c*-axis.[124] In this way, some of the electrons at the Fermi energy can contribute to conductivity in the *ab*-plane only. In the mid-IR region, the *c*-axis conductivity shows a well defined peak while in the *ab*-plane conductivity we see a broad shoulder. At higher frequencies the anisotropy becomes smaller with the conductivity along both directions showing a rapid increase above 1.5 eV. In the *ab*-plane response we see a more pronounced peak at 2 eV followed by a slower increase in conductivity at even higher energies. The response probed along the *c*-axis direction reveals a more uniform increase in the conductivity, although peaks at 2 eV and 3 eV are still noticeable.

To further understand the band structure of CrO_2 it is crucial to study the temperature dependence of the conductivity, especially near T_C and across the ferromagnetic transition. Fig. 6.4 shows temperature dependence of the optical conductivity for both films. It is important to note that the absorption region (iii) with onset at 1.5 eV exhibits virtually no temperature dependence, prevailing well above T_C. Noticeable temperature dependence is observed in the mid infrared region. In the case of the (110) film, the amplitude of this peak increases and its center becomes red-shifted as temperature increases. In the (100) film we observe that, in the *c*-axis direction, this peak broadens but its amplitude does not increase, while in the *ab*-plane we see no clear peak in this region. The Drude free carrier absorption at the lowest energies is modified as well. As shown in Fig. 6.3, the DC conductivity decreases and the scattering rate increases with increasing temperature. Above T_C, hints of saturation in the scattering rate are apparent, presumably due to the small electron mean free path expected in the paramagnetic state.[69] The Drude plasma frequency remains approximately constant at all temperatures.

This finding is in conflict with the double-exchange scenario of ferromagnetism in CrO_2 predicting a noticeable spectral weight transfer from high to low energy as temperature is reduced below T_C.[30] This expectation is substantiated by IR data for manganites, where the effective number of carriers decreases continuously with increased temperature, finally vanishing at T_C .[90] This result is also inconsistent with LSDA calculations predicting higher Drude plasma frequency in the paramagnetic state.[69]Similar behavior of the Drude plasma frequency across T_C is also found in ferromagnetic III-V semiconductors.[118, 117] DC conductivity in the *ab*-plane remains higher than that in the *c*-axis direction throughout our entire temperature range, with no discontinuous changes at T_C. These data are in good agreement with resistivity measurements performed on similar (100) CrO_2 samples. [43] We observe a higher scattering rate in the *ab*-plane than in the *c*-axis direction. From Fig. 6.3 we note that the DC conductivity of the (100) film is 30-35% higher than that of the (110) film.

A novel and unanticipated result of our work is that we observe no significant changes either in the Drude absorption or in the interband resonances throughout the broad temperature range covering both the ferromagnetic and paramagnetic states. It is known that strain and strain induced defects can affect the electronic and magnetic properties of thin films. This is a possibility in the (100) film, but not in the (110) film which has been shown to be strain free.[26] Therefore, we expect to see a dramatic difference between the spectra at the low and high ends of our temperature range, the former corresponding to a fully spin polarized ferromagnetic state well below T_C and the latter to a paramagnetic regime well above T_C. However, while the small peaks present at lower temperatures near 2 and 3 eV disappear quickly with increased temperature, the general trend of a sharp absorption starting at 1.5 eV remains unchanged. Therefore, assignment of the high energy absorption to transitions across the minority gap of a half-metallic ferromagnet becomes problematic and is in disagreement with our results. The more noticeable temperature dependence in the mid-IR region might be explained by recalling that this peak could correspond to interband transitions between the split t_{2g} levels. As the temperature is increased and the sample enters the para-

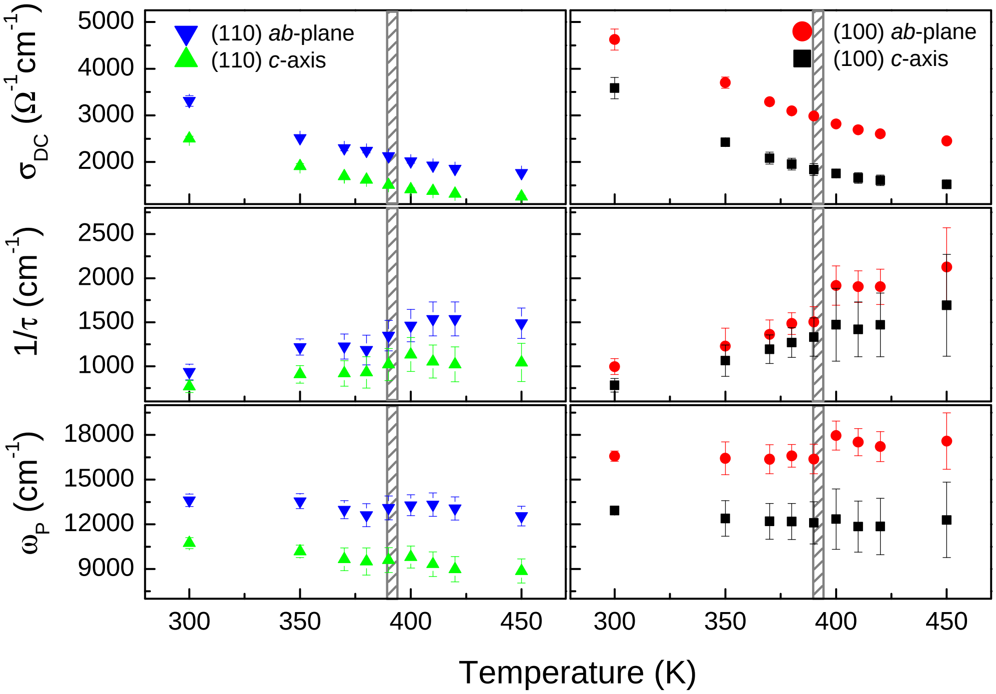

Figure 6.3: DC conductivity (top), scattering rate, and Drude plasma frequency (bottom) as a function of temperature obtained from the Drude function in our model. The vertical bars indicate the Curie temperature. The left column shows data for CrO_2 on (110) TiO_2 and the right column is for CrO_2 on (100) TiO_2

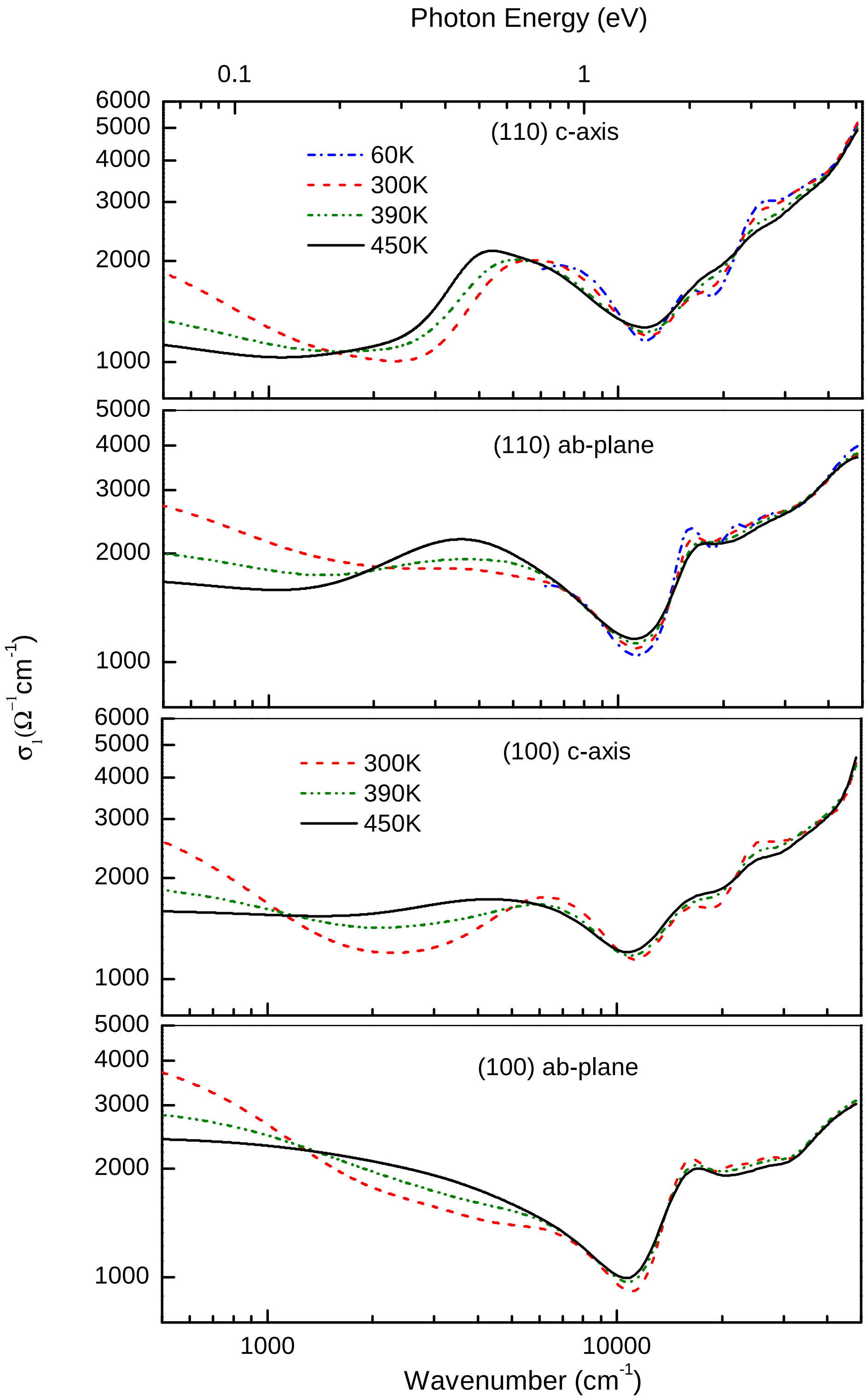

Figure 6.4: Optical conductivity in *ab*-plane and *c*-axis direction of each film at temperatures between 300 and 450 K for the (100) sample and between 60 and 450 K for the (110) sample.

magnetic state, the minority spin levels would presumably go down to the Fermi energy. This would allow excitations of minority spins into the conduction band with less energy, which could contribute to the broadening and increase in magnitude of this peak. In the case of the (100) film we expect the strain along the b-axis to be greater than that along the *c*-axis due to larger lattice mismatch in the direction of the *b*-axis. Since the splitting of the t_{2g} levels is due to the elongation of the oxygen octahedra along the *c*-axis,[63] one might expect that the way in which the t_{2g} levels split will be affected by this strain along the b-axis, causing a difference in the conductivities of the two films in the mid-IR region. The lack of temperature dependence in the plasma frequency as well as in the sharp absorption region above 1.5 eV is in disagreement with the dramatic changes expected in the double-exchange scenario and in the current picture of the band structure of this material.

6.4 Conclusion

We have obtained optical conductivity data for CrO_2 across the ferromagnetic transition at 390 K. The main features observed in our room temperature data appear to be in good agreement with band structure calculations for the fully spin polarized ferromagnetic state. A study of the temperature dependence of the conductivity however, poses new questions about the electronic band structure of this material. We see that the peak which, according to calculations, would correspond to transitions across the minority gap remains quite prominent at temperatures well above T_C. Furthermore, the Drude plasma frequency we obtained is temperature independent, which is inconsistent with the double-exchange scenario. We also observe an important anisotropy in the optical conductivity of CrO_2 and a difference in the conductivities of the two films. These observations are consistent with what is known about the crystal structure of this half-metal and about the strain in the films.

Acknowledgments

Work at UCSD was supported by ONR N00014-08-1-0746.

Chapter 2, in full, is a reprint of the material as it appears in Phys. Rev. B **79**, 144414 (2009). M. K. Stewart, K. B. Chetry, B. Chapler, M. M. Qazilbash, A. A. Schafgans, A. Gupta, T. E. Tiwald, and D. N. Basov. The dissertation author was the primary investigator and author of this paper.

Bibliography

[1] Y. Ando, G. S. Boebinger, A. Passner, T. Kimura, and K. Kishio. Logarithmic Divergence of both In-Plane and Out-of-Plane Normal-State Resistivities of Superconducting $La_{2-x}Sr_xCuO_4$ in the Zero-Temperature Limit. *Phys. Rev. Lett.*, 75:4662, 1995.

[2] Y. Ando, G. S. Boebinger, A. Passner, N. L. Wang, C. Geibel, and F. Steglich. Metallic In-Plane and Divergent Out-of-Plane Resistivity of a High-T_c Cuprate in the Zero-Temperature Limit. *Phys. Rev. Lett.*, 77:2065, 1996.

[3] A. Anguelouch, A. Gupta, G. Xiao, D. W. Abraham, Y. Ji, S. Ingvarsson, and C. L. Chien. Near-complete spin polarization in atomically-smooth chromium-dioxide epitaxial films prepared using a CVD liquid precursor. *Phys. Rev. B*, 64:180408(R), 2001.

[4] T. Arima, Y. Tokura, and J. B. Torrance. Variation of optical gaps in perovskite-type 3d transition-metal oxides. *Phys. Rev. B*, 48:17006, 1993.

[5] T. H. Arima and Y. Tokura. Optical study of electronic-structure in perovskite-type RMO_3 (R=La, Y M=Sc, Ti, V, Cr, Mn, Fe, Co, Ni, Cu). *J. Phys. Soc. Jpn.*, 64:2488, 1995.

[6] L. Baldassarre, A. Perucchi, D. Nicoletti, A. Toschi, G. Sangiovanni, K. Held, M. Capone, M. Ortolani, L. Malavasi, M. Marsi, P. Metcalf, P. Postorino, and S. Lupi. Quasiparticle evolution and pseudogap formation in V_2O_3: An infrared spectroscopy study. *Phys. Rev. B*, 77:113107, 2008.

[7] D. N. Basov, R. D. Averitt, D. van der Marel, M. Dressel, and K. Haule. Electrodynamics of correlated electron materials. *Rev. Mod. Phys.*, 85:471, 2011.

[8] D. N. Basov and A. V. Chubukov. Manifesto for a higher T_c. *Nat. Phys.*, 7:272, 2011.

[9] D. N. Basov, B. Dabrowski, and T. Timusk. Infrared Probe of Transition from Superconductor to Nonmetal in $YBa_2(Cu_{1-x}Zn_x)_4O_8$. *Phys. Rev. Lett.*, 81:2132, 1998.

[10] D. N. Basov, R. Liang, B. Dabrowski, D. A. Bonn, W. N. Hardy, and T. Timusk. Pseudogap and charge dynamics in CuO_2 planes in YBCO. *Phys. Rev. Lett.*, 77:4090, 1996.

[11] D. N. Basov, A. V. Puchkov, R. A. Hughes, T. Strach, J. Preston, T. Timusk, D. A. Bonn, R. Liang, and W. N. Hardy. Disorder and superconducting-state conductivity of single crystals of $YBa_2Cu_3O_{6.95}$. *Phys. Rev. B*, 49:12165, 1994.

[12] D. N. Basov, E. J. Singley, and S. V. Dordevic. Sum rules and electrodynamics of high-T_c cuprates in the pseudogap state. *Phys. Rev. B*, 65:054516, 2002.

[13] D. N. Basov and T. Timusk. Electrodynamics of high-T_c superconductors. *Rev. Mod. Phys.*, 77:721, 2005.

[14] D. N. Basov, S. I. Woods, A. S. Katz, E. J. Singley, R. C. Dynes, M. Xu, D. G. Hinks, C. C. Homes, and M. Strongin. Sum rules and interlayer conductivity of High-T_c cuprates. *Science*, 283:49, 1999.

[15] E. Benckiser, M. W. Haverkort, S. Bruck, E. Goering, S. Macke, A. Frano, X. P. Yang, O. K. Andersen, G. Cristiani, H. U. Habermeier, A. V. Boris, I. Zegkinoglou, P. Wochner, H. J. Kim, V. Hinkov, and B. Keimer. Orbital reflectometry of oxide heterostructures. *Nat. Mat.*, 10:189, 2011.

[16] L. Benfatto, J. P. Carbotte, and F. Marsiglio. Temperature dependence of the conductivity sum rule in the normal state due to inelastic scattering. *Phys. Rev. B*, 74:155115, 2006.

[17] B. Berini, N. Keller, Y. Dumont, E. Popova, W. Noun, M. Guyot, J. Vigneron, A. Etcheberry, N. Franco, and R. M. C. da Silva. Reversible phase transformation of $LaNiO_{3-x}$ thin films studied in situ by spectroscopic ellipsometry. *Phys. Rev. B*, 76:205417, 2007.

[18] P. Blaha, K. Schwartz, G. K. H. Madsen, D. Kvasnicka, and J. Luitz. *An Augmented Plane Wave + Local Orbitals Program for Calculating Crystal Properties.* Karlheinz Schwarz, Techn. Universitat Wien, Austria, 2001.

[19] K. S. Burch, J. Stephens, R. K. Kawakami, D. D. Awschalom, and D. N. Basov. Ellipsometric study of the electronic structure of $Ga_{1-x}Mn_xAs$ and low-temperature GaAs. *Phys. Rev. B*, 70:205208, 2004.

[20] S. M. Butorin, C. Sathe, A. Agui, F. Saalem, J. A. Alonso, and J. Nordgren. Intra-versus inter-site electronic excitations in $NdNiO_3$ by resonant inelastic ultra-soft X-ray scattering at Ni 3p edge. *Solid State Comm.*, 135:716, 2005.

[21] P. C. Canfield, J. D. Thompson, S. W. Cheong, and L. W. Rupp. Extraordinary pressure-dependence of the metal-to-insulator transition in the charge-transfer compounds $NdNiO_3$ and $PrNiO_3$. *Phys. Rev. B*, 47:12357, 1993.

[22] M. Cardona. Optical properties and band structure of $SrTiO_3$ and $BaTiO_3$. *Phys. Rev.*, 140:A651, 1965.

[23] G. Catalan. Progress in perovskite nickelate research. *Phase Transitions*, 81:729, 2008.

[24] J. Chakhalian, J. M. Rondinelli, Jian Liu, B. A. Gray, M. Kareev, E. J. Moon, N. Prasai, J. L. Cohn, M. Varela, I. C. Tung, M. J. Bedzyk, S. G. Altendorf, F. Strigari, B. Dabrowski, L. H. Tjeng, P. J. Ryan, and J. W. Freeland. Asymmetric orbital-lattice interactions in ultrathin correlated oxide films. *Phys. Rev. Lett.*, 107:116805, 2011.

[25] J. Chaloupka and G. Khaliullin. Orbital Order and Possible Superconductivity in $LaNiO_3/LaMO_3$ Superlattices. *Phys. Rev. Lett.*, 100:016404, 2008.

[26] K. B. Chetry, M. Pathak, P. LeClair, and A. Gupta. Structural and magnetic properties of (100)-and (110)-oriented epitaxial CrO_2 films. *J. Appl. Phys.*, 105:083925, 2009.

[27] Y. D. Chuang, A. D. Gromko, D. S. Dessau, T. Kimura, and Y. Tokura. Fermi surface nesting and nanoscale fluctuating charge/orbital ordering in colossal magnetoresistive oxides. *Science*, 292:1509, 2001.

[28] S. Ciuchi and S. Fratini. Signatures of polaronic charge ordering in optical and dc conductivity using dynamical mean field theory. *Phys. Rev. B*, 77:205127, 2008.

[29] S. L. Cooper, D. Reznik, A. Kotz, M. A. Karlow, R. Liu, M. V. Klein, W. C. Lee, J. Giapintzakis, D. M. Ginsberg, B. W. Veal, and A. P. Paulikas. Optical studies of the a-axis, b-axis, and c-axis charge dynamics in $YBa_2Cu_3O_{6+x}$. *Phys. Rev. B*, 47:8233, 1993.

[30] L. Craco, M. S. Laad, and E. Müller-Hartmann. Orbital Kondo Effect in CrO_2: A Combined Local-Spin-Density-Approximation Dynamical-Mean-Field-Theory Study. *Phys. Rev. Lett.*, 90:237203, 2003.

[31] D. De Sousa Meneses, M. Malki, and J. Echegut. Structure and lattice dynamics of binary lead silicate glasses investigated by infrared spectroscopy. *Non-Cryst. Solids*, 352:769, 2006.

[32] P. D. Dernier and M. Marezio. Crystal structure of the low-temperature antiferromagnetic phase of V_2O_3. *Phys. Rev. B*, 2:3771, 1970.

[33] G. Deutscher, A. F. Santander-Syro, and N. Bontemps. Kinetic energy change with doping upon superfluid condensation in high-temperature superconductors. *Phys. Rev. B*, 72:3, 2005.

[34] S. Di Matteo, N. B. Perkins, and C. R. Natoli. Spin-1 effective Hamiltonian with three degenerate orbitals: An application to the case of V_2O_3 . *Phys. Rev. B*, 65:054413, 2002.

[35] R. Eguchi, A. Chainani, M. Taguchi, M. Matsunami, Y. Ishida, K. Horiba, Y. Senba, H. Ohashi, and S. Shin. Fermi surfaces, electron-hole asymmetry, and correlation kink in a three-dimensional Fermi liquid $LaNiO_3$. *Phys. Rev. B*, 79:115122, 2009.

[36] D. Emin. Optical properties of large and small polarons and bipolarons. *Phys. Rev. B*, 48:13691, 1993.

[37] S. Y. Ezhov, V. I. Anisimov, D. I. Khomskii, and G. A. Sawatzky. Orbital occupation, local spin, and exchange interactions in V_2O_3. *Phys. Rev. Lett.*, 83:4136, 1999.

[38] D. Franta, D. Necas, and I. Ohlidal. Anisotropy-enhanced depolarization on transparent film/substrate system. *Thin Solid Films*, 519:2631, 2010.

[39] J. L. Garciamunoz, J. Rodriguezcarvajal, and P. Lacorre. Neutron-diffraction study of the magnetic-ordering in the insulating regime of the perovskites $RNiO_3$ (R=Pr and Nd). *Phys. Rev. B*, 50:978, 1994.

[40] J. L. Garciamunoz, J. Rodriguezcarvajal, P. Lacorre, and J. B. Torrance. Neutron-diffraction study of $RNiO_3$ (R = La,Pr,Nd,Sm) - electronically induced structural-changes across the metal-insulator-transition. *Phys. Rev. B*, 46:4414, 1992.

[41] F. Gervais. Optical conductivity of oxides. *Mat. Sci. Eng. R*, 39:29, 2002.

[42] J. B. Goodenough. Electronic and ionic transport properties and other physical aspects of perovskites. *Rep. Prog. Phys.*, 67:1915, 2004.

[43] A. Gupta, X. W. Li, and G. Xiao. Magnetic and transport properties of epitaxial and polycrystalline chromium dioxide thin films. *J. Appl. Phys.*, 87:6073, 2000.

[44] P. Hansmann, X. P. Yang, A. Toschi, G. Khaliullin, O. K. Andersen, and K. Held. Turning a Nickelate Fermi Surface into a Cupratelike One through Heterostructuring. *Phys. Rev. Lett.*, 103:016401, 2009.

[45] K. Haule, C. H. Yee, and K. Kim. Dynamical mean-field theory within the full-potential methods: Electronic structure of $CeIrIn_5$, $CeCoIn_5$, and $CeRhIn_5$. *Phys. Rev. B*, 81:30, 2010.

[46] K. Held, G. Keller, V. Eyert, D. Vollhardt, and V. I. Anisimov. Mott-Hubbard Metal-Insulator Transition in Paramagnetic V_2O_3: An $LDA + DMFT$(QMC) Study. *Phys. Rev. Lett.*, 86:5345, 2001.

[47] G. Herranz, B. Martinez, J. Fontcuberta, F. Sanchez, C. Ferrater, M. V. Garcia-Cuenca, and M. Varela. Enhanced electron-electron correlations in nanometric $SrRuO_3$ epitaxial films. *Phys. Rev. B*, 67:174423, 2003.

[48] D. J. Hilton, R. P. Prasankumar, S. Fourmaux, A. Cavalleri, D. Brassard, M. A. El Khakani, J. C. Kieffer, A. J. Taylor, and R. D. Averitt. Enhanced photosusceptibility near T_c for the light-induced insulator-to-metal phase transition in vanadium dioxide. *Phys. Rev. Lett.*, 99:226401, 2007.

[49] C. C. Homes, M. Reedyk, D. A. Cradles, and T. Timusk. Technique for measuring the reflectance of irregular, submillimeter-sized samples. *Appl. Opt.*, 32:2976, 1993.

[50] K. Horiba, R. Eguchi, M. Taguchi, A. Chainani, A. Kikkawa, Y. Senba, H. Ohashi, and S. Shin. Electronic structure of $LaNiO_{3-x}$: An in situ soft x-ray photoemission and absorption study. *Phys. Rev. B*, 76:155104, 2007.

[51] H. Huang, K. Seu, A. Reilly, Y. Kadmon, and W. F. Egelhoff. Temperature, wavelength, and polarization dependent time resolved optical spectroscopy of half-metallic CrO_2. *J. Appl. Phys.*, 97:10C309, 2005.

[52] M. Imada, A. Fujimori, and Y. Tokura. Metal-insulator transitions. *Rev. Mod. Phys.*, 70:1039, 1998.

[53] T. Ishikawa, T. Kimura, T. Katsufuji, and Y. Tokura. Optical probe of anisotropic and incoherent charge dynamics in a layered ferromagnet: $La_{1.2}Sr_{1.8}Mn_2O_7$. *Phys. Rev. B*, 57:R8079, 1998.

[54] A. Jayaraman, D. B. McWhan, J. P. Remeika, and P. D. Dernier. Critical Behavior of the Mott Transition in Cr-Doped V_2O_3. *Phys. Rev. B*, 2:3751, 1970.

[55] G. E. Jellison. Data Analysis for Spectroscopic Ellipsometry. In H. G. Tompkins and E. A. Irene, editors, *Handbook of Ellipsometry*, pages 237–296. William Andrew Publishing/Springer Verlag, 2005.

[56] G. E. Jellison, F. A. Modine, and L. A. Boatner. Measurement of the optical functions of uniaxial materials by two-modulator generalized ellipsometry: rutile TiO_2. *Opt. Lett.*, 22:1808, 1997.

[57] J. G. E. Jellison, L. A. Boatner, D. H. Lowndes, R. A. McKee, and M. Godbole. Optical functions of transparent thin films of $SrTiO_3$, $BaTiO_3$, and SiO_x determined by spectroscopic ellipsometry. *Appl. Opt.*, 33:6053, 1994.

[58] Y. Ji, G. J. Strijkers, F. Y. Yang, C. L. Chien, J. M. Byers, A. Anguelouch, G. Xiao, and A. Gupta. Determination of the Spin Polarization of Half-Metallic CrO_2 by Point Contact Andreev Reflection. *Phys. Rev. Lett.*, 86:5585, 2001.

[59] M. Kareev, S. Prosandeev, J. Liu, C. Gan, A. Kareev, J. W. Freeland, M. Xiao, and J. Chakhalian. Atomic control and characterization of surface defect states of TiO_2 terminated $SrTiO_3$ single crystals. *Appl. Phys. Lett.*, 93:061909, 2008.

[60] T. Katsufuji, Y. Okimoto, T. Arima, Y. Tokura, and J. B. Torrance. Optical spectroscopy of the metal-insulator-transition in $NdNiO_3$. *Phys. Rev. B*, 51:4830, 1995.

[61] A. S. Katz, S. I. Woods, E. J. Singley, T. W. Li, M. Xu, D. G. Hinks, R. C. Dynes, and D. N. Basov. Interlayer conductivity in the superconductor $Tl_2Ba_2CuO_{6+\delta}$: Energetics and energy scales. *Phys. Rev. B*, 61:5930, 2000.

[62] A. R. Kaul, O. Yu Gorbenko, and A. A. Kamenev. The role of heteroepitaxy in the development of new thin-film oxide-based functional materials. *Russ. Chem. Rev.*, 73:861, 2004.

[63] M. A. Korotin, V. I. Anisimov, D. I. Khomskii, and G. A. Sawatzky. CrO_2: A Self-Doped Double Exchange Ferromagnet. *Phys. Rev. Lett.*, 80:4305, 1998.

[64] G. Kotliar, S. Y. Savrasov, K. Haule, V. S. Oudovenko, O. Parcollet, and C. A. Marianetti. Electronic structure calculations with dynamical mean-field theory. *Rev. Mod. Phys.*, 78:865, 2006.

[65] N. N. Kovaleva, A. V. Boris, C. Bernhard, A. Kulakov, A. Pimenov, A. M. Balbashov, G. Khaliullin, and B. Keimer. Spin-controlled mott-hubbard bands in $LaMnO_3$ probed by optical ellipsometry. *Phys. Rev. Lett.*, 93:147204, 2004.

[66] Y. Kumar, R. J. Choudhary, A. P. Singh, G. Anjum, and R. Kumar. Evidence of quantum correction to conductivity in strained epitaxial $LaNiO_3$ films. *J. Appl. Phys.*, 108:083706, 2010.

[67] E. Z. Kurmaev, A. Moewes, S. M. Butorin, M. I. Katsnelson, L. D. Finkelstein, J. Nordgren, and P. M. Tedrow. Half-metallic electronic structure of CrO_2 in resonant scattering. *Phys. Rev. B*, 67:155105, 2003.

[68] A. B. Kuzmenko. Kramers-Kronig constrained variational analysis of optical spectra. *Rev. Sci. Inst.*, 76:083108, 2005.

[69] S. P. Lewis, P. B. Allen, and T. Sasaki. Band structure and transport properties of CrO_2. *Phys. Rev. B.*, 55:10253, 1997.

[70] P. Limelette, A. Georges, D. Jerome, P. Wzietek, P. Metcalf, and J. M. Honig. Universality and critical behavior at the Mott transition. *Science*, 302:89, 2003.

[71] J. A. Liu, M. Kareev, B. Gray, J. W. Kim, P. Ryan, B. Dabrowski, J. W. Freeland, and J. Chakhalian. Strain-mediated metal-insulator transition in epitaxial ultrathin films of $NdNiO_3$. *Appl. Phys. Lett.*, 96:233110, 2010.

[72] M. K. Liu, B. Pardo, J. Zhang, M. M. Qazilbash, S. J. Yun, Z. Fei, J. H. Shin, H. T. Kim, N. Basov, and R. D. Averitt. Photoinduced Phase Transitions by Time-Resolved Far-Infrared Spectroscopy in V_2O_3. *Phys. Rev. Let.*, 107:066403, 2011.

[73] S. Lupi, L. Baldassarre, B. Mansart, A. Perucchi, A. Barinov, P. Dudin, E. Papalazarou, F. Rodolakis, J. P. Rueff, J. P. Itie, S. Ravy, D. Nicoletti, P. Postorino, P. Hansmann, N. Parragh, A. Toschi, T. Saha-Dasgupta, O. K. Andersen, G. Sangiovanni, K. Held, and M. Marsi. A microscopic view on the Mott transition in chromium-doped V_2O_3. *Nat. Comm.*, 1:105, 2010.

[74] S. J. May, J.-W. Kim, J. M. Rondinelli, E. Karapetrova, N. A. Spaldin, A. Bhattacharya, and P. J. Ryan. Quantifying octahedral rotations in strained perovskite oxide films. *Phys. Rev. B*, 82:014110, 2010.

[75] I. I. Mazin, D. J. Singh, and C. Ambrosch-Draxl. Transport, optical, and electronic properties of the half-metal CrO_2. *Phys. Rev. B*, 59:411, 1999.

[76] II Mazin, D. I. Khomskii, R. Lengsdorf, J. A. Alonso, W. G. Marshall, R. A. Ibberson, A. Podlesnyak, M. J. Martinez-Lope, and M. M. Abd-Elmeguid. Charge ordering as alternative to Jahn-Teller distortion. *Phys. Rev. Lett.*, 98:176406, 2007.

[77] D. B. McWhan, T. M. Rice, and J. P. Remeika. Mott Transition in Cr-Doped V_2O_3. *Phys. Rev. Lett.*, 23:1384, 1969.

[78] M. L. Medarde. Structural, magnetic and electronic properties of $RNiO_3$ perovskites (R equals rare earth). *J. Phys.: Condens. Matter*, 9:1679, 1997.

[79] G. Miao, G. Xiao, and A. Gupta. Variations in the magnetic anisotropy properties of epitaxial CrO_2 films as a function of thickness. *Phys. Rev. B*, 71:094418, 2005.

[80] F. Mila, R. Shiina, F.-C. Zhang, A. Joshi, M. Ma, V. Anisimov, and T. M. Rice. Orbitally Degenerate Spin-1 Model for Insulating V_2O_3. *Phys. Rev. Lett.*, 85:1714, 2000.

[81] A. J. Millis. Optical conductivity and correlated electron physics. In D. Baeriswyl and L. Degiorgi, editors, *Strong Interactions in Low Dimensions*. Kluwer Academic, Dordrecht, The Netherlands, 2004.

[82] A. J. Millis and S. N. Coppersmith. Interaction and doping dependence of optical spectral weight of the 2-dimensional Hubbard-model. *Phys. Rev. B*, 42:10807, 1990.

[83] A. J. Millis, A. Zimmers, R. P. S. M. Lobo, N. Bontemps, and C. C. Homes. Mott physics and the optical conductivity of electron-doped cuprates. *Phys. Rev. B*, 72:224517, 2005.

[84] S.-K. Mo, J. D. Denlinger, H.-D. Kim, J.-H. Park, J. W. Allen, A. Sekiyama, A. Yamasaki, K. Kadono, S. Suga, Y. Saitoh, T. Muro, P. Metcalf, G. Keller, K. Held, V. Eyert, V. I. Anisimov, and D. Vollhardt. Prominent Quasiparticle Peak in the Photoemission Spectrum of the Metallic Phase of V_2O_3. *Phys. Rev. Lett.*, 90:186403, 2003.

[85] H. J. A. Molegraaf, C. Presura, D. van der Marel, P. H. Kes, and M. Li. Superconductivity-induced transfer of in-plane spectral weight in $Bi_2Sr_2Ca_2O_{8+\delta}$. *Science*, 295:2239, 2002.

[86] M. A. Mroginski, N. E. Massa, H. Salva, J. A. Alonso, and M. J. Martinez-Lope. Metal-insulator phase transitions of $SmNiO_3$ and $PrNiO_3$: Electrons in a polaronic medium. *Phys. Rev. B*, 60:5304, 1999.

[87] Y. Nohara, S. Yamamoto, and T. Fujiwara. Electronic structure of perovskite-type transition metal oxides $LaMO_3$ ($M=Ti \sim Cu$) by U plus GW approximation. *Phys. Rev. B*, 79:14, 2009.

[88] X. Obradors, L. M. Paulius, M. B. Maple, J. B. Torrance, A. I. Nazzal, J. Fontcuberta, and X. Granados. Pressure-dependence of the metal-insulator-transition in the charge-transfer oxides $RNiO_3$ ($R =$ Pr,Nd,$Nd_{0.7}La_{0.3}$). *Phys. Rev. B*, 47:12353, 1993.

[89] A. Ohtomo and H. Y. Hwang. A high-mobility electron gas at the $LaAlO_3/SrTiO_3$ heterointerface. *Nature*, 427:423, 2004.

[90] Y. Okimoto, T. Katsufuji, T. Ishikawa, A. Urushibara, T. Arima, and Y. Tokura. Anomalous Variation of Optical Spectra with Spin Polarization in Double-Exchange Ferromagnet: $La_{1-x}Sr_xMnO_3$. *Phys. Rev. Lett.*, 75:109, 1995.

[91] M. Ortolani, P. Calvani, and S. Lupi. Frequency-dependent thermal response of the charge system and the restricted sum rules of $La_{2-x}Sr_{x4}$. *Phys. Rev. Lett.*, 94:067002, 2005.

[92] Daniel G. Ouellette, SungBin Lee, Junwoo Son, Susanne Stemmer, Leon Balents, Andrew J. Millis, and S. James Allen. Optical conductivity of $LaNiO_3$: Coherent transport and correlation driven mass enhancement. *Phys. Rev. B*, 82:165112, 2010.

[93] W. J. Padilla, D. Mandrus, and D. N. Basov. Searching for the Slater transition in the pyrochlore $Cd_2Os_2O_7$ with infrared spectroscopy. *Phys. Rev. B*, 66:035120, 2002.

[94] L. Paolasini, C. Vettier, F. de Bergevin, F. Yakhou, D. Mannix, A. Stunault, W. Neubeck, M. Altarelli, M. Fabrizio, P. A. Metcalf, and J. M. Honig. Orbital Occupancy Order in V_2O_3: Resonant X-Ray Scattering Results. *Phys. Rev. Lett.*, 82:4719, 1999.

[95] J. H. Park, L. H. Tjeng, A. Tanaka, J. W. Allen, C. T. Chen, P. Metcalf, J. M. Honig, F. M. F. de Groot, and G. A. Sawatzky. Spin and orbital occupation and phase transitions in V_2O_3. *Phys. Rev. B*, 61:11506, 2000.

[96] S. K. Park, T. Ishikawa, and Y. Tokura. Charge-gap formation upon the Verwey transition in Fe_3O_4. *Phys. Rev. B*, 58:3717, 1998.

[97] A. Perucchi, L. Baldassarre, P. Postorino, and S. Lupi. Optical properties across the insulator to metal transitions in vanadium oxide compounds. *J. Phys.: Condens. Matter*, 21:323202, 2009.

[98] N. Poirot, V. T. Phuoc, G. Gruener, and F. Gervais. Dependence of optical conductivity with δ in $La_2NiO_{4+\delta}$ single crystals. *Solid State Sci.*, 7:1157, 2005.

[99] A. I. Poteryaev, J. M. Tomczak, S. Biermann, A. Georges, A. I. Lichtenstein, A. N. Rubtsov, T. Saha-Dasgupta, and O. K. Andersen. Enhanced crystal-field splitting and orbital-selective coherence induced by strong correlations in V_2O_3. *Phys. Rev. B*, 76:085127, 2007.

[100] A. V. Puchkov, P. Fournier, D. N. Basov, T. Timusk, A. Kapitulnik, and N. N. Kolesnikov. Evolution of the pseudogap state of high-T_c superconductors with doping. *Phys. Rev. Lett.*, 77:3212, 1996.

[101] M. M. Qazilbash, M. Brehm, G. O. Andreev, A. Frenzel, P. C. Ho, Chae Byung-Gyu, Kim Bong-Jun, Yun Sun Jin, Kim Hyun-Tak, A. V. Balatsky, O. G. Shpyrko, M. B. Maple, F. Keilmann, and D. N. Basov. Infrared spectroscopy and nano-imaging of the insulator-to-metal transition in vanadium dioxide. *Phys. Rev. B*, 79:075107, 2009.

[102] M. M. Qazilbash, K. S. Burch, D. Whisler, D. Shrekenhamer, B. G. Chae, H. T. Kim, and D. N. Basov. Correlated metallic state of vanadium dioxide. *Phys. Rev. B*, 74:205118, 2006.

[103] M. M. Qazilbash, J. J. Hamlin, R. E. Baumbach, L. J. Zhang, D. J. Singh, M. B. Maple, and D. N. Basov. Electronic correlations in the iron pnictides. *Nat. Phys.*, 5:647, 2009.

[104] M. M. Qazilbash, A. A. Schafgans, K. S. Burch, S. J. Yun, B. G. Chae, B. J. Kim, H. T. Kim, and D. N. Basov. Electrodynamics of the vanadium oxides VO_2 and V_2O_3. *Phys. Rev. B*, 77:115121, 2008.

[105] K. P. Rajeev, G. V. Shivashankar, and A. K. Raychaudhuri. Low-temperature electronic-properties of a normal conducting perovskite oxide ($LaNiO_3$). *Solid State Commun.*, 79:591, 1991.

[106] H. G. Reik and D. Heese. Frequency dependence of the electrical conductivity of small polarons for high and low temperatures. *J. Phys. Chem. Solids*, 28:581, 1967.

[107] J. W. Reiner, F. J. Walker, and C. H. Ahn. Atomically Engineered Oxide Interfaces. *Science*, 323:1018, 2009.

[108] F. Rodolakis, P. Hansmann, J. P. Rueff, A. Toschi, M. W. Haverkort, G. Sangiovanni, A. Tanaka, T. Saha-Dasgupta, O. K. Andersen, K. Held, M. Sikora, I. Alliot, J. P. Itie, F. Baudelet, P. Wzietek, P. Metcalf, and M. Marsi. Inequivalent Routes across the Mott Transition in V_2O_3 Explored by X-Ray Absorption. *Phys. Rev. Lett.*, 104:047401, 2010.

[109] M. J. Rozenberg, G. Kotliar, and H. Kajueter. Transfer of spectral weight in spectroscopies of correlated electron systems. *Phys. Rev. B*, 54:8452, 1996.

[110] M. J. Rozenberg, G. Kotliar, H. Kajueter, G. A. Thomas, D. H. Rapkine, J. M. Honig, and P. Metcalf. Optical conductivity in mott-hubbard systems. *Phys. Rev. Lett.*, 75:105, 1995.

[111] A. Rusydi, R. Rauer, G. Neuber, M. Bastjan, I. Mahns, S. Muller, P. Saichu, B. Schulz, S. G. Singer, A. I. Lichtenstein, D. Qi, X. Gao, X. Yu, A. T. S. Wee, G. Stryganyuk, K. Dorr, G. A. Sawatzky, S. L. Cooper, and M. Rubhausen. Metal-insulator transition in manganites: Changes in optical conductivity up to 22 eV. *Phys. Rev. B*, 78:5, 2008.

[112] R. D. Sanchez, M. T. Causa, A. Caneiro, A. Butera, M. ValletRegi, M. J. Sayagues, J. GonzalezCalbet, F. GarciaSanz, and J. Rivas. Metal-insulator transition in oxygen-deficient $LaNiO_{3-x}$ perovskites. *Phys. Rev. B*, 54:16574, 1996.

[113] D. D. Sarma, N. Shanthi, and P. Mahadevan. Electronic-structure and the metal-insulator-transition in $LnNiO_3$ (Ln=La, Pr, Nd, Sm and Ho) - band-structure results. *J. Phys.: Condens. Matter*, 6:10467, 1994.

[114] V. Scagnoli, U. Staub, M. Janousch, A. M. Mulders, M. Shi, G. I. Meijer, S. Rosenkranz, S. B. Wilkins, L. Paolasini, J. Karpinski, S. M. Kazakov, and S. W. Lovesey. Charge disproportionation and search for orbital ordering in $NdNiO_3$ by use of resonant x-ray diffraction. *Phys. Rev. B*, 72:155111, 2005.

[115] M. Schubert. Theory and Application of Generalized Ellipsometry. In H. G. Tompkins and E. A. Irene, editors, *Handbook of Ellipsometry*, pages 637–717. William Andrew Publishing/Springer Verlag, 2005.

[116] K. Schwarz. CrO_2 predicted as a half-metallic ferromagnet. *J. Phys. F*, 16:L211, 1986.

[117] E. J. Singley, K. S. Burch, R. Kawakami, J. Stephens, D. D. Awschalom, and D. N. Basov. Electronic structure and carrier dynamics of the ferromagnetic semiconductor $Ga_{1-x}Mn_xAs$. *Phys. Rev. B*, 68:165204, 2003.

[118] E. J. Singley, R. Kawakami, D. D. Awschalom, and D. N. Basov. Infrared Probe of Itinerant Ferromagnetism in $Ga_{1-x}Mn_xAs$. *Phys. Rev. Lett.*, 89:097203, 2002.

[119] E. J. Singley, C. P. Weber, D. N. Basov, A. Barry, and J. M. D. Coey. Charge dynamics in the half-metallic ferromagnet CrO_2. *Phys. Rev. B*, 60:4126, 1999.

[120] I. Solovyev, N. Hamada, and K. Terakura. t(2g) versus all 3d localization in $LaMO_3$ perovskites (M=Ti-Cu): First-principles study. *Phys. Rev.B*, 53:7158, 1996.

[121] J. Son, P. Moetakef, J. M. LeBeau, D. Ouellette, L. Balents, S. J. Allen, and S. Stemmer. Low-dimensional Mott material: Transport in ultrathin epitaxial $LaNiO_3$ films. *Appl. Phys. Lett.*, 96:062114, 2010.

[122] W. G. Spitzer, R. C. Miller, D. A. Kleinman, and L. E. Howarth. Far Infrared Dielectric Dispersion in $BaTiO_3$, $SrTiO_3$, and TiO_2. *Phys. Rev.*, 126:1710, 1962.

[123] K. Sreedhar, J. M. Honig, M. Darwin, M. McElfresh, P. M. Shand, J. Xu, B. C. Crooker, and J. Spalek. Electronic-properties of the metallic perovskite $LaNiO_3$ - correlated behavior of 3d electrons. *Phys. Rev. B*, 46:6382, 1992.

[124] C. B. Stagarescu, X. Su, D. E. Eastman, K. N. Altmann, F. J. Himpsel, and A. Gupta. Orbital character of O-2p unoccupied states near the Fermi level in CrO_2. *Phys. Rev. B*, 61:R9233, 2000.

[125] P. A. Stampe, R. J. Kennedy, S. M. Watt, and S. von Molnar. Strain effects in thin films of CrO_2 on rutile and sapphire substrates. *J. Appl. Phys.*, 89:7696, 2001.

[126] M. K. Stewart, J. Liu, M Kareev, J. Chakhalian, and D. N. Basov. Mott physics near the insulator-to-metal transition in $NdNiO_3$. *Phys. Rev. Lett.*, in press.

[127] M. K. Stewart, J. Liu, R. K. Smith, B. C. Chapler, C. H. Yee, D. Meyers, R. E. Baumbach, M. B. Maple, K. Haule, J. Chakhalian, and D. N. Basov. Optical probe of strong correlations in $LaNiO_3$ thin films. *J. Appl. Phys*, 110:033514, 2011.

[128] M. K. Stewart, C. H. Yee, Jian Liu, M. Kareev, R. K. Smith, B. C. Chapler, M. Varela, P. J. Ryan, K. Haule, J. Chakhalian, and D. N. Basov. Optical study of strained ultrathin films of strongly correlated $LaNiO_3$. *Phys. Rev. B*, 83:075125, 2011.

[129] K. S. Takahashi, M. Gabay, D. Jaccard, K. Shibuya, T. Ohnishi, M. Lippmaa, and J. M. Triscone. Local switching of two-dimensional superconductivity using the ferroelectric field effect. *Nature*, 441:195, 2006.

[130] A. Tanaka. Electronic structure and phase transition in V_2O_3: Importance of 3d spin-orbit interaction and lattice distortion. *J. Phys. Soc. Jap.*, 71:1091, 2002.

[131] P. W. Tasker. The stability of ionic crystal surfaces. *J. Phys. C*, 12:4977, 1979.

[132] B. J. Thamer, R. M. Douglass, and E. Staritzky. The Thermal Decomposition of Aqueous Chromic Acid and Some Properties of the Resulting Solid Phases1. *J. Am. Chem. Soc.*, 79:547, 1957.

[133] T. Tiwald and M. Schubert. Measurement of rutile TiO_2 dielectric tensor from 0.148 to 33 μm using generalized ellipsometry. *Proc. SPIE*, 19:4103, 2000.

[134] A. Tiwari, C. Jin, and J. Narayan. Strain-induced tuning of metal-insulator transition in $NdNiO_3$. *Appl. Phys. Lett.*, 80:4039, 2002.

[135] Y. Tokura. Correlated-electron physics in transition-metal oxides. *Phys. Today*, 56:50, 2003.

[136] A. Toropova, G. Kotliar, S. Y. Savrasov, and V. S. Oudovenko. Electronic structure and magnetic anisotropy of CrO_2. *Phys. Rev. B*, 71:172403, 2005.

[137] J. B. Torrance, P. Lacorre, A. I. Nazzal, E. J. Ansaldo, and C. Niedermayer. Systematic study of insulator-metal transitions in perovskites $RNiO_3$ (R = Pr, Nd, Sm, Eu) due to closing of charge-transfer gap. *Phys. Rev. B*, 45:8209, 1992.

[138] K. Tsubouchi, I. Ohkubo, H. Kumigashira, Y. Matsumoto, T. Ohnishi, M. Lippmaa, H. Koinuma, and M. Oshima. Epitaxial growth and surface metallic nature of $LaNiO_3$ thin films. *Appl. Phys. Lett.*, 92:262109, 2008.

[139] T. Tsujioka, T. Mizokawa, J. Okamoto, A. Fujimori, M. Nohara, H. Takagi, K. Yamaura, and M. Takano. Hubbard splitting and electron correlation in the ferromagnetic metal CrO_2. *Phys. Rev. B*, 56:R15509, 1997.

[140] T. Venkatesan, X. D. Wu, A. Inam, and J. B. Wachtman. Observation of two distinct components during pulsed laser deposition of high T_c superconducting films. *Appl. Phys. Lett.*, 52:1193, 1988.

[141] X. Q. Xu, J. L. Peng, Z. Y. Li, H. L. Ju, and R. L. Greene. Resistivity, thermopower, and susceptibility of $RNiO_3$ (R = La,Pr). *Phys. Rev. B*, 48:1112, 1993.

[142] R. Yamamoto, Y. Moritomo, and A. Nakamura. Electronic structure of half-metallic CrO_2 as investigated by optical spectroscopy. *Phys. Rev. B*, 61:R5062, 2000.

[143] S. Yamamoto and T. Fujiwara. Charge and spin order in $RNiO_3$ (R=Nd, Y) by LSDA+U method. *J. Phys. Soc. Jpn.*, 71:1226, 2002.

[144] T. Yoshii, Y. Hamanaka, Y. Moritomo, and A. Nakamura. Critical behavior of a photo-disordered spin system in epitaxial CrO_2 films. *J. Lumin.*, 108:225, 2004.

[145] M. Zaghrioui, A. Bulou, P. Lacorre, and P. Laffez. Electron diffraction and Raman scattering evidence of a symmetry breaking at the metal-insulator transition of $NdNiO_3$. *Phys. Rev. B*, 64:081102, 2001.

[146] Z. M. Zhang, B. I. Choi, M. I. Flik, and A. C. Anderson. Infrared refractive indices of $LaAlO_3$, $LaGaO_3$, and $NdGaO_3$. *J. Opt. Soc. Am. B*, 11:2252, 1994.

[147] J. S. Zhou, J. B. Goodenough, and B. Dabrowski. Exchange interaction in the insulating phase of $RNiO_3$. *Phys. Rev. Lett.*, 95:127204, 2005.

[148] J. S. Zhou, J. B. Goodenough, B. Dabrowski, P. W. Klamut, and Z. Bukowski. Probing the metal-insulator transition in Ni(III)-oxide perovskites. *Phys. Rev. B*, 61:4401, 2000.